

Design and Analysis of the Onsala 4 mm Receiver and other Antenna Configurations for Millimetre Wave Astronomy

Presented by

George William Walker, B.A. (Mod.)

A thesis submitted for the degree of

Master of Science

at the

National University of Ireland, Maynooth

Terahertz Optics and Technology Group

Department of Experimental Physics

Faculty of Science and Engineering

August 2016

Head of Department

Professor J. Anthony Murphy

Research Supervisor

Dr Neil A. Trappe

Table of Contents

Abstract	vi
Acknowledgements	viii
1 Introduction	1
1.1 Historical Background of Astronomy	1
1.2 Millimetre and Submillimetre Astronomy	4
1.3 Astronomical Applications	5
1.4 Commercial Applications	7
1.5 Thesis Overview and Author's Contribution	7
2 Background Theory	11
2.1 Gaussian Beam Mode Analysis	12
2.1.1 Paraxial Wave Equation	12
2.1.2 Fundamental Gaussian Beam Mode in Cylindrical Coordinates .	13
2.1.3 Normalization	18
2.1.4 Fundamental Gaussian Beam Mode in Rectangular Coordinates	18
2.1.5 Confocal Distance	20
2.1.6 Edge Taper	20
2.2 Higher Order Gaussian Beam Modes	21
2.2.1 Higher Order Modes in Cylindrical Coordinates	22
2.2.2 Higher Order Modes in Rectangular Coordinates	23
2.3 Ray Transfer Matrix Analysis	25
2.4 Analysis of Antenna Systems	29

2.4.1	Telescope	29
2.4.2	Conical Corrugated Horn	29
2.4.3	Horn transition	31
2.4.4	Beam coupling	32
2.5	Introduction to GRASP	33
2.5.1	Physical Optics Analysis	33
2.5.2	System Generation in GRASP	37
2.5.3	GRASP Input Sources	38
2.5.4	Reflectors	40
2.5.5	Verification of GRASP using the VNA	42
2.6	Conclusion	43
3	Onsala 4 mm Receiver	44
3.1	Onsala Space Observatory	45
3.1.1	25 m and 20 m Telescopes	45
3.1.2	20 m Telescope Optics	48
3.2	4 mm Receiver	49
3.2.1	Design Requirements	50
3.2.2	Horn Design	54
3.2.3	Further Design Considerations	56
3.3	Initial Optical Analysis	58
3.4	Truncation Analysis	61
3.5	Optical Efficiency	68
3.6	Conclusion	70
4	PO Analysis of the 4 mm Receiver	71
4.1	GRASP Analysis	71
4.1.1	Gaussian beam	72
4.1.2	GRASP Hybrid Horn	74
4.1.3	Horn Aperture Grid Files	77
4.2	Propagation of the beam to the Sky	79

4.3	Cross polar levels	81
4.4	Comparison with the 3mm system	82
4.5	Experimental Measurements	83
4.6	Conclusion	89
5	W Band Lens Antenna Design and Analysis	90
5.1	Introduction	91
5.2	Planar Antenna theory	91
5.2.1	Analysis of Patch Antennae	92
5.2.2	S-Parameter	95
5.2.3	Directivity	96
5.2.4	CST Microwave Studio	96
5.3	Circular Patch	98
5.3.1	Addition of HDPE lenses	100
5.3.2	Wrap around lens	103
5.4	Alternative patch designs	106
5.4.1	Square patch	106
5.4.2	H-antenna dipole	107
5.4.3	Ellipsoidal lens	108
5.4.4	Rectangular patch antenna	109
5.5	Further Design Considerations	112
5.6	Conclusion	116
6	Detector Cavities	117
6.1	Background	117
6.2	Modelling of Detector Cavities within CST	118
6.3	Cavity 1	119
6.3.1	Optimization of Simulation Efficiency	120
6.3.2	Using Two Ohmic Sheets	122
6.3.3	Modelling the Ohmic sheet on a Dielectric	123
6.3.4	Offset Position of Waveguide	125

Table of Contents

6.3.5	Absorber position	127
6.4	Cavity 2	128
6.4.1	Two Ohmic Sheets	128
6.4.2	Effect of Dielectric Thickness	129
6.4.3	Offset Position of Waveguide	131
6.5	Cavity 3	133
6.5.1	Two Ohmic Sheets	133
6.5.2	Effect of Dielectric Thickness	134
6.5.3	Offset Position of Waveguide	135
6.6	Conclusion	137
7	Conclusions	138
	Bibliography	146

Abstract

This thesis outlines several different topics associated with the design and analysis of millimetre and submillimetre systems. A major topic is the design, analysis and verification of a 4 mm receiver for the 20 m telescope at Onsala Space Observatory, Onsala, Sweden. The 4 mm receiver was designed to be installed parallel to the existing 3 mm channel to target new science at that longer wavelength. Gaussian beam mode analysis was used to produce the fundamental optical design. This is computationally efficient, and provides all critical beam characterization through the optical train within the paraxial limit. The design was analysed more accurately with physical optics, using GRASP, a commercial software package developed by TICRA. Following the manufacture of the system, experimental verification was performed at Onsala Space Observatory. Measurements of the beam were compared with simulations to verify the operation at 69 GHz.

In addition to this, an investigation was carried out into the development of lens antennae fed by planar antennae with good beam characteristics, as an alternative to horn antennae in the W band. A variety of patch designs were considered, with the effect of a lens placed in front of them. This adds the required directionality to the beam to launch or receive signals efficiently. CST Microwave studio was used for this investigation.

Finally, the behaviour of absorbing bolometer detectors housed in waveguide cavities was examined, in particular the effects of varying the absorber and input waveguide position for a number of different cavity geometries. The goal was to analyse

Abstract

the effect of these parameters on the optical coupling: how much incident radiation was absorbed in a thin absorbing layer of tantulum associated with a TES detector. This work was directed towards the SAFARI instrument for proposed SPICA missions. The analysis tool was CST Microwave Studio.

Acknowledgements

First of all, I wish to thank my supervisor, Dr Neil Trappe, for all his valuable help, support, and guidance on the work presented in this thesis. I appreciate his dedication and patience during my time as a postgraduate and thank him for the time he has spent sharing his extensive knowledge of the area, and for always offering helpful comments on my work. His door was always open whenever I ran into trouble or had a question. I am grateful for having been given the opportunity to join the Terahertz Space Optics Group, and to Professor Anthony Murphy for the use of department facilities. Thanks to Eimante Kalinauskaite for her work on the horn antenna used in the Onsala 4 mm system, and for providing me with the details of it for use in my thesis. Thanks to Dr Darragh McCarthy for always being enthusiastically willing to discuss any issues, especially in relation to the Onsala system and GRASP. Thanks to all the other members of the department, especially Gráinne Roche for her secretarial work. Thanks also to Dr Frank Mulligan for his helpful comments and advice about teaching. Thanks to those with whom I have shared an office: Dr Patrick Connell during my first year, Rory Sheridan for a while, and to Adam Byrne during the last year. Thanks to Benraad for keeping the office warm. To the other postgraduates in the department, thank you for making my time in Maynooth enjoyable.

Many thanks to those I worked with at Onsala Space Observatory: Dr Miroslav Pantaleev, Leif Helldner, and especially to Jonas Flygare for his correspondence in relation to the experimental measurements of the 4 mm receiver. I am grateful for twice having had the opportunity to visit Onsala Space Observatory.

Acknowledgements

I am very grateful for the financial support I received through the European Space Agency contract RFQ 3-6418/11/NL/CBI (New Technology high efficiency horn antennas for cosmic microwave background experiments and FarIR astronomy).

Finally, a special thanks to my family — Mum, Dad, Wendy, Valerie, Jason, and Granny — for always being there for me and offering support and encouragement during my time in college and university.

Chapter 1

Introduction

Contents

1.1 Historical Background of Astronomy	1
1.2 Millimetre and Submillimetre Astronomy	4
1.3 Astronomical Applications	5
1.4 Commercial Applications	7
1.5 Thesis Overview and Author's Contribution	7

1.1 Historical Background of Astronomy

Astronomy is one of the oldest of the natural sciences, and since ancient times, humanity has been performing methodical observations of the night sky. The earliest civilizations engaged in astronomical research, devising calendars based on the movements of celestial objects, and using this knowledge for such diverse activities as the timing of crop plantations or the dating of Easter. In more recent times, astronomical research has resulted in a significant increase in human understanding of the physics of the universe [1].

Historically, most astronomical research took place using optical wavelengths (400–700 nm), as these are the wavelengths visible to the human eye. However, these wavelengths only form a tiny portion of the electromagnetic spectrum, as shown in figure 1.1. Many of the great astronomers of history, including Copernicus, Brahe, Galileo, and Newton all relied on these wavelengths to perform their astronomical

observations. This reliance was due to the use of the the naked eye, and what could be magnified by simple optical telescopes at visible wavelengths.

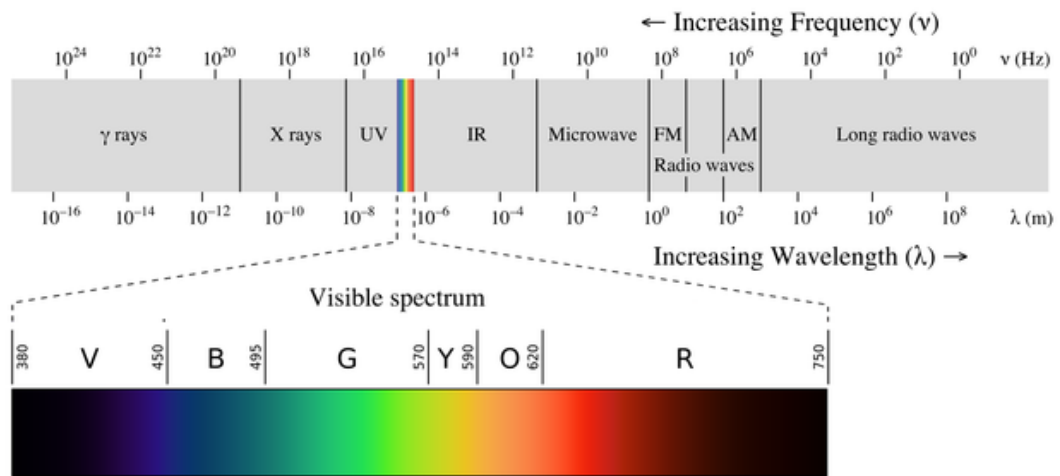


Figure 1.1: Electromagnetic spectrum, highlighting visible light [2].

In the nineteenth century, James Clerk Maxwell showed that visible light was an electromagnetic wave [3]. Maxwell's Equations describe electromagnetic waves as oscillating electric and magnetic fields, which can be produced by an accelerating charged particle. In 1887, Heinrich Hertz produced electromagnetic waves at longer wavelengths, and demonstrated that they had the same properties as light such as standing waves, diffraction, refraction, and polarization. These waves became known as radio waves, and were to revolutionize communication in the early twentieth century.

The first application of radio waves to astronomy was in 1932, when Karl Jansky discovered radio emissions coming from the Milky Way [4]. Subsequent observation has revealed a number of different sources of radiation of these frequencies, not only including stars and galaxies, but also a host of previously unknown objects, such as radio galaxies, quasars, and pulsars. Perhaps one of the most significant discoveries at radio frequencies has been the Cosmic Microwave Background (CMB), which is evidence for a finite age of the universe. This led to the replacement of the steady state theory of the universe with the cosmological model known as the Big

Bang .

Detection of electromagnetic waves requires vastly different methods of observation depending on which frequency band is being observed. As a result of this, telescopes specialize in certain parts of the electromagnetic spectrum. For example, the Very Large Array (VLA) operates at radio frequencies [5], the Atacama Large Millimetre Array (ALMA) and the Herschel Space Telescope for millimetre and sub-millimetre wavelengths [6] [7], the Hubble Space Telescope at optical and infrared [8], and the XMM Newton Space Observatory is designed for the detection of x-rays [9].

It is useful to study the universe using a variety of different wavelengths, as different information may be revealed depending on the wavelength used. Certain features that are visible in one region of the spectrum may become transparent in others, hence that which previously obscured may be visible when viewed using different frequencies. An example of this is shown below in figure 1.2. This shows images of the Horsehead Nebula taken using different wavelengths. The Horsehead Nebula is a region of star formation located in the Orion constellation.

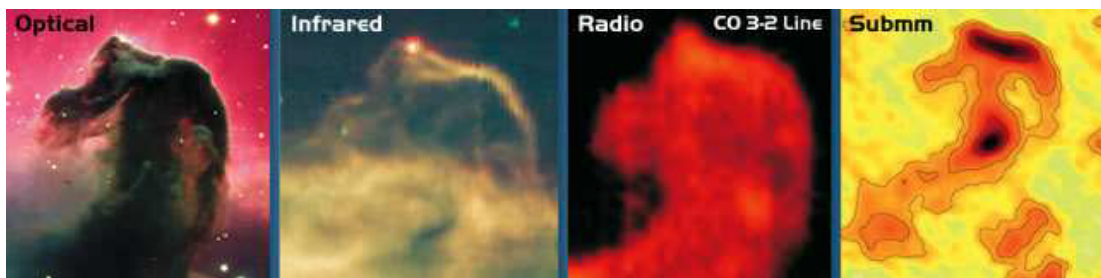


Figure 1.2: The Horsehead Nebula, viewed at different wavelengths [6].

The image taken at optical wavelengths shows the dark dust, which obscures the visible radiation from within the nebula. The layer of hot gas around the nebula then becomes visible at infrared and radio wavelengths. In the submillimetre band, the dust is transparent, and the inner structure of the nebula is revealed. The darker regions are those with the peak emission, and indicate the presence of star-forming clouds.

1.2 Millimetre and Submillimetre Astronomy

The far-infrared region of the electromagnetic spectrum is rather loosely defined, and is interchangeably also referred to as the Terahertz region or the submillimetre region. In terms of frequency, this region is loosely in the range 0.1 THz – 10 THz [10]. The term "submillimetre" refers to wavelengths in the region 100 μm – 1 mm. The millimetre waveband ranges from 1 mm – 10 mm. The far-infrared region in the electromagnetic spectrum has commonly been referred to as the Terahertz gap, as it was the last unexplored region of the electromagnetic spectrum due to a difficulty in the development of detectors and readily available sources. However, the gap is now being filled due to new technology being developed and made available. The position of the Terahertz gap relative to the rest of the electromagnetic spectrum is illustrated in figure 1.3.

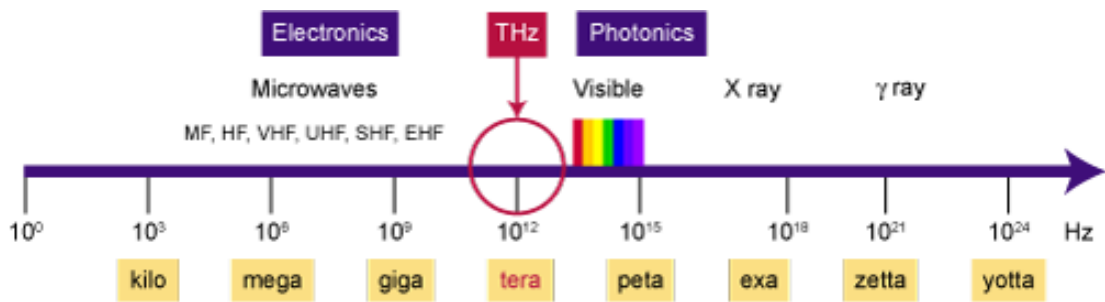


Figure 1.3: The Terahertz gap in the electromagnetic spectrum [11].

The Terahertz gap exists in the region between optical wavelengths and radio wavelengths. At shorter wavelengths, in the optical region, the method of analysis is primarily ray tracing and geometrical optics, as traditional mirrors and lenses are used. At higher wavelengths, where diffraction effects dominate, full electromagnetic analysis requiring solutions to Maxwell's equations are required to model the radio waves and microwaves. A combination of optical and microwave techniques is necessary for analysis in the Terahertz region.

Gaussian beam mode analysis, which was initially developed for lasers at near-infrared wavelengths, is commonly used for the analysis of optical systems which operate in

the millimetre and submillimetre regions. This method of analysis is based primarily on the propagation of Gaussian beam modes that are solutions to the paraxial wave equation [12]. Gaussian beam mode analysis is useful for the initial design and analysis of a system. However, there are some drawbacks to this method when good accuracy is required. The Physical Optics technique provides greater accuracy, especially when off-axis reflecting systems are being studied. The drawback with Physical Optics is that it is less computationally efficient, which results in longer simulation times.

1.3 Astronomical Applications

An important application of radiation at Terahertz frequencies is in the observation of cool objects in the universe such as interstellar gas and dust. Many important astronomical sources radiate at these frequencies. From $hf \approx kT$, the equivalent blackbody temperature for objects radiating at Terahertz frequencies ranges from 40 K to 480 K. For example, dense interstellar gas typically has a temperature ranging from approximately 10 K in cooler regions up to 100 K or 200 K in the denser and hotter parts. Due to the CMB, there is significant radiation at the lower frequencies of the millimetre waveband. Some highly redshifted galaxies may also be observed at these wavelengths. In addition, there are many important spectral lines resulting from certain molecular rotations and atomic transitions. These are of interest as they reveal significant information concerning the chemical make up of various objects in the universe such as gas and dust clouds.

Electromagnetic radiation is emitted or absorbed by different chemical compounds at different frequencies, which are well-defined. In order to detect radiation from extra-terrestrial sources, the radiation has to pass through the earth's atmosphere. Certain vibrational or rotational transitions can be excited in molecules by photons at certain energies. This phenomenon results in transition and absorption lines, which means photons at certain frequencies are absorbed by the atmosphere. For

millimetre wavelengths (up to 300 GHz in terms of frequency), only certain O₂ and H₂O lines are present, so the atmosphere is largely transparent. However, in the sub-millimetre range, a large number of absorption lines (mainly due to water vapour) are present, which results in the atmosphere being very opaque. The opacity of the earth's atmosphere, across the electromagnetic spectrum, is shown in figure 1.4, demonstrating the lack of transparency in the millimetre and submillimetre wavebands.

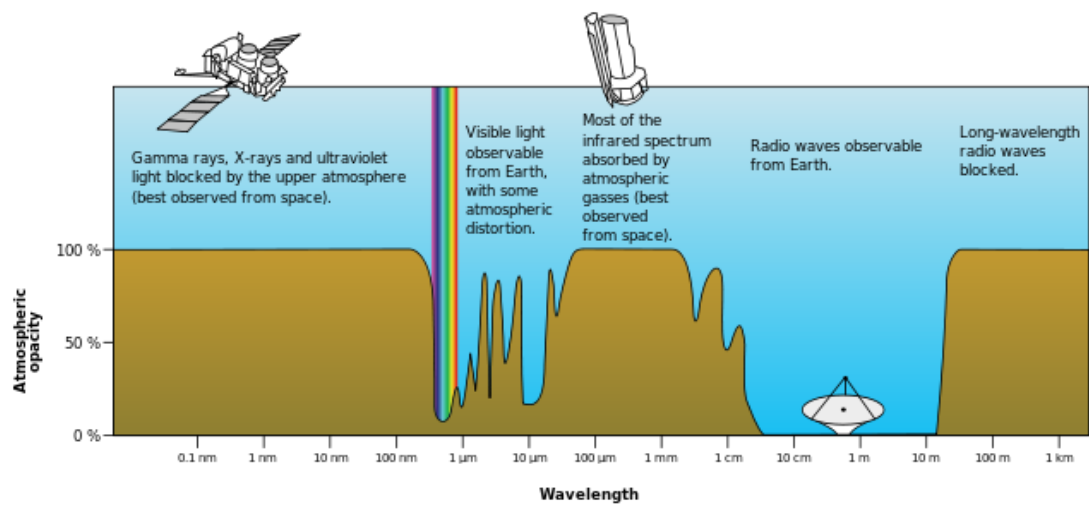


Figure 1.4: Atmospheric opacity, shown for wavelengths across the electromagnetic spectrum [13].

This is why telescopes designed to operate in the submillimetre range are often placed at very high altitudes in dry environments, so that the amount of water above the telescope will be reduced as much as possible. For example, ALMA is located in the Chajnantor plateau in the Atacama desert in Chile, which is at an altitude of 5100 m above sea level. An alternative solution is to use a satellite outside the earth's atmosphere as a platform for a telescope. For example, the Herschel Space Telescope was a space based telescope, which was designed to observe in the sub-millimetre band $55 \mu\text{m} - 672 \mu\text{m}$. It was in operation between 2009 and 2013, when it completed its mission. The disadvantage of using a space telescope is that the components must be smaller than those typically used on the ground, due to the restrictive costs of sending objects into space.

In this thesis, the Onsala 4 mm receiver design is analysed. This receiver can be classified as a millimetre wave band receiver, and can operate relatively well between 67 and 86 GHz, observing interstellar medium spectral lines, unlike higher frequency Terahertz receivers.

1.4 Commercial Applications

In addition to a wide range of applications of Terahertz radiation to scientific research, there are also some commercial applications [14]. For example, it can be used in security systems at airports and other places where screening for sharp objects or illegal substances is necessary. Terahertz radiation is absorbed by human skin, but not by clothing or metallic and ceramic objects. Because of this, it is suitable for non-invasive scanning for concealed objects. In addition, radiation at Terahertz frequencies is non-ionizing, so it is much safer to use for a scan than high frequency x-rays. Terahertz radiation will reveal sharp objects of a non-metallic nature, such as ceramic knives. It also may be used to target compounds such as explosives and illicit drugs, which have characteristic Terahertz spectra. This provides an additional layer of security, as such objects would be overlooked by conventional metal detectors [15].

Other applications include using a Terahertz scan to safely examine a wound under a bandage, without having to remove it [16], and the measurement of the quality of pharmaceutical tablet coatings [17].

1.5 Thesis Overview and Author's Contribution

This thesis is primarily concerned with the design, analysis, and verification of a new receiver channel for the 20 m telescope at Onsala Space Observatory, Onsala, Sweden. The receiver channel is referred to as the *4 mm receiver*, as it is designed to

operate in the frequency range 67–86 GHz, the centre of which corresponds approximately to this wavelength. In addition to this, the design and analysis of a W band (75–110 GHz) planar antenna with spherical lenslet is outlined, and some analysis on the effect the design of a detector cavity has on its resonant frequency is presented. The following is a summary of the thesis content, by chapter, and details the specific contributions of the author.

Chapter 2

Chapter 2 gives an overview of optical analysis techniques and background theory. A derivation of Gaussian Beam Mode Analysis is presented as this forms the basis of quasioptical analysis for millimetre and submillimetre optical systems, and is used extensively throughout this thesis. The derivation of ray transfer matrix analysis is presented, as this was the method used in the design of the Onsala 4 mm receiver. The theory behind antenna systems and horn antennae is also outlined. GRASP, an optical software package, is also introduced, along with the mathematical methods which form the basis of its operation. The author performed a brief experimental verification of GRASP, using the vector network analyser at Maynooth.

Chapter 3

In chapter 3, the 4 mm receiver system for the 20 m telescope at Onsala Space Observatory is introduced, and the preliminary design and analysis, making use of ray transfer matrix analysis, is reported.

The author was responsible for the optical design of the 4 mm receiver, and for the simulations reported to colleagues at Onsala Space Observatory. Using Mathematica [18], the author analysed the beam parameters of the 4 mm receiver, and analysed the truncation levels and coupling estimations across the frequency band of operation.

Chapter 4

Chapter 4 reports further analysis of the 4 mm receiver system, using physical optics in GRASP; including a three-dimensional model, and a variety of feed models. A model beam is propagated to the sky in GRASP, verifying the design, and cross-polar levels are reported. Additionally, the design of the 4 mm receiver is compared with that of the 3 mm receiver, and experimental results from Onsala Space Observatory are compared with the equivalent simulations. Conclusions on the realized design are also reported.

The author produced the GRASP files used for the analysis, and analysed the performance of the system as presented in this chapter.

Chapter 5

In chapter 5, the design and analysis of a W band lens antenna are reported. The motivation for this work is introduced, and an overview of patch antenna theory is presented. CST Microwave Studio, a software package for high frequency electromagnetic design and analysis, is introduced, as this software package was used for the simulations in chapters 5 and 6.

The performance of a variety of patch antenna designs is presented, and how the addition of a lens in front of the antenna affects this performance is discussed. The author performed all the analysis presented in this chapter using CST.

Chapter 6

In Chapter 6 the behaviour of rectangular detector cavities is investigated, and it is shown that the geometry of the cavity, and the position of an input waveguide has a large effect on its optical performance. The author performed the simulations used in the analysis presented in this chapter using CST.

Chapter 7

Chapter 7 presents a summary of the work carried out for the thesis, and final conclusions.

Chapter 2

Background Theory

Contents

2.1 Gaussian Beam Mode Analysis	12
2.1.1 Paraxial Wave Equation	12
2.1.2 Fundamental Gaussian Beam Mode in Cylindrical Coordinates	13
2.1.3 Normalization	18
2.1.4 Fundamental Gaussian Beam Mode in Rectangular Coordinates	18
One Dimension	18
Two dimensions	19
2.1.5 Confocal Distance	20
2.1.6 Edge Taper	20
2.2 Higher Order Gaussian Beam Modes	21
2.2.1 Higher Order Modes in Cylindrical Coordinates	22
2.2.2 Higher Order Modes in Rectangular Coordinates	23
2.3 Ray Transfer Matrix Analysis	25
2.4 Analysis of Antenna Systems	29
2.4.1 Telescope	29
2.4.2 Conical Corrugated Horn	29
2.4.3 Horn transition	31
2.4.4 Beam coupling	32
2.5 Introduction to GRASP	33
2.5.1 Physical Optics Analysis	33
Cross-polarization	36
Physical Theory of Diffraction	36
2.5.2 System Generation in GRASP	37
2.5.3 GRASP Input Sources	38
Gaussian Beam	38
Hybrid Mode Conical Horn	39

Tabulated Planar Source	39
2.5.4 Reflectors	40
2.5.5 Verification of GRASP using the VNA	42
2.6 Conclusion	43

2.1 Gaussian Beam Mode Analysis

Gaussian beam mode analysis (GBMA) plays an important role in the design and verification of quasioptical systems. In this thesis, it is used for the initial optical design of the Onsala 4 mm receiver system (chapter 3), as it is a computationally efficient method which provides all critical beam characterization through the optical train, within the paraxial limit. Gaussian beams represent electromagnetic radiation in which the transverse electric field and intensity are defined as on-axis power with relatively low levels of truncation or beam clipping.

2.1.1 Paraxial Wave Equation

The formal mathematical treatment for Gaussian beam mode theory is found in [12] and [19]. The paraxial wave equation is the basis for Gaussian beam mode propagation. This makes the assumption that the variation of the amplitude along the direction of propagation will be small over distances comparable with the wavelength, and that the axial variation will be small compared with the perpendicular variation.

The Helmholtz wave equation is satisfied for components of the electromagnetic field [20]:

$$(\nabla^2 + k^2)\psi = 0, \quad (2.1)$$

where ψ is any component of \mathbf{E} or \mathbf{H} . k is the wavenumber, which is equal to $2\pi/\lambda$, where λ is the wavelength. By allowing the direction of propagation to be in the

positive z direction, the expression for the electric field can be given by

$$E(x, y, z) = u(x, y, z)e^{-ikz}, \quad (2.2)$$

where u is a complex scalar function that defines the non-plane part of the beam. k is the wavenumber, and i is the complex identity. The Helmholtz equation becomes (in rectangular coordinates):

$$\frac{\partial^2 E}{\partial x^2} + \frac{\partial^2 E}{\partial y^2} + \frac{\partial^2 E}{\partial z^2} + k^2 E = 0. \quad (2.3)$$

By substituting the expression for the electric field, the reduced wave equation is obtained:

$$\frac{\partial^2 u}{\partial x^2} + \frac{\partial^2 u}{\partial y^2} + \frac{\partial^2 u}{\partial z^2} - 2ik \frac{\partial u}{\partial z} = 0. \quad (2.4)$$

The next step is to apply the paraxial approximation. The third term is small compared to the fourth term because of the small variation of the amplitude along the direction of propagation. It is also small compared to the first two terms because of the assumption that the axial variation is small compared to the perpendicular variation. Consequently, this term is dropped to obtain the reduced paraxial wave equation in rectangular coordinates [12].

$$\frac{\partial^2 u}{\partial x^2} + \frac{\partial^2 u}{\partial y^2} - 2ik \frac{\partial u}{\partial z} = 0. \quad (2.5)$$

2.1.2 Fundamental Gaussian Beam Mode in Cylindrical Coordinates

Cylindrical coordinates are more convenient for circularly symmetric optical systems. In cylindrical coordinates, the axially symmetric paraxial equation is given by

$$\frac{\partial^2 u}{\partial r^2} + \frac{1}{r} \frac{\partial u}{\partial r} - 2ik \frac{\partial u}{\partial z} = 0. \quad (2.6)$$

The simplest solution of the axially symmetric paraxial wave equation can be written as

$$u(r, z) = A(z) \exp \left[\frac{-ikr^2}{2q(z)} \right], \quad (2.7)$$

where A and q are two complex functions of z . These functions, defined below, are found by substituting equation 2.7 for u into the axially symmetric paraxial wave equation 2.6:

$$-2ik \left(\frac{A}{q} + \frac{\partial A}{\partial z} \right) + \frac{k^2 r^2 A}{q^2} \left(\frac{\partial q}{\partial z} - 1 \right) = 0. \quad (2.8)$$

The two parts of this equation must equal zero since while the first part only depends on z , the second part depends on both r and z , and the equation must be satisfied for all values of r and z . This gives the following two simultaneous equations:

$$\frac{\partial q}{\partial z} = 1, \quad (2.9)$$

$$\frac{\partial A}{\partial z} = -\frac{A}{q}. \quad (2.10)$$

The solution for equation 2.9 is given by

$$q(z) = q(z_0) + (z - z_0). \quad (2.11)$$

This function q is called the complex beam parameter or Gaussian beam parameter. q is a function of z , unless otherwise indicated. As it appears as $1/q$ in equation 2.7, it is convenient to write

$$\frac{1}{q} = \left(\frac{1}{q} \right)_r - i \left(\frac{1}{q} \right)_i. \quad (2.12)$$

By substituting this into equation 2.7, the exponential term becomes

$$\exp \left(\frac{-ikr^2}{2q} \right) = \exp \left[\left(\frac{-ikr^2}{2} \right) \left(\frac{1}{q} \right)_r - \left(\frac{kr^2}{2} \right) \left(\frac{1}{q} \right)_i \right]. \quad (2.13)$$

The imaginary term here has the form of a phase variation produced by a spherical wave in the paraxial limit. This can be compared with an equiphase surface having a radius of curvature R . $\phi(r)$ is defined to be the phase variation as a function of r relative to a plane at a fixed value of z . When $r \ll R$, the phase delay is approximately equal to

$$\phi(r) \approx \frac{\pi r^2}{\lambda R} = \frac{kr^2}{2R}. \quad (2.14)$$

The real part of $1/q$ is then identified with the radius of curvature of the beam:

$$\left(\frac{1}{q}\right)_r = \frac{1}{R}. \quad (2.15)$$

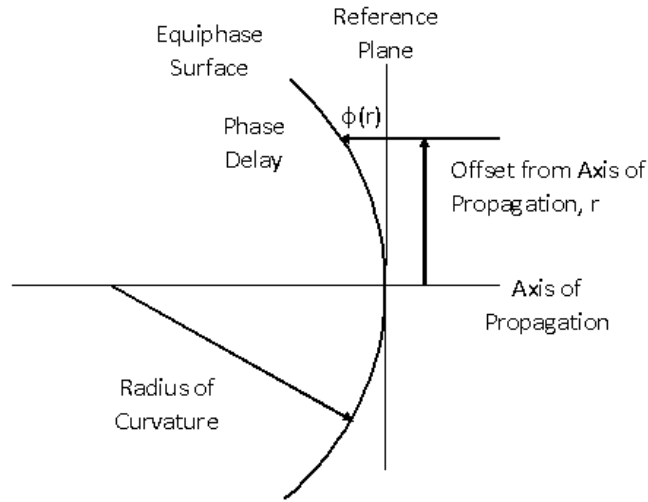


Figure 2.1: Phase shift of spherical wave relative to plane wave. $\phi(r)$ is the phase delay of the spherical wave at a distance r from the axis of propagation.

The second part of equation 2.13 is real and has a Gaussian variation as a function of the distance from the axis of propagation. This can be equated with the exponential part of a standard Gaussian distribution:

$$-\left(\frac{r}{r_0}\right)^2 = -\left(\frac{kr^2}{2}\right)\left(\frac{1}{q}\right)_i. \quad (2.16)$$

The imaginary part of $1/q$ is then found to be

$$\left(\frac{1}{q}\right)_i = \frac{2}{kw^2(z)} = \frac{\lambda}{\pi w^2}, \quad (2.17)$$

where w is called the beam radius and is the radius of the beam at which the field falls to $1/e$ relative to its value on the axis of propagation.

By substituting equations 2.15 and 2.17 into equation 2.12, the function q is given by

$$\frac{1}{q} = \frac{1}{R} - \frac{i\lambda}{\pi w^2}, \quad (2.18)$$

where R and w are both functions of z .

At $z = 0$, from equation 2.7, $u(r, 0) = A(0) \exp[-ikr^2/2q(0)]$. If w_0 is chosen such that $w_0 = [\lambda q(0)/i\pi]^{0.5}$, the relative field distribution at $z = 0$ is found to be

$$u(r, 0) = u(0, 0) \exp\left(\frac{-r^2}{w_0^2}\right). \quad (2.19)$$

w_0 is the source plane beam radius, at $z = 0$. It is called the beam waist radius. From this and equation 2.11, taking $z_0 = 0$, the following important expression for q is obtained [12]:

$$q = \frac{i\pi w_0^2}{\lambda} + z. \quad (2.20)$$

Expressions for the radius of curvature and the beam radius as a function of position along the axis of propagation can be derived from equations 2.18 and 2.20:

$$R = z + \frac{1}{z} \left(\frac{\pi w_0^2}{\lambda}\right)^2, \quad (2.21)$$

$$w = w_0 \left[1 + \left(\frac{\lambda z}{\pi w_0^2}\right)^2\right]^{0.5}. \quad (2.22)$$

These relations for radius of curvature and beam radius are fundamental to Gaussian beam mode propagation. Equation 2.22 shows that the beam waist radius is the

minimum value of the beam radius, and it occurs at the beam waist, where $z = 0$. At this point, equation 2.21 shows that the radius of curvature becomes infinite. Both of these values depend on λ , so in the geometrical limit ($\lambda \rightarrow 0$), the beam radius becomes constant, and the radius of curvature diverges to infinity.

From equations 2.9 and 2.10,

$$\frac{dA}{A} = -\frac{dq}{q}. \quad (2.23)$$

Integration, with limits of z and 0 yields

$$\frac{A(z)}{A(0)} = \frac{q(0)}{q(z)}, \quad (2.24)$$

and by substituting q from equation 2.20,

$$\frac{A(z)}{A(0)} = \frac{1 + i\lambda z/\pi w_0^2}{1 + (\lambda z/\pi w_0^2)^2}. \quad (2.25)$$

Expressing this in terms of a phasor is convenient, giving

$$\frac{A(z)}{A(0)} = \frac{w_0}{w} \exp(i\phi_0), \quad (2.26)$$

where

$$\tan \phi_0 = \frac{\lambda z}{\pi w_0^2}. \quad (2.27)$$

ϕ_0 is referred to as the Gaussian beam phase shift.

By taking the on-axis amplitude at the beam waist to be one, the complete expression for the fundamental Gaussian beam mode is given by

$$u(r, z) = \frac{w_0}{w} \exp\left(\frac{-r^2}{w^2} - \frac{i\pi r^2}{\lambda R} + i\phi_0\right). \quad (2.28)$$

Hence, the expression for the electric field can be found using equation 2.2, which

differs only by inclusion of the plane wave phase factor:

$$E(r, z) = \frac{w_0}{w} \exp\left(\frac{-r^2}{w^2} - ikz - \frac{i\pi r^2}{\lambda R} + i\phi_0\right). \quad (2.29)$$

2.1.3 Normalization

In order to relate equation 2.29 for the electric field to the total power in a Gaussian beam, using the paraxial limit it is assumed that the electric and magnetic fields are related to each other, as in a plane wave. In this case, the total power is proportional to the square of the electric field integrated over the beam area. A convenient normalization is to set this integral to one, with the radius extending from 0 to ∞ :

$$\int |E|^2 \cdot 2\pi r \, dr. \quad (2.30)$$

When this integral of equation 2.2 is evaluated at $z = 0$, it is found to be $\pi w_0^2/2$. As a result, the normalized electric field distribution at a distance z along the axis of propagation is given by

$$E(r, z) = \left(\frac{2}{\pi w^2}\right)^{0.5} \exp\left(-\frac{r^2}{w^2} - \frac{i\pi r^2}{\lambda R} + i\phi_0 - ikz\right). \quad (2.31)$$

2.1.4 Fundamental Gaussian Beam Mode in Rectangular Coordinates

One Dimension

As a simple example, here a 2-dimensional beam that has variation in the x direction is considered. In this case, the paraxial wave equation is reduced to

$$\frac{\partial^2 u}{\partial x^2} - 2ik \frac{\partial u}{\partial z} = 0. \quad (2.32)$$

Using the trial solution,

$$u(x, z) = A_x(z) \exp\left(-\frac{ikx^2}{2q_x(z)}\right), \quad (2.33)$$

which is similar to equation 2.7, it can be shown that the solution for q_x as a function of z is similar to that found for q in equation 2.20 [12]:

$$q_x = \frac{i\pi w_{0x}^2}{\lambda} + z. \quad (2.34)$$

The normalized electric field distribution is given by

$$E(x, z) = \left(\frac{2}{\pi w_x^2}\right)^{0.25} \exp\left(-\frac{x^2}{w_x^2} - \frac{i\pi x^2}{\lambda R_x} + \frac{i\phi_{0x}}{2} - ikz\right), \quad (2.35)$$

where w_x , R_x , and ϕ_{0x} are defined analogously to w , R , and ϕ_0 previously. The additional square root in the normalizing factor is a result of the variation being in one direction. The phase shift is half as large as in the preceding case.

Two dimensions

In two dimensions, a similar approach is used. The trial solution is

$$u(x, y, z) = A_x(z)A_y(z) \exp\left(-\frac{ikx^2}{2q_x}\right) \exp\left(-\frac{iky^2}{2q_y}\right). \quad (2.36)$$

This form is used in order to keep the solution independent in the two coordinates.

The following independent conditions are obtained:

$$\frac{\partial q_x}{\partial z} = 1, \quad \frac{\partial A_x}{\partial z} = -\frac{1}{2} \frac{A_x}{q_x}; \quad (2.37)$$

and

$$\frac{\partial q_y}{\partial z} = 1, \quad \frac{\partial A_y}{\partial z} = -\frac{1}{2} \frac{A_y}{q_y}. \quad (2.38)$$

The normalized electric field distribution is given by

$$E(x, y, z) = \left(\frac{2}{\pi w_x w_y} \right)^{0.5} \exp \left(-\frac{x^2}{w_x^2} - \frac{y^2}{w_y^2} - \frac{i\pi x^2}{\lambda R_x} - \frac{i\pi y^2}{\lambda R_y} + \frac{i\phi_{0x}}{2} + \frac{i\phi_{0y}}{2} - ikz \right), \quad (2.39)$$

where w_x , w_y , R_x , R_y , ϕ_{0x} , and ϕ_{0y} are defined analogously to w , R , and ϕ_0 previously. Noting that $x^2 + y^2 = r^2$, in the special case that the two beam waist radii are equal at the same value of z , this relation becomes identical to equation 2.31.

2.1.5 Confocal Distance

The Gaussian beam parameters can be described particularly simply when expressed in terms of the confocal distance [12]

$$z_c = \frac{\pi w_0^2}{\lambda}. \quad (2.40)$$

This parameter is also known as the Rayleigh range. Using the confocal distance, the Gaussian beam parameters can be rewritten as

$$R = z + \frac{z_c^2}{z}, \quad (2.41)$$

$$w = w_0 \left[1 + \left(\frac{z}{z_c} \right)^2 \right]^{0.5}, \quad (2.42)$$

$$\phi_o = \tan^{-1} \left(\frac{z}{z_c} \right). \quad (2.43)$$

The confocal distance is the distance from the beam waist along the propagation axis at which the cross-sectional area is twice that at the waist [19].

2.1.6 Edge Taper

The distribution of the electric field perpendicular to the z axis is given by

$$\frac{|E(r, z)|}{|E(0, z)|} = \exp \left[-\left(\frac{r}{w} \right)^2 \right], \quad (2.44)$$

where r is the distance from the propagation axis. In terms of power density, the distribution is given by

$$\frac{|P(r, z)|}{|P(0, z)|} = \exp \left[-2 \left(\frac{r}{w} \right)^2 \right]. \quad (2.45)$$

The fundamental Gaussian beam mode can be characterized in terms of the relative power level at a certain radius. This is known as the edge taper T_e , and is given by

$$T_e = \frac{P(r_e)}{P(0)}, \quad (2.46)$$

where r_e is the radius of the edge taper. From equation 2.45,

$$T_e(r) = \exp \left(-\frac{2r_e^2}{w^2} \right). \quad (2.47)$$

In order to efficiently accommodate a large range, the edge taper is commonly expressed in decibels, so

$$T_e(\text{dB}) = 10 \log_{10}(T_e). \quad (2.48)$$

The edge taper is often used to specify a certain relative power density at the edge of a reflector. Usually the optics are designed to have a minimum $4w$ size to minimize beam truncation. This corresponds to -34 dB loss at the reflector edge.

2.2 Higher Order Gaussian Beam Modes

The fundamental Gaussian beam solutions given above are the simplest and most widely used solutions to the paraxial wave equations describing the propagation of a quasioptical beam. However, in reality electric field distributions are much more complex than a fundamental Gaussian beam. Additional solutions are often needed to accurately describe the beam. These solutions, which have a more complex variation of the electric field perpendicular to axis of propagation, can be analysed using higher order Gaussian beam mode solutions. They are formed by superimposing various polynomials on the fundamental Gaussian beam solution, as will be shown

in the following sections. An important application of higher order modes is the accurate description of the beam from a corrugated feed horn. In this case, they are necessary because, although there is high axial symmetry, the radiation pattern is not perfectly Gaussian. The pattern is usually 98% Gaussian.

2.2.1 Higher Order Modes in Cylindrical Coordinates

In cylindrical coordinates, the additional variation of the electric field is accounted for by using a trial solution including additional terms that vary as a function of the polar angle φ (not to be confused with the phase shift ϕ_0) and the radius r . The trial solution can be written as

$$u(r, \varphi, z) = A(z) \exp\left(-\frac{ikr^2}{2q(z)}\right) S(r) \exp(im\varphi), \quad (2.49)$$

where $S(r)$ is an unknown radial function, and m is an integer. The solutions obtained for the paraxial wave equation are given by

$$S(r) = \left(\frac{\sqrt{2r}}{w}\right)^m L_{pm}\left(\frac{2r^2}{w^2}\right), \quad (2.50)$$

where w is the beam radius, as before, and L_{pm} is the generalized Laguerre polynomial. p and m represent variation in the radial and azimuthal directions respectively. The polynomials $L_{pm}(u)$ are solutions of Laguerre's equation [21]

$$u \frac{d^2 L_{pm}}{du^2} + (m+1-u) \frac{dL_{pm}}{du} + pL_{pm} = 0, \quad (2.51)$$

and can be found from the following expression:

$$L_{pm}(u) = \frac{e^u u^{-m}}{p!} \frac{d^p}{du^p} (e^{-u} u^{p+m}). \quad (2.52)$$

The first few Laguerre polynomials are

$$\begin{aligned}
 L_{0m}(u) &= 1, \\
 L_{1m}(u) &= 1 + m - u, \\
 L_{2m}(u) &= \frac{1}{2} [(2 + m)(1 + m) - 2(2 + m)u + u^2].
 \end{aligned} \tag{2.53}$$

The normalized electric field distribution for the pm Gauss-Laguerre beam mode is given by

$$\begin{aligned}
 E_{pm}(r, \varphi, z) &= \left(\frac{2p!}{\pi(p+m)} \right)^{0.5} \frac{1}{w(z)} \left(\frac{\sqrt{2}r}{w(z)} \right)^m L_{pm} \left(\frac{2r^2}{w^2(z)} \right) \\
 &\cdot \exp \left(-\frac{r^2}{w^2(z)} - \frac{i\pi r^2}{\lambda R(z)} - i(2p+m+1)\phi_0(z) - ikz + im\varphi \right),
 \end{aligned} \tag{2.54}$$

where the beam radius w , the radius of curvature R , and the phase shift ϕ_0 are the same as for the fundamental Gaussian beam mode.

2.2.2 Higher Order Modes in Rectangular Coordinates

In rectangular coordinates, the higher order modes are obtained by including additional functions dependent on x and y . As the general two-dimensional mode is the product of two one-dimensional modes, it is convenient to start with just the x coordinate. The trial solution is

$$u(x, z) = A(z) H \left(\frac{\sqrt{2}x}{w(z)} \right) \exp \left(-\frac{ikx^2}{2q(z)} \right), \tag{2.55}$$

where w and q are defined as before. H satisfies Hermite's differential equation

$$\frac{d^2H(u)}{du^2} - 2u \frac{dH(u)}{du} + 2mH(u) = 0, \tag{2.56}$$

where m is a non-negative integer. This equation defines the Hermite polynomial $H_M(u)$ of order m . Given the Hermite polynomials $H_0(u)$ and $H_1(u)$ are respectively

1 and $2u$, the remaining polynomials can be obtained from

$$H_{n+1} = 2(uH_n(u) - nH_{n-1}(u)). \quad (2.57)$$

They can also be found from the following expression:

$$H_n(u) = (-1)^n e^{u^2} \frac{d^n}{du^n} (e^{-u^2}). \quad (2.58)$$

The first few Hermite polynomials are

$$\begin{aligned} H_0(u) &= 1, \\ H_1(u) &= 2u, \\ H_2(u) &= 4u^2 - 2, \\ H_3(u) &= 8u^3 - 12u, \\ H_4(u) &= 16u^4 - 48u^2 + 12. \end{aligned} \quad (2.59)$$

The normalized electric field distribution for the one dimensional Gauss-Hermite beam mode of order m is given by

$$\begin{aligned} E_m(x, z) &= \left(\frac{2}{\pi}\right)^{0.25} \left(\frac{1}{w_x 2^m m!}\right)^{0.5} H_m\left(\frac{\sqrt{2}x}{w_x}\right) \\ &\exp\left(-\frac{x^2}{w_x^2} - \frac{i\pi x^2}{\lambda R_x} + \frac{i(2m+1)\phi_{0x}}{2} - ikz\right). \end{aligned} \quad (2.60)$$

Finally, the two-dimensional case is achieved by using a trial solution formed from the product of individual functions like equation 2.60 in x and y . The normalized electric field distribution for the two-dimensional mn Gauss-Hermite beam mode is given by

$$\begin{aligned} E_{mn}(x, y, z) &= \left(\frac{1}{\pi w_x w_y 2^{m+n-1} m! n!}\right)^{0.5} H_m\left(\frac{\sqrt{2}x}{w_x}\right) H_n\left(\frac{\sqrt{2}y}{w_y}\right) \\ &\exp\left(-\frac{x^2}{w_x^2} - \frac{y^2}{w_y^2} - \frac{i\pi x^2}{\lambda R_x} - \frac{i\pi y^2}{\lambda R_y} + \frac{i(2m+1)\phi_{0x}}{2} + \frac{i(2n+1)\phi_{0y}}{2} - ikz\right). \end{aligned} \quad (2.61)$$

2.3 Ray Transfer Matrix Analysis

Section 2.1 outlines the free space propagation of a Gaussian beam. However, in a quasioptical system, there will be elements such as mirrors and lenses which will need to be described. Ray transfer matrix analysis, which is adapted from geometrical analysis, is used to efficiently model this beam transformation. This is also known as ABCD matrix analysis due to the use of these letters to denote the matrix elements.

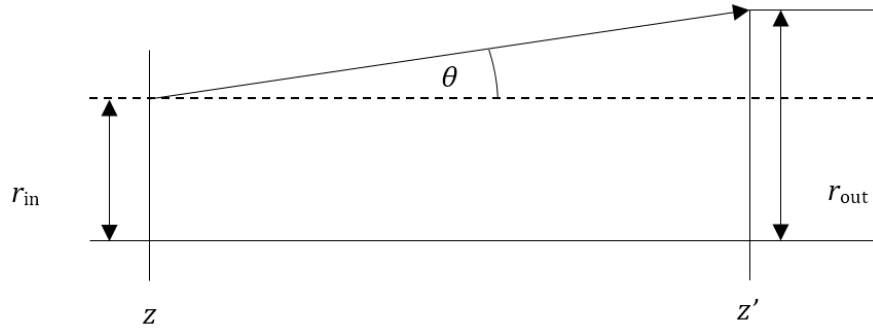


Figure 2.2: Ray propagation in free space, showing r_{in} and r_{out} . The angle θ is equal to the slope r' in the paraxial limit.

By denoting the position of a ray as r_{in} , and its slope relative to the axis of propagation as r'_{in} (figure 2.2), the relationship between the input and output ray position and slope can be written as [12]

$$\begin{pmatrix} r_{out} \\ r'_{out} \end{pmatrix} = \begin{pmatrix} A & B \\ C & D \end{pmatrix} \begin{pmatrix} r_{in} \\ r'_{in} \end{pmatrix}. \quad (2.62)$$

The slope here is the slope of rays relative to the z axis, which is equivalent to the angle for the small angles considered in the paraxial approximation, where $\tan \theta \approx \theta$. The radius of curvature is defined by $R = r/r'$, so the following equation can be used to determine the output radius:

$$R_{out} = \frac{AR_{in} + B}{CR_{in} + D}. \quad (2.63)$$

This is extended to quasioptical systems by using q , the complex beam parameter [22], giving

$$q_{\text{out}} = \frac{Aq_{\text{in}} + B}{Cq_{\text{in}} + D}. \quad (2.64)$$

The reciprocal form of this equation is often more convenient to use:

$$\frac{1}{q_{\text{out}}} = \frac{C + D/q_{\text{in}}}{A + B/q_{\text{in}}}. \quad (2.65)$$

The beam width w , and the radius of curvature R can thus be determined:

$$w = \left[\frac{\lambda}{\pi \text{Im}(-1/q)} \right]^{0.5} \quad (2.66)$$

$$R = \left[\text{Re} \left(\frac{1}{q} \right) \right]^{-1} \quad (2.67)$$

The phase slippage $\Delta\phi_0$, which is defined as the difference between the phases of the incident and output beams, is given by the argument of a combination of the matrix elements A and B , and the incident complex beam parameter q_{in} :

$$\Delta\phi_0 = -\text{Arg} \left(A + B \left(\frac{1}{q_{\text{in}}} \right) \right). \quad (2.68)$$

ABCD matrix analysis is extremely useful in quasioptical analysis, as it means that the ray theory of geometrical optics can be applied to systems at millimetre and sub-millimetre wavelengths. Each element of a system has a unique ABCD matrix; these are multiplied together to determine the overall system matrix. The order of multiplication is such that the rightmost matrix describes the first element at the input, and the following matrices are placed to its left.

The following table gives the ray transformation matrices for some of the most commonly used components in quasioptical systems [12].

Element	Matrix	Comment
Propagation in free space	$\begin{pmatrix} 1 & d \\ 0 & 1 \end{pmatrix}$	d is the propagation distance.
Reflection from a flat mirror	$\begin{pmatrix} 1 & 0 \\ 0 & 1 \end{pmatrix}$	For mirrors perpendicular to the beam.
Reflection from a curved mirror	$\begin{pmatrix} 1 & 0 \\ -\frac{2}{R} & 1 \end{pmatrix}$	R is the radius of curvature. $R > 0$ for a convex mirror.
Refraction at a flat interface	$\begin{pmatrix} 1 & 0 \\ 0 & -\frac{n_1}{n_2} \end{pmatrix}$	n_1 is the initial refractive index and n_2 is the final refractive index.
Refraction at a curved interface	$\begin{pmatrix} 1 & 0 \\ \frac{n_1 - n_2}{Rn_2} & \frac{n_1}{n_2} \end{pmatrix}$	R is the radius of curvature; n_1 and n_2 are the refractive indices.
Thin lens	$\begin{pmatrix} 1 & 0 \\ -\frac{1}{f} & 1 \end{pmatrix}$	f is the focal length. $f > 0$ for a converging lens. Only valid if $f \gg$ lens thickness.

Table 2.1: ABCD matrices for commonly used optical components.

In order to illustrate the application of the ABCD matrix technique, a Gaussian beam telescope is outlined below. The Gaussian beam telescope consists of two lenses of focal lengths f_1 and f_2 separated by a distance $d = f_1 + f_2$ such that their foci are coincident. Furthermore, the input is taken to be f_1 from the first lens, and the output is taken to be f_2 from the second lens, although it is not necessary that a beam waist exists at this point. This is illustrated in figure 2.3 below.

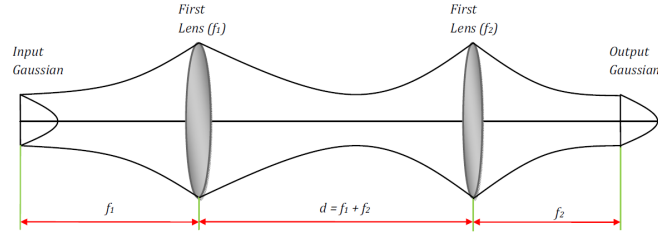


Figure 2.3: Gaussian Beam Telescope [23].

The combined ABCD matrix for this arrangement is

$$M = \begin{pmatrix} 1 & f_2 \\ 0 & 1 \end{pmatrix} \begin{pmatrix} 1 & 0 \\ -\frac{1}{f_2} & 1 \end{pmatrix} \begin{pmatrix} 1 & f_1 + f_2 \\ 0 & 1 \end{pmatrix} \begin{pmatrix} 1 & 0 \\ -\frac{1}{f_1} & 1 \end{pmatrix} \begin{pmatrix} 1 & f_1 \\ 0 & 1 \end{pmatrix}, \quad (2.69)$$

which simplifies to

$$M = \begin{pmatrix} -\frac{f_2}{f_1} & 0 \\ 0 & -\frac{f_1}{f_2} \end{pmatrix}. \quad (2.70)$$

The complex beam parameter can then be found using equation 2.64:

$$q_{\text{out}} = \left(\frac{f_2}{f_1}\right)^2 q_{\text{in}}, \quad (2.71)$$

and the output beam parameters can hence be determined:

$$\begin{aligned} R_{\text{out}} &= \left(\frac{f_2}{f_1}\right)^2 R_{\text{in}}; \\ w_{\text{out}} &= \left(\frac{f_2}{f_1}\right) w_{\text{in}}. \end{aligned} \quad (2.72)$$

These parameters are independent of wavelength, and are only dependent on the focal lengths of the lenses. As the B matrix element is zero, the argument for the phase shift becomes real, so $\Delta\phi_0 = \pi$.

2.4 Analysis of Antenna Systems

2.4.1 Telescope

The antenna system dealt with in this thesis is a large Cassegrain reflecting antenna, which is designed to couple radiation from the sky to a focal plane through a series of quasioptical elements in a cryostat receiver near the focal plane. The radiation is fed to a horn antenna, which in this case is a conical corrugated horn, and the detector is a waveguide probe. By the principle of reciprocity, optical systems operate equivalently whether they are receiving or transmitting [24]. Therefore, when designing the system, coupling a beam from the telescope to the horn antenna is equivalent to propagating a beam from the horn back in the direction of the sky through the telescope [23].

2.4.2 Conical Corrugated Horn

In order to accurately analyse an antenna system, it is necessary to have an accurate description of the source field. There is a large variety of antenna feed horns, all with different field distributions and beam mode expansions. The conical corrugated horn is a very common type of feed horn. These horns produce circularly symmetric beams, and their field distributions can be expanded in terms of Laguerre-Gaussian modes. The horn propagates a waveguide mode known as the hybrid HE_{11} mode [12]. The corrugations in the horn are designed to produce an infinite reactance on the metallic surface to prevent the establishment of currents. Bandwidth is limited as the reactance condition is frequency dependent.

The linearly polarized field distribution for a circularly symmetric waveguide can be approximated to a good level by [25]

$$E(r) = J_0\left(\frac{2.405r}{a}\right). \quad (2.73)$$

where r is the distance from the central axis, a is the waveguide radius, and J_0 is the zero order Bessel function. The horn is said to be operating in the balanced hybrid mode condition. At the aperture, there is also a spherical phase curvature term which is defined by the radial length of the horn, R_h , so

$$E(r) = J_0\left(\frac{2.405r}{a}\right) \exp\left(-i \frac{\pi r^2}{\lambda R_h}\right). \quad (2.74)$$

The normalized coupling coefficient for the fundamental Gaussian beam mode to this aperture field distribution can be expressed as [12]

$$c_p = 1.362s \int_{x=0}^{2/s^2} L_p(x) \exp\left(-\frac{x}{2}\right) J_0(st\sqrt{x}) dx, \quad (2.75)$$

where $x = 2r^2/w_0^2$, $s = w_0/a$, and $t = 2.405/\sqrt{2}$. This coupling coefficient is graphed in figure 2.4, which shows that the maximum coupling occurs where the beam radius $w = 0.6435a$ [26]. This gives a Gaussian power coupling coefficient (c_p^2) of 98%.

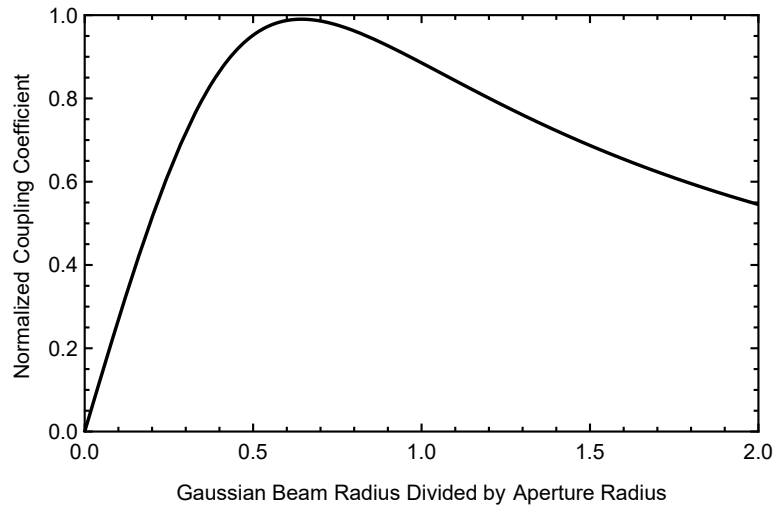


Figure 2.4: Coupling coefficient of the fundamental Gaussian beam mode to the truncated zero order Bessel function.

The field distribution can be expanded using Gauss-Laguerre beam modes:

$$E(r, \varphi) \approx \sum_{p=0} A_p E_{p0}(r, \varphi). \quad (2.76)$$

where E_{p0} represents beam modes with coefficients A_p of increasing order p .

The truncated Bessel function is used in conjunction with the ABCD matrices for a more accurate description of the system when compared with the fundamental Gaussian beams, and is used throughout the analysis presented in chapter 3.

2.4.3 Horn transition

In general, a conical horn will be attached to a rectangular waveguide, and reflection at the junction will need to be minimized [27]. The reflection coefficient on a transmission line is written as

$$|\rho| = \frac{Z_2 - Z_1}{Z_2 + Z_1}, \quad (2.77)$$

where Z_2 is the load impedance, and Z_1 is the source impedance. When ρ is minimized, the source and load impedance are equal, and are said to be matched. The field in a waveguide can be described in terms of transverse electric (TE) and transverse magnetic (TM) modes, which are linearly polarized hybrid modes [12]. The waveguide impedance for the TE and TM modes can be written as

$$Z_{TE} = \frac{Z_0}{\sqrt{1 - \left(\frac{\lambda}{\lambda_c}\right)^2}} = \frac{Z_0 \lambda_g}{\lambda}, \quad (2.78)$$

$$Z_{TM} = \sqrt{1 - \left(\frac{\lambda}{\lambda_c}\right)^2} = \frac{Z_0 \lambda}{\lambda_g}, \quad (2.79)$$

where Z_0 is free-space impedance, and λ_c and λ_g are cut-on and guide wavelengths respectively. Combining the above equations gives the following condition:

$$|\rho| = \frac{\lambda_{g2} - \lambda_{g1}}{\lambda_{g2} + \lambda_{g1}}, \quad (2.80)$$

where only the fundamental modes are being considered, as not much power is scattered to the higher order modes and 1 and 2 refer to such wavelengths in the same location. As the guide wavelength can be expressed in terms of the cut-on

wavelength, the condition can be achieved by equating the cut-on wavelengths for the rectangular and circular modes as follows:

$$\frac{2\pi}{\sqrt{\left(\frac{m\pi}{a}\right)^2 - \left(\frac{n\pi}{b}\right)^2}} = \frac{2\pi r_a}{p'_{xl}}, \quad (2.81)$$

where a and b are respectively the width and height of the rectangular waveguide, and R_a is the radius of the circular waveguide (i.e., the first part of the conical horn). m and n are the whole numbers of half wavelengths that fit in the a and b dimensions, and x and l are the radial and azimuthal orders of the circular TE modes. By substituting $m = 1$, $n = 0$ and $p'_{xl} = 1.84$, which are the values for the fundamental TE modes, the condition is met when

$$r_a = \frac{1.841a}{\pi}. \quad (2.82)$$

2.4.4 Beam coupling

Beam coupling is used to calculate how well a beam from an optical system corresponds with the beam representing ideal conditions. For example, it may be necessary to test a field distribution collected on an output grid from software such as GRASP (see section 2.5) at a telescope focal plane, and analyse its optical characteristics. Then, taking the actual beam that has been propagated through the system, a coupling calculation may be performed with an ideal equivalent beam to analyse how close the propagated beam is to the ideal beam. This coupling calculation might also reveal an insight into the amount of optical aberration in a beam.

For example, equation 2.83 represents the fundamental Gaussian beam mode:

$$E_{00} = \exp\left(-\frac{(x^2 + y^2)}{w^2} - \frac{ik(x^2 + y^2)}{2R}\right), \quad (2.83)$$

where w is the beam radius, and R is the radius of curvature.

The following formula is used to calculate a coupling coefficient, K_{00} [12]:

$$K_{00} = \left| \frac{\int_S F^* E_{00} ds}{\sqrt{\int_S F^* F ds \int_S E_{00}^* E_{00} ds}} \right|. \quad (2.84)$$

F is the field distribution which is being coupled to the fundamental Gaussian beam mode E_{00} in an area S . In practice, summations are used rather than integrals. The area should be large enough to cover all the power from the field distribution.

It is also possible to use the same equation to couple to other arbitrary beams, such as the top hat field from a telescope. In this case, the appropriate field is substituted for the Gaussian beam in equation 2.84.

2.5 Introduction to GRASP

While Gaussian beam mode analysis is a good representation of beam propagation in quasioptical systems, it does not provide sufficient accuracy when precise detail of the beam propagation is required, particularly for off-axis systems [20]. For example, off-axis propagation with reflectors is not dealt with fully as the mirrors are treated as thin lenses. For this reason, the Physical Optics (PO) technique is used in addition to Gaussian beams to more accurately characterize optical systems.

GRASP is an example of an electromagnetic simulation package which makes use of the PO technique, which is outlined below.

2.5.1 Physical Optics Analysis

Here, the analytical solutions of Maxwell's equations are considered, leading to a description of the PO approximation [28][29]. Maxwell's equations for a time har-

monic electromagnetic field can be expressed as follows:

$$\nabla \times \mathbf{E} = -i\omega\mu\mathbf{H}, \quad (2.85)$$

$$\nabla \times \mathbf{H} = i\omega\epsilon\mathbf{E} + \mathbf{J}, \quad (2.86)$$

where \mathbf{E} is the electric field, \mathbf{H} is the magnetic field strength, \mathbf{J} is the electric current density, ω is the angular frequency, μ is the permeability, and ϵ is the permittivity.

To solve these equations, solutions must be found for \mathbf{E} and \mathbf{H} due to a current source \mathbf{J} . To obtain a practical solution, vector potential functions are introduced.

The magnetic vector potential is related to the magnetic field by [23]

$$\mathbf{H} = \frac{1}{\mu} \nabla \times \mathbf{A}. \quad (2.87)$$

The electric field can also be described by this vector potential,

$$\mathbf{E} = \frac{1}{i\omega\mu\epsilon} \nabla(\nabla \cdot \mathbf{A}) - i\omega\mathbf{A}. \quad (2.88)$$

The magnetic vector potential satisfies the Helmholtz equation,

$$\nabla^2 \mathbf{A} + k^2 \mathbf{A} = -\mu\mathbf{J}, \quad (2.89)$$

where k is the wavenumber. The solution for equation 2.89 is found by integrating the effects of the elemental currents. It gives the magnetic vector potential \mathbf{A} due to the current density \mathbf{J} ,

$$\mathbf{A} = \frac{\mu}{4\pi} \int_S \mathbf{J} \frac{e^{ikr}}{r} ds, \quad (2.90)$$

where ds is the infinitesimal source element surface and S is the surface over which the integration is carried out. e^{ikr}/r is a Green's function. This results in

$$\mathbf{A} = \frac{\mu}{4\pi} \frac{e^{ikr}}{r}. \quad (2.91)$$

The total field can be found using this result and equations 2.87 and 2.88, such that

$$\mathbf{E} = -i \frac{\omega \mu}{4\pi} \iint_S [\mathbf{J}G + \frac{1}{k^2} (\mathbf{J} \cdot \nabla) \nabla G] ds, \quad (2.92)$$

$$\mathbf{H} = \frac{1}{4\pi} \iint_S [\mathbf{J} \times \nabla G] ds, \quad (2.93)$$

where $G = e^{ikr}/r$.

Once the current density is known, equations 2.92 and 2.93 give the electric and magnetic fields. Appropriate approximations are used to calculate the near and far fields of the radiated field. The following relation applies to a radiated field from a scatterer surface:

$$\mathbf{E}_{\text{tot}} = \mathbf{E}_{\text{inc}} + \mathbf{E}_{\text{scat}}, \quad (2.94)$$

where \mathbf{E}_{tot} is the total electric field, \mathbf{E}_{inc} is the incident electric field, and \mathbf{E}_{scat} is the scattered electric field.

To calculate the scattered electric field, the first step is to calculate the currents on the surface of the scatterer. These currents are induced by the incident electric field. The scattered field must then be calculated from the current distributions. Finally, the total field is found by combining the incident and scattered fields.

The PO approximation simplifies the calculation of the induced currents on the scatterer. The scatterer is assumed to be large when compared with the wavelength. This means that the induced currents are calculated as if they were on an infinite plane surface. Each current element is locally expressed as

$$\mathbf{J} = 2\hat{n} \times \mathbf{H} \quad (2.95)$$

where \hat{n} is the unit vector normal to the scatterer surface, and \mathbf{H} is the incident magnetic field. This will give accurate results as long as the radius of curvature is large compared with the wavelength. The fields are calculated as 2-dimensional

numerical integrations. In GRASP, the integration area of the scatterer is defined by its rim, which here is the circle which determines the edge of the mirror.

Cross-polarization

To fully characterize the reflecting elements in a system, it is necessary to consider the effect on the polarization of the incident beam, assumed to be linearly polarized. Cross-polarization levels are used to describe power leaking from the linear polarization state of interest to the orthogonal state of polarization. This describes the component of the field orthogonal to what is called co-polarization, which is in the main polarization plane of interest. Ludwig's third definition is conventionally used to define the reference polarization [30]. In this definition, the reference polarization is taken to be that of a Huygen's source, i.e. electric and magnetic tangential field components that lie in the aperture plane, radiating equal, equiphase fields along the z axis. The direction of cross-polarization is obtained by rotating the source 90° in the aperture plane. The co-polar and cross-polar components are given by

$$E_{cop} = E_\theta \cos \theta \cos \phi - E_\phi \sin \phi \approx E_\theta \cos \phi - E_\phi \sin \phi, \quad (2.96)$$

$$E_{xsp} = E_\theta \cos \theta \sin \phi + E_\phi \cos \phi \approx E_\theta \sin \phi + E_\phi \cos \phi. \quad (2.97)$$

It is desirable to keep the cross-polar levels low.

Physical Theory of Diffraction

The PO approximation only holds when the surface on which the induced currents are calculated can be locally defined as planar. As this does not hold at the truncated edges of a scatterer, the edge effects of the field are not truly accounted for by the PO technique. Instead, the Physical Theory of Diffraction (PTD) is used to calculate the currents at these edge. GRASP makes use of the PTD technique by calculating the

edge currents among the illuminated edge of the scatterer for incremental surface area strips. The PTD contributions are then separated into the TE and TM components, which are combined to give the local field. The PTD approximation is valid when the local incident field at the edge of the scatterer behaves as a plane wave. Using the PTD technique improves the accuracy when the reflectors have a moderate degree of truncation. The combined PO and PTD field calculations provide very accurate results for the fields scattered by reflectors illuminated by radiation from long wavelength sources such as feed horns. This provides much more accurate results than using the PO method alone, as shown in [23]. In Chapter 3 of this thesis, the predicted fields were generated using the combined PO and PTD technique in GRASP.

2.5.2 System Generation in GRASP

A system can be both implemented and analysed in GRASP using TICRA Object Repository (*.tor) and TICRA Command Input (*.tci) files. These files form the basis of a GRASP project file. The *.tor files describe the objects in the system and the *.tci files describe the list of analysis calculation commands to be implemented. These files are created using the graphical user interface in the GRASP pre-processor. It is also possible to plot the system in 3D, and perform limited planar and contour plots of the output beams. The post-processor can be used to plot the output fields, or they can be analysed using an external program such as Mathematica. Each element in GRASP is defined at a local coordinate system using a set of properties specific to that element. The descriptions following are of those elements that were of most importance for the research reported in this thesis.

2.5.3 GRASP Input Sources

To analyse beam characteristics, a source of electromagnetic radiation needs to be defined in GRASP. The input sources are subsequently propagated through the system. The following three methods were used to define input horn fields [31]. Two of them are generated internally by GRASP, and the third uses an externally defined field.

Gaussian Beam

This method defines a feed which radiates a Gaussian beam using the near-field parameters of the Gaussian beam. It provides a field with a Gaussian taper, and truncates the beam at the edge of the aperture. It satisfies Maxwell's equations in both the near and far fields. This is used as a simple model for the radiation from a corrugated horn. A corrugated horn has 98% of its power in an equivalent Gaussian which is scaled to the right size to represent it. The beam radius and the phase front radius are the parameters required, illustrated in Figure 2.5

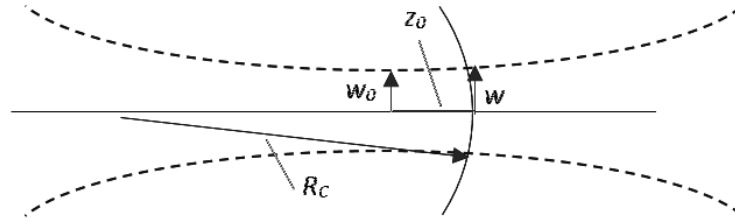


Figure 2.5: Gaussian Beam, Near field definition; R_C = phase front radius, w_0 = beam waist radius, w = beam radius at desired plane, z_0 = distance from beam waist

The beam radius w and the phase front radius are related to the beam waist w_0 and the position of the waist at $-z_0$ by

$$w = w_0 \sqrt{1 + z_0^2 / b^2}, \quad (2.98)$$

$$R_C = z_0 (1 + b^2 / z_0^2), \quad (2.99)$$

where the confocal distance $b = w_0^2 k / 2$ and the wavenumber $k = 2\pi / \lambda$.

Hybrid Mode Conical Horn

This is a more accurate description of the radiation produced from a conical corrugated horn (see section 2.4.2). The horn is operating under the balanced-hybrid condition and has a narrow flare angle. The parameters required are the aperture radius, the semi-flare angle, and the distance to the phase centre of the horn. The hybrid modes HE_{mn} and EH_{mn} , and the cylindrical modes TE_{0n} and TM_{0n} are supported. As has already been mentioned, the conical corrugated horn typically propagates only the hybrid HE_{11} mode.

Tabulated Planar Source

This option is used when an external user defined vector source field is required. The files used store field values in a rectangular grid. For the analysis presented in Chapter 4, the grid files were produced using the mode matching software *Scatter*, which was developed by the Terahertz Optics and Technology Group in Maynooth [32]. The basis of the mode matching technique used by *Scatter* is splitting a horn into segments of increasing radius, and considering the propagation of the appropriate waveguide modes through each section. At each junction between sections of different radii, an overlap integral is performed to provide the level of coupling between the modes. The modes are then recombined to provide the resulting field.

Scatter offers an excellent prediction of the aperture vector field distributions [33]. As a result, it is more desirable to use it for the source field than the Gaussian Beam or Hybrid Mode Conical Horn in GRASP. The mode matching code accurately predicts co-polar and cross-polar levels of the horn, and GRASP allows full vector free space analysis.

2.5.4 Reflectors

Reflector objects are defined in GRASP using a surface object and a rim object. The rim describes the edge of the scatterer.

Elliptical reflectors are used to image a beam waist from one plane to another plane. Parabolic reflectors are used when parallel beams need to be brought to a focus.

An ellipsoid is generated by rotating an ellipse about one of its axes. The distances R_1 and R_2 from the focal points to the point of reflection on the surface are related as follows:

$$\frac{1}{f} = \frac{1}{R_1} + \frac{1}{R_2}, \quad (2.100)$$

where f is the focal length determined from the ABCD matrices, where the mirrors are treated as on-axis lenses. In the initial geometric design of a system, R_1 is determined by adding the distance between the phase centre and the horn aperture to the distance between the horn aperture and the first mirror.

A beam from the first focal point will travel a distance of R_1 before reflecting off the surface and travelling a distance of R_2 to the second focal point. This typical optical train is represented below in figure 2.6, along with the defining parameters of the ellipse: the semi-major axis a , the semi-minor axis b , the linear eccentricity (half the interfocal distance) c , and the two focal points F_1 and F_2

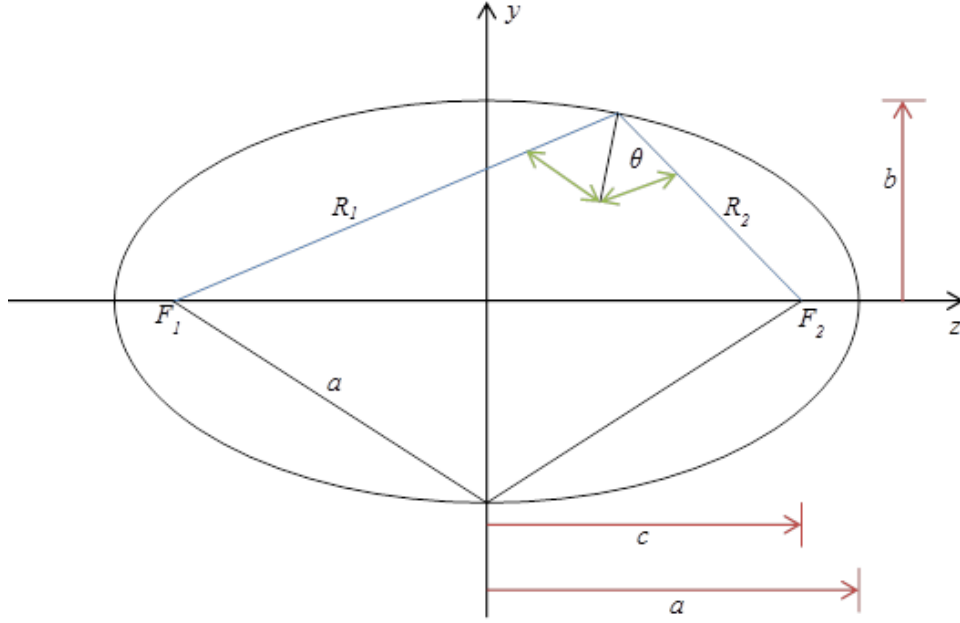


Figure 2.6: Ellipse parameters

Using R_1 , R_2 , and θ , the angle of reflection, the semi-major axis a , semi-minor axis b , linear eccentricity c , eccentricity e , and the ellipsoid's radius of curvature Rad , are then determined:

$$a = \frac{R_1 + R_2}{2}, \quad (2.101)$$

$$b = \sqrt{R_1 R_2 \cos(\theta)}, \quad (2.102)$$

$$c = \sqrt{a^2 - b^2}, \quad (2.103)$$

$$e = \sqrt{1 - \frac{b^2}{a^2}}, \quad (2.104)$$

$$Rad = a(1 - e^2). \quad (2.105)$$

The defining polynomial for the ellipsoid is

$$\frac{x^2 + y^2}{2Rad} + \frac{(1 - e^2)z^2}{2Rad} + z = 0. \quad (2.106)$$

This equation may be implemented in GRASP as a 2nd order quadric polynomial surface to define the mirror surface. The origin is one of the vertices of the ellipsoid.

The surface must then be rotated so the mirror is in the correct position.

2.5.5 Verification of GRASP using the VNA

A vector network analyser (VNA) characterizes a device under test by measuring its effect on the amplitude and phase of test signals. Generally, the reflection and transmission of the applied device under test is measured. For example, in a two-port system, a test signal from port 1 may be incident on the device, with the response measured at port 2. If a is the incident wave from port 1, and d is the response at port 2, the transmitted power $|S_{21}|$ may be calculated by the scattering matrix in the following equation:

$$\begin{pmatrix} b \\ d \end{pmatrix} = \begin{pmatrix} S_{11} & S_{12} \\ S_{21} & S_{22} \end{pmatrix} \begin{pmatrix} a \\ c \end{pmatrix}. \quad (2.107)$$

The VNA at the Maynooth Department of Experimental Physics uses a Rohde and Schwarz ZVA-24 system, which corresponds to a frequency range of 10 MHz–24 GHz. The in-house system incorporates two ZVA-Z110 W-band (75 GHz–110 GHz) converter heads in order to step up the frequency to the Terahertz region. The signal is split into two identical waves, and one is transmitted to the device under test, while the other is transmitted to the reference channel. The VNA system must be calibrated before any measurements may be taken.

For the purpose of comparing a GRASP simulation with an experimental measurement, the beam pattern of a pyramidal horn was measured using the VNA, and an equivalent simulation was made in GRASP, using physical measurements of the horn. In addition, for a tolerance analysis, the dimensions of the horn were reduced by 0.1 mm, and increased by 0.1 mm to account for any possible errors taken during measurement of the horn dimensions. This is illustrated in figure 2.7, which clearly shows the presence of the VNA-generated beam within these tolerances (GRASP Max, GRASP Min), especially in the y cut, where more deviation is evident in the GRASP-generated beams.

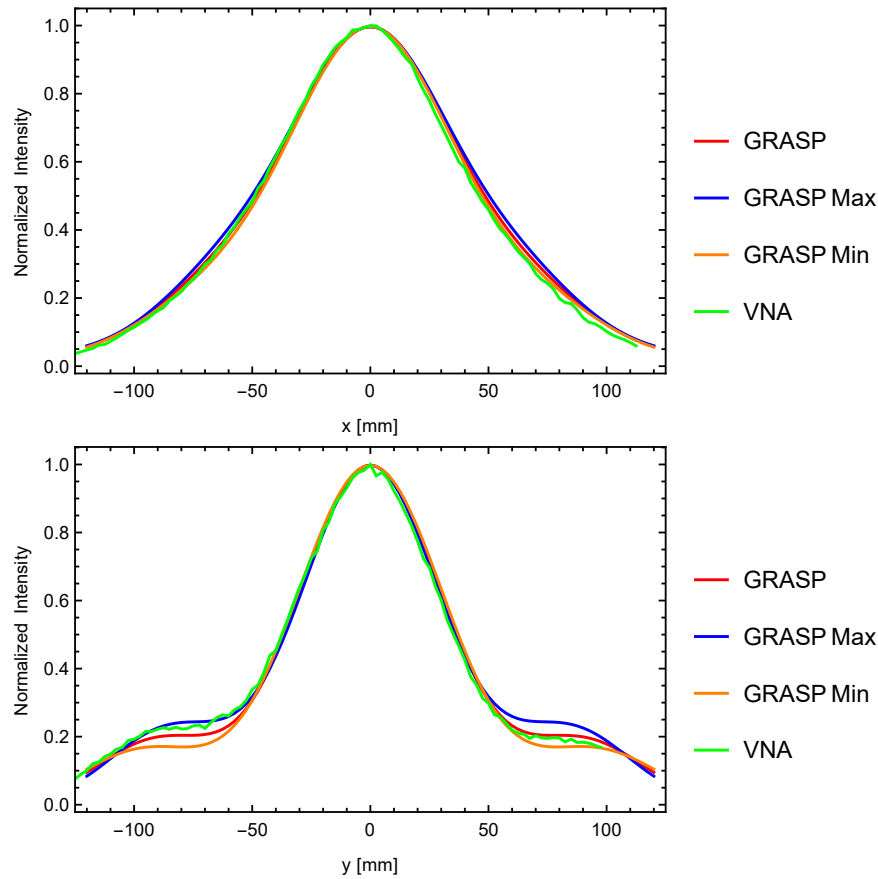


Figure 2.7: Cuts of the field generated by the VNA compared with those generated with GRASP

2.6 Conclusion

In this chapter, the background theory and optical analysis techniques were introduced. Gaussian Beam Mode Analysis and the PO technique employed by GRASP were presented, as they form the basis of the analysis of the Onsala 4 mm receiver presented in Chapters 3 and 4. The theory behind antenna systems and horn antennae was also outlined. A brief experimental verification of GRASP using a vector network analyser was performed.

Chapter 3

Onsala 4 mm Receiver

Contents

3.1 Onsala Space Observatory	45
3.1.1 25 m and 20 m Telescopes	45
3.1.2 20 m Telescope Optics	48
3.2 4 mm Receiver	49
3.2.1 Design Requirements	50
3.2.2 Horn Design	54
3.2.3 Further Design Considerations	56
3.3 Initial Optical Analysis	58
3.4 Truncation Analysis	61
3.5 Optical Efficiency	68
3.6 Conclusion	70

This chapter concerns the optical design design and analysis of a 4 mm receiver channel for the 20 m telescope at Onsala Space Observatory, Onsala, Sweden. The 4 mm receiver was installed in October 2015, and is designed to operate between 67 and 86 GHz. This receiver was installed parallel to the 3 mm receiver channel [34], which was installed in March 2014 [35]. The Department of Experimental Physics at Maynooth was invited to design the 4 mm system; the author’s specific contribution was the optical design and verification of the receiver. Eimante Kalinauskaite worked in parallel at Maynooth on the design of the conical corrugated horn, which is the antenna of choice. This work was done from autumn 2014 to summer 2015. The system was then manufactured and tested. The first light was observed in October 2015.

3.1 Onsala Space Observatory

Onsala Space Observatory (OSO) [36], which was founded in 1949 by Olaf Rydbeck, is the Swedish National Facility for Radio Astronomy. It is associated with the Department of Earth and Space Scientists at Chalmers University of Technology which operates it on behalf of the Swedish research council [37]. The observatory participates in a number of international projects, including LOFAR (Low Frequency Array) [38] and ALMA (Atacama Large Millimeter Array) [39].

3.1.1 25 m and 20 m Telescopes

There are two Cassegrain telescopes at Onsala, one with a 20 m antenna and one with a 25 m antenna. The two telescopes provide the possibility to perform high resolution spectroscopy at frequency range 0.8 – 116 GHz. The 25 m telescope, which operates in the range 0.8 – 6.7GHz, is shown in figure 3.1. The receivers and operating frequency ranges of the 25 m telescope are shown in table 3.1.



Figure 3.1: The 25 m telescope.

Frequency range (GHz)	Temperature (K)	Receiver type	Polarization
0.8-1.2	100	HEMT amplifier	Dual
1.2-1.8	30	HEMT amplifier	Dual
4.5-5.3	80	FET amplifier	Dual
6.0-6.7	80	HEMT amplifier	Dual

Table 3.1: Receivers in the 25 m telescope [40]

The 20 m telescope, which is analysed in this thesis, is enclosed in a 30 m diameter radome which protects it from the weather. This is shown in figure 3.2. The telescope operates in the range 2.2 – 116 GHz; the receivers, including the 4 mm receiver recently designed at Maynooth, and their operating frequency ranges are shown in table 3.2.



Figure 3.2: Exterior of the 20 m telescope.



Figure 3.3: The 20 m telescope inside the radome [41].

Frequency range (GHz)	Temperature (K)	Receiver type	Polarization
2.2-2.4	60	HEMT amplifier	Single
8.2-8.4	80	HEMT amplifier	Dual
18.0-26.0	30	HEMP amplifier	Dual
26.0-36.0	50	HEMT amplifier	Single
36.0-49.8	50	HEMT amplifier	Dual
67-87 ("4 mm") ^a	50-60	HEMT amplifier	Dual
85-116 ("3 mm")	50-60	SIS mixer	Dual

Table 3.2: Receivers in the 20 m telescope [42]

^aDesigned at Maynooth

3.1.2 20 m Telescope Optics

Figure 3.3 shows the interior of the radome, with the primary reflector of the 20 m telescope clearly visible.

The 20 m telescope follows a traditional Cassegrain design; this is illustrated in figure 3.4.

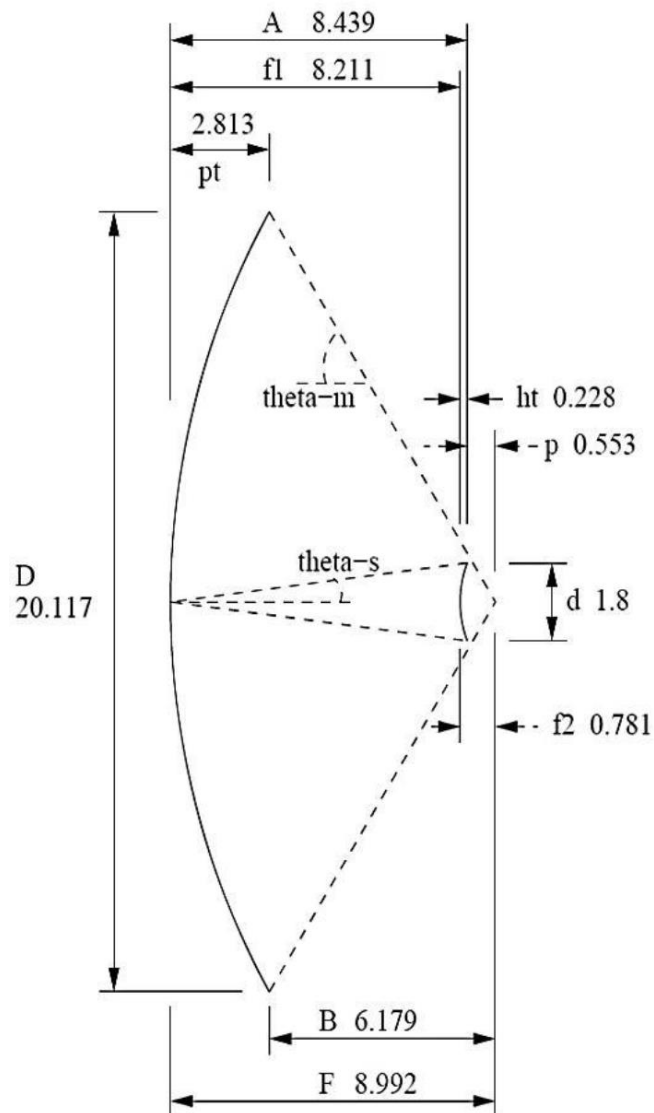


Figure 3.4: Layout of the 20 m Cassegrain telescope at Onsala Space Observatory. Dimensions are given in metres [43].

3.2 4 mm Receiver

As shown in Table 3.2, the 3 mm channel was designed to operate between 85 GHz and 116 GHz [43], whereas the 4 mm receiver channel was to operate between 67 GHz and 86 GHz.

The main observation goal of the 4 mm channel is to study deuterated molecules in the interstellar medium, many of which have not been extensively surveyed before by any telescope [35]. A list of important spectral lines in this frequency band is given in Table 3.3, including these important deuterated molecules.

Substance	Rest frequency (GHz)	Bandwidth (GHz)
Deuterated formylium (DCO^+)	72.039	71.97 - 72.11
Deuterium cyanide (DCN)	72.415	72.34 - 72.49
Cyanoacetylene (HC_3N)	72.784	72.71 - 72.86
Methyl cyanide (CH_3CN)	73.59	73.51 - 73.66
Deuterated water (HDO)	80.578	80.50 - 80.66
Cyanoacetylene (HC_3N)	81.881	81.80 - 81.96
Cyclopropenylidene (C_3H_2)	82.966	82.88 - 83.05

Table 3.3: Important Spectral lines in the 4 mm band [44].

The 4 mm receiver was installed in October 2015. Scientific verification observations were performed in the early months of 2016, which indicate its success. The receiver was used for the following projects [42]:

- W. Vlemmings et al.: A new circumstellar water maser at 67.8 GHz.
- E. De Beck et al.: The molecular content of supergiant outflows: a legacy of the history and future of massive stars.
- T. Danilovich et al.: The sulphur chemistry in circumstellar envelopes of oxygen-rich AGB stars.

- W. Geppert et al.: Search for water clusters in massive star-forming regions.
- P. Bjerkeli et al.: An unbiased 4mm spectral survey of the Class 0 protostar NGC 1333 IRAS 2A.
- W. Geppert et al.: Mapping of formaldehyde in star-forming regions.
- E. Wirström et al.: Deuteration in Barnard 5.
- J. Black et al.: Atmospheric emission lines for science verification at 4 mm wavelength.
- M. Hajigholi et al.: DCO+/DCN in the outer and inner galaxy.

3.2.1 Design Requirements

The following are the primary requirements for the optical design. There are mechanical constraints associated with the design as the optical train is to fit within a cryostat unit. The cylindrical cryostat unit was initially designed with half the space allocated for the 3 mm channel. The remaining space is for the development of the additional 4 mm channel. A cross-sectional drawing of the cryostat unit is presented in figure 3.5, which illustrates the geometry of the space. The L-shaped blue area indicates the volume available for the 4 mm receiver channel.

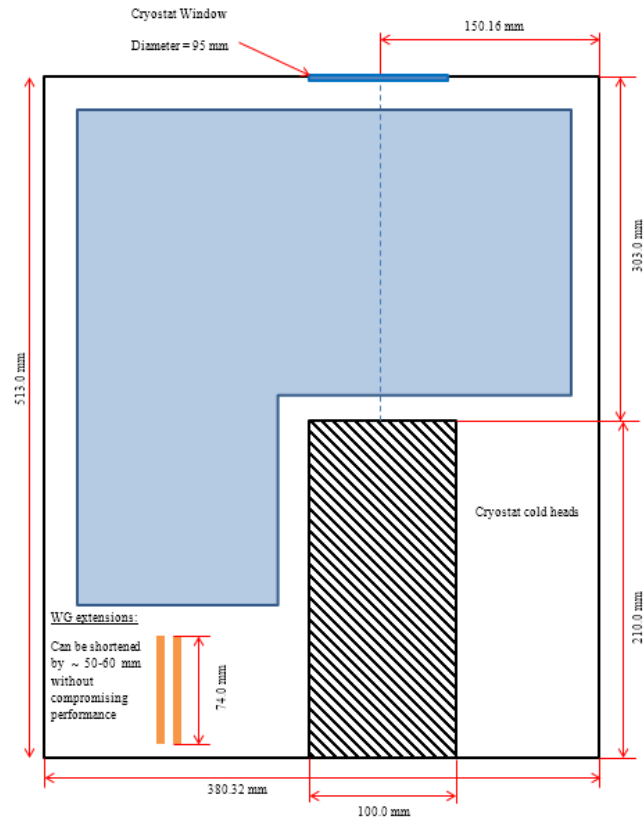


Figure 3.5: Geometrical layout of the cryostat unit to house the 4 mm receiver channel and optical system [34].

Further requirements are low cross polar levels of less than -30 dB relative to maximum copolar levels, low power truncation of -30 dB at the optical components and windows, and an edge taper of -12 dB at the secondary mirror in order to give high coupling efficiency to the horn antenna. There is an additional requirement of wavelength independent coupling between the horn aperture and the antenna secondary mirror over the bandwidth of the channel. This requires the same beam radius at the secondary mirror at all frequencies across the band, so that the horn aperture is imaged onto the secondary mirror of the telescope.

The 3 mm and 4 mm receiver channels are housed in a cryostat which is located near the telescope's focal point (see figure 3.4). The cryostat is mounted such that the optics coupling the two receiver channels are equivalently off-axis from the central focal point. The upper plate of the cryostat contains four cryostat windows. Two of these windows contain the front-end optics for the two receiver channels and the

remaining two contain cold calibration targets. There is a sliding mirror mechanism, which steers the beam towards either the antenna secondary mirror (for observation) or the cold targets (for calibration). This mechanism, and its effect on the beams, is illustrated in figure 3.6.

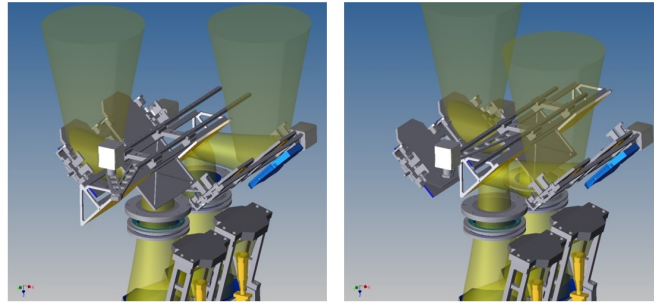


Figure 3.6: Model of the sliding mirror mechanism for the on/off calibration of the 3 mm and 4 mm receiver [34].

The flat reflectors in this part of the optical train have no optical power, but redirect the beam in a particular direction, and result in an additional propagation distance and possible aberrations which must be accounted for.

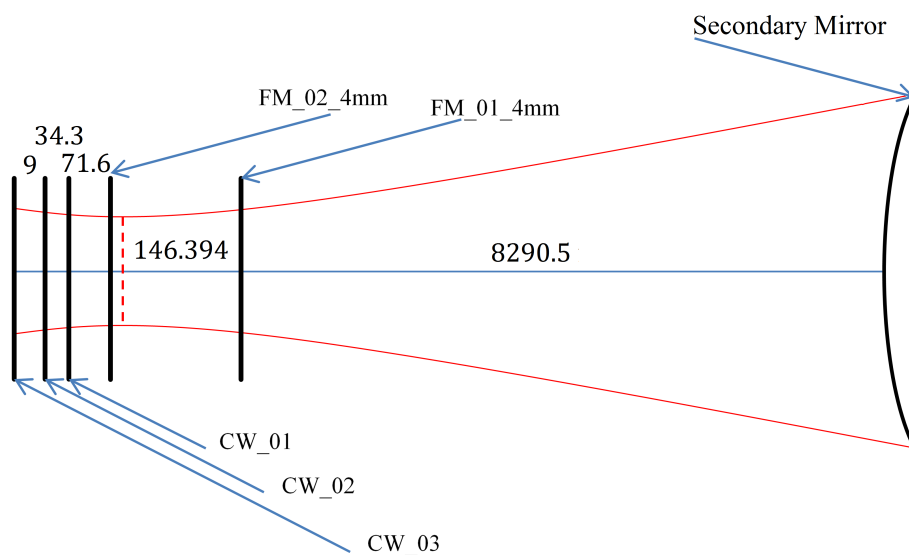


Figure 3.7: Simplified schematic showing position of mirrors in the steering mechanism and cryostat windows [34]. Dimensions in millimetres.

Figure 3.7 shows the existing position of the mirrors and cryostat windows as designed for the 3 mm receiver. The dimensions are simplified to appear in one line

and displayed with the beam width at 67 GHz. The two flat mirrors are part of the sliding mirror mechanism. The first flat mirror after the secondary mirror is referred to as FM_01_4mm and the second as FM_02_4mm. FM_02_4mm is located 146.394 mm from FM_01_4mm. It is tilted at an angle of 45° , and it directs the incident radiation into the cryostat. The beam must fit through a series of cryostat windows. The first of these is denoted CW_01. It has a diameter of 91 mm and is located a distance of 71.6 mm from FM_02_4mm. The second cryostat window, CW_02, has a diameter of 92 mm and is located a distance of 34.3 mm from CW_01. CW_03 is the third cryostat window, and has a diameter of 95 mm and is located at a distance of 43.2 mm from CW_01.

The proposed optical scheme makes use of two off-axis ellipsoidal mirrors. The main alternative to this scheme was one with a dielectric lens and the horn antenna on-axis with the cryostat window. The disadvantage of the alternative scheme was the increased potential for standing wave effects due to the system being on-axis, and a significantly reduced amount of space for optical components. In order to achieve wavelength independence, a Gaussian beam telescope type configuration is required, which would be more difficult to achieve with the limited optical distance of an on-axis approach. Using two off-axis ellipsoidal mirrors allows greater freedom in the development of an appropriate solution as there is a higher number of variable parameters. Such a design is compact, and makes good use of the available space. In addition, a two ellipsoidal mirror design was also used for the 3 mm system. The pairing of off-axis reflectors helps achieve low cross-polar levels. The geometrical constraints affecting this particular design within the cryostat unit are shown in figure 3.8, along with the design itself.

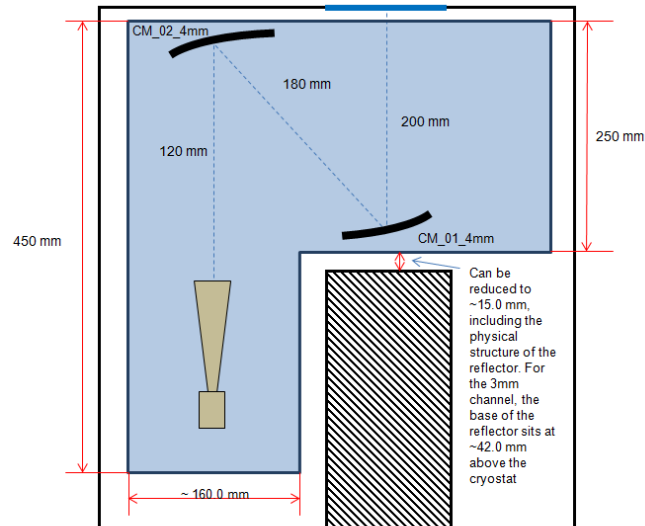


Figure 3.8: Proposed optical layout for the 4 mm system to fit within the geometrical constraints of the cryostat.

In this design, CM_01_4mm is an ellipsoidal mirror on an axis in line with the cryostat window, and CM_02_4mm is an ellipsoidal mirror on the axis in line with the horn. The horn aperture is imaged by CM_02_4mm to a focus between CM_02_4mm and CM_01_4mm, and this is then imaged to the secondary mirror.

3.2.2 Horn Design

The final corrugated horn, designed at Maynooth by Eimante Kalinauskaite, was designed to have a slant length of 100 mm, axial length of 87 mm, and an aperture radius of 15 mm. This is a standard linear corrugated horn dimension for this frequency range. The horn design is shown in figure 3.9, and includes corrugations which are perpendicular to the axis of propagation

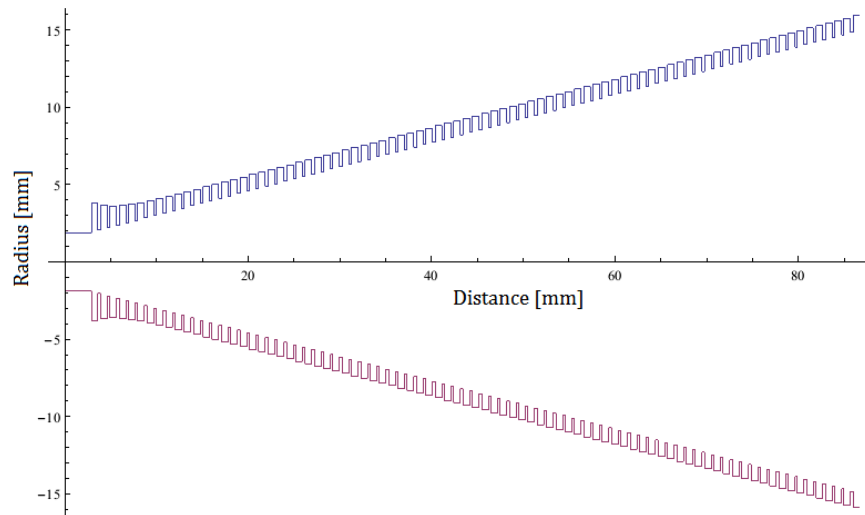


Figure 3.9: Final design of the conical corrugated horn.

The Cylindrical Scatter software program was used to obtain the scattering matrices, fields at the aperture, and the farfield beam patterns. The aperture field at 76 GHz is shown in figure 3.10; the blue line corresponds to a cut taken at $\varphi = 0^\circ$, the red at $\varphi = 90^\circ$, and the yellow at $\varphi = 45^\circ$. The horn has excellent cross polar performance with low levels, satisfying the design constraints.

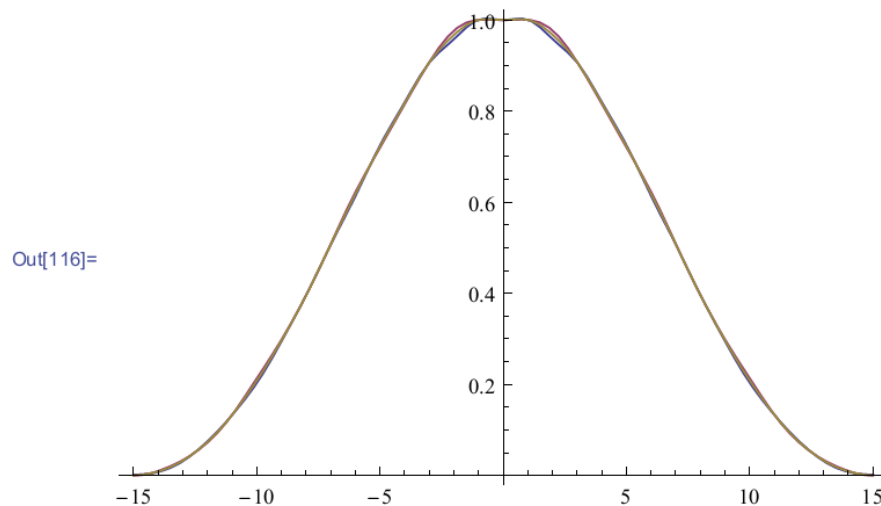


Figure 3.10: Aperture fields of the horn at 76 GHz taken at various cuts

In figure 3.11, the farfield co-polar and cross-polar radiation cuts are presented for the horn, at 76 GHz. The cross-polar cuts were taken at $\varphi = 45^\circ$.

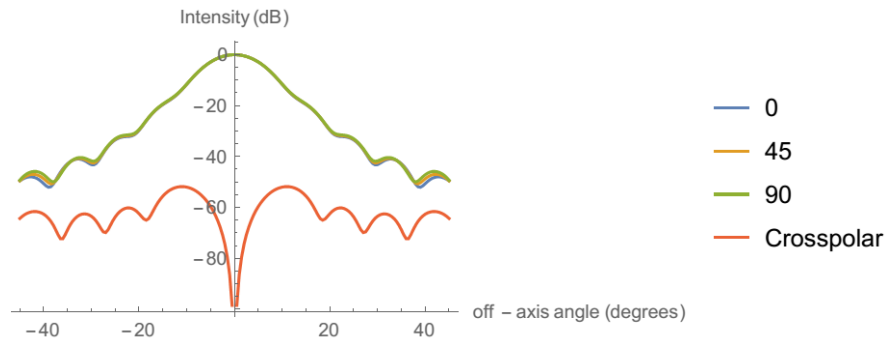


Figure 3.11: Horn farfield at 76 GHz, showing the required low cross polar levels.

The horn aperture fields used for the GRASP analysis presented in chapter 4 were generated using this model in Cylindrical Scatter. These consist of a tabulated grid of data points for the co and cross polar fields.

3.2.3 Further Design Considerations

Due to mechanical constraints, only certain optical designs were possible. As shown in figure 3.12, the 4 mm system was considered with three different separations between the horn and cryostat optical axes.

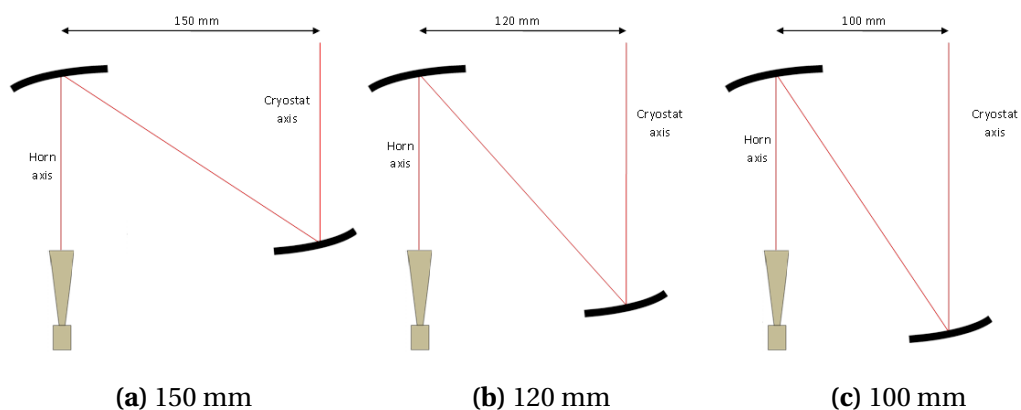


Figure 3.12: Three options for the separation between the horn and cryostat axes.

When considering the different separations between the horn and cryostat axes, the angle of reflection was changed in each case in such a way that the optical distance

between the mirrors remained 180 mm, so the same ABCD matrix setup could be used.

Ultimately, the 120 mm separation was chosen as a compromise. The 150 mm separation was close to the mechanical limit of the cryostat, and would result in the beams potentially being close to the cryostat wall. The physical overlap of the mirrors in the 100 mm case resulted in some of the beam being reflected back and lost. This advantage of the 120 mm separation over the 100 mm separation is illustrated in the GRASP simulation using rays in figure 3.13.

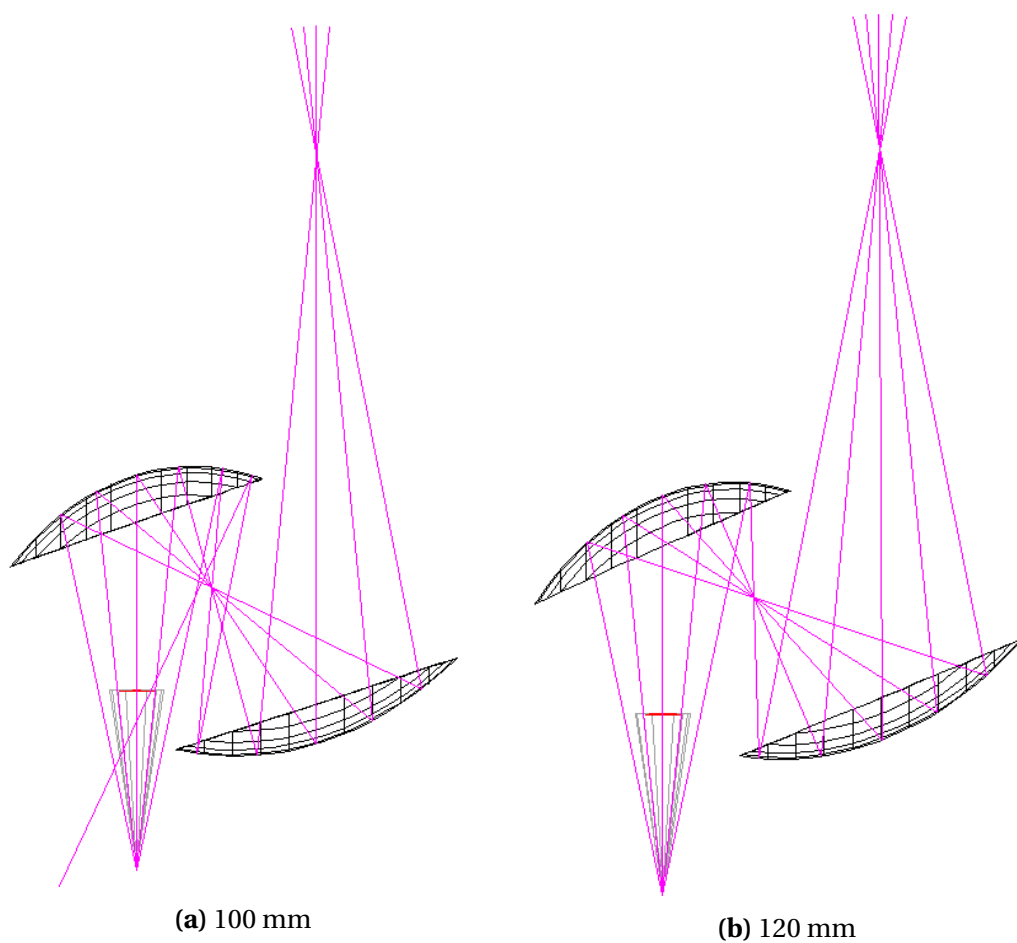


Figure 3.13: Comparison of 100mm separation with 120 mm separation, showing rays being reflected back in the 100mm case. The maximum angle for rays shown is 12°

The rays are set to a maximum angle of 12° . At the horn aperture, the geometrical beam associated with this angle approximately corresponds to 2.5 times the beam radius. The mirrors have the same radii in each case: the first mirror after the horn

antenna (denoted CM_02) has a radius of 70 mm; the second mirror (CM_01) has a radius of 78 mm. These radii were chosen so that they would correspond to 2.5 times the beam radii at the mirror positions. Using the 100 mm separation would introduce an unnecessary truncation which should be avoided.

3.3 Initial Optical Analysis

The ABCD matrix technique (Section 2.3) was used for the initial analysis of the system.

The two ABCD matrices required for this system were those for propagation in free space and for a thin lens. The matrix for propagation in free space is

$$M_{\text{dist}} = \begin{pmatrix} 1 & d \\ 0 & 1 \end{pmatrix}, \quad (3.1)$$

where d is the distance travelled by the beam. The matrix for a thin lens is

$$M_{\text{lens}} = \begin{pmatrix} 1 & 0 \\ -\frac{1}{f} & 1 \end{pmatrix}, \quad (3.2)$$

where f is the focal length. The focal lengths found here were later used to determine properties of the ellipsoidal mirrors used in the system.

The combined matrix for the system is

$$M = \begin{pmatrix} 1 & d_3 \\ 0 & 1 \end{pmatrix} \begin{pmatrix} 1 & 0 \\ -\frac{1}{f_2} & 1 \end{pmatrix} \begin{pmatrix} 1 & d_2 \\ 0 & 1 \end{pmatrix} \begin{pmatrix} 1 & 0 \\ -\frac{1}{f_1} & 1 \end{pmatrix} \begin{pmatrix} 1 & d_1 \\ 0 & 1 \end{pmatrix}. \quad (3.3)$$

This was then used to determine the evolution of the optical beam at important planes in the system.

In order to cover the band width of the channel, analysis was performed for three

frequencies: 67 GHz, 76.5 GHz, and 86 GHz. The focal lengths were chosen so that the beam radius at the secondary mirror would be equal at all three frequencies, i.e. the system would be wavelength independent. This was done by varying the two focal lengths of the ellipsoidal mirrors in order to achieve the same beam width and radius of curvature for the three frequencies across the band. Appropriate focal lengths of 56.07 mm for CM_02 and 79.355 mm for CM_01 were calculated to achieve this. They also give waists reasonable distances between mirrors.

The beam waist forms a distance Δ behind the aperture, defined by

$$\Delta = \sqrt{\frac{w^2}{1 + \left(\frac{\pi w^2}{\lambda R}\right)^2}}. \quad (3.4)$$

The following table gives the values of Δ , the distance of the waist from CM_01, and the beam width at the waist for the three frequencies.

Frequency (GHz)	Δ (mm)	waist distance from CM_01 (mm)	w at waist(mm)
67	29.97	308.67	15.68
76.5	35.81	312.97	13.75
86	41.35	315.94	12.24

Table 3.4: Δ , beam waist location and radius for the large horn

The following tables outline the information on the beam width, radius of curvature, and edge taper at all planes of interest in the system. While there is some variation of the beam width at the secondary mirror in table 3.5, this is acceptable as the difference (2.4 mm) is smaller than the smallest wavelength for which the system is designed (3.5 mm), and does not significantly affect the optical coupling. Moreover, even a small variation of one of the focal lengths has an impact on the beam width at the secondary mirror comparable to this difference.

Parameter	67 GHz	76.5 GHz	86 GHz
w_0 at phase centre (mm)	8.08	7.73	7.39
Δ (mm)	29.97	35.51	41.35
w at aperture (mm)	9.65	9.65	9.65
w at CM_02 (mm)	27.6	26.3	25.3
w at CM_01 (mm)	32.1	31.5	31.1
w at CW_03 (mm)	18.5	17.1	16.1
w at CW_02 (mm)	18.1	16.7	15.6
w at CW_01 (mm)	16.8	15.1	13.9
w at FM_02(mm)	15.7	13.8	12.2
w at FM_01(mm)	20.9	19.2	18.0
w at secondary (mm)	767.1	765.7	764.7

Table 3.5: Evolution of beam width through the system.

Parameter	67 GHz	76.5 GHz	86 GHz
R at aperture (mm)	100	100	100
R at CM_02 (mm)	164.0	170.6	176.4
R after CM_02 (mm)	-85.2	-83.5	-82.2
R at CM_01 (mm)	98.7	99.9	100.8
R after CM_01 (mm)	-405.2	-386.4	-373.7
R at CW_03 (mm)	-382.7	-316.3	-273.2
R at CW_02 (mm)	-398.5	-324.9	-277.5
R at CW_01 (mm)	-521.1	-399.3	-323.8
R at FM_02 (mm)	4783.3	11895.3	-17540.4
R at FM_01 (mm)	347.8	303.2	270.9
R at secondary (mm)	8446.7	8441.6	8438.0

Table 3.6: Evolution of radius of curvature through the system.

Parameter	67 GHz	76.5 GHz	86 GHz
T_e at CW_03 (dB)	-57.2	-67.0	-75.6
T_e at CW_02 (dB)	-56.1	-65.9	-75.5
T_e at CW_01 (dB)	-63.7	-78.9	-93.1
T_e at FM_02 (dB)	-106.6	-138.0	-176.5
T_e at FM_01 (dB)	-60.2	-71.3	-81.1
T_e at secondary (dB)	-12.0	-12.0	-12.0

Table 3.7: Evolution of edge taper through the system.

3.4 Truncation Analysis

As each optical element (mirror or window) in the system has a finite radius, it is important to know the effects that this will have on the beam. Here, the ellipsoidal mirrors are modelled as being thin lenses with radii 2.5 times the local beam radius. This is equivalent to an edge taper of -54.3 dB. The other mirrors and the cryostat windows are modelled using the dimensions given in section 3.2.1. It is important to measure the effect of truncation, and keep it to a minimum. If the beam is significantly truncated, unforeseen diffraction effects will occur, which affect its subsequent behaviour [45].

As outlined in chapter 2, the electric field is described by a combination of Gaussian beam modes

$$E = \sum_n A_n \Psi_n, \quad (3.5)$$

where Ψ represents the complex independent propagating modes. Truncation is introduced by considering the output electric field E_o to be zero where the off axis distance r is larger than the aperture radius a , such that

$$\begin{aligned} E_o(r) &= E_i(r) & r &\leq a \\ E_o(r) &= 0 & r &\geq a, \end{aligned} \quad (3.6)$$

where E_i is the input electric field [46]. The incident and output fields may both be written in terms of Gauss-Laguerre modes

$$\begin{aligned} E_i &= \sum_n A_n \Psi_n(r), \\ E_o &= \sum_m B_m \Psi_m(r), \end{aligned} \quad (3.7)$$

where the input mode coefficients A_n are different from the output mode coefficients B_m . The output coefficients are given by the overlap integral

$$B_m = \int_0^a \Psi_m(r) E_o(r) 2\pi r dr. \quad (3.8)$$

Within the aperture is the special case where the output field and the input field are equivalent, so

$$\begin{aligned} B_m &= \int_0^a \Psi_m(r) E_i(r) 2\pi r dr \\ &= \sum_n A_n \int_0^a \Psi_m^*(r) \Psi_n(r) 2\pi r dr, \end{aligned} \quad (3.9)$$

which defines

$$S_{mn} = \int_0^a \Psi_m^*(r) \Psi_n(r) 2\pi r dr, \quad (3.10)$$

where S_{mn} is a scattering matrix which relates the output coefficients to the input coefficients

$$B_m = \sum_n S_{mn} A_n. \quad (3.11)$$

In the trivial case where truncation effects are not considered, the scattering matrix simplifies to the identity matrix. The scattering matrix is described in terms of Gauss-Laguerre modes by

$$S_{mn} = \int_0^a \sqrt{\frac{2}{\pi w^2}} L_m\left(\frac{2r^2}{w^2}\right) L_n\left(\frac{2r^2}{w^2}\right) \exp\left(-\frac{2r^2}{w^2}\right) 2\pi r dr. \quad (3.12)$$

The beams are presented in the following graphs at the important planes of the system for three frequencies across the band (67 GHz, 76.5 GHz, 86 GHz). The result

of the truncated beam is presented in the graphs below in red, and the untruncated beam in blue. These graphs illustrate the effect truncation has on the beam.

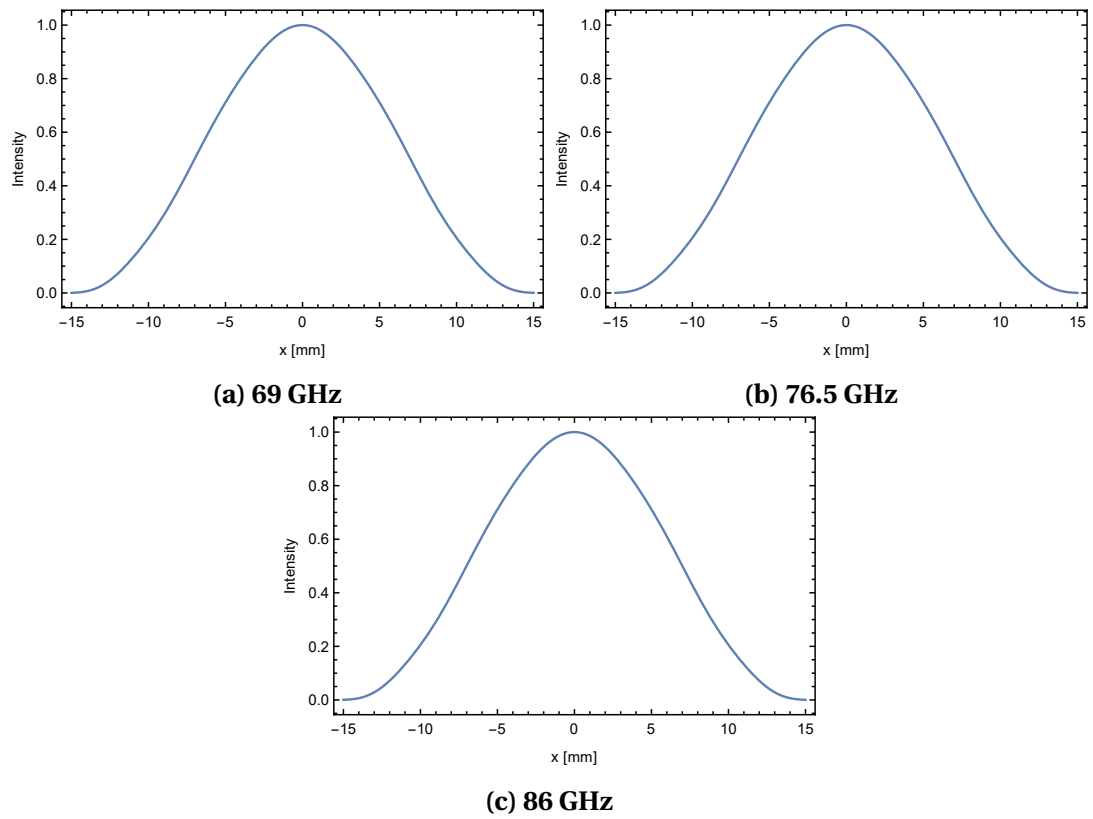


Figure 3.14: Beam at aperture

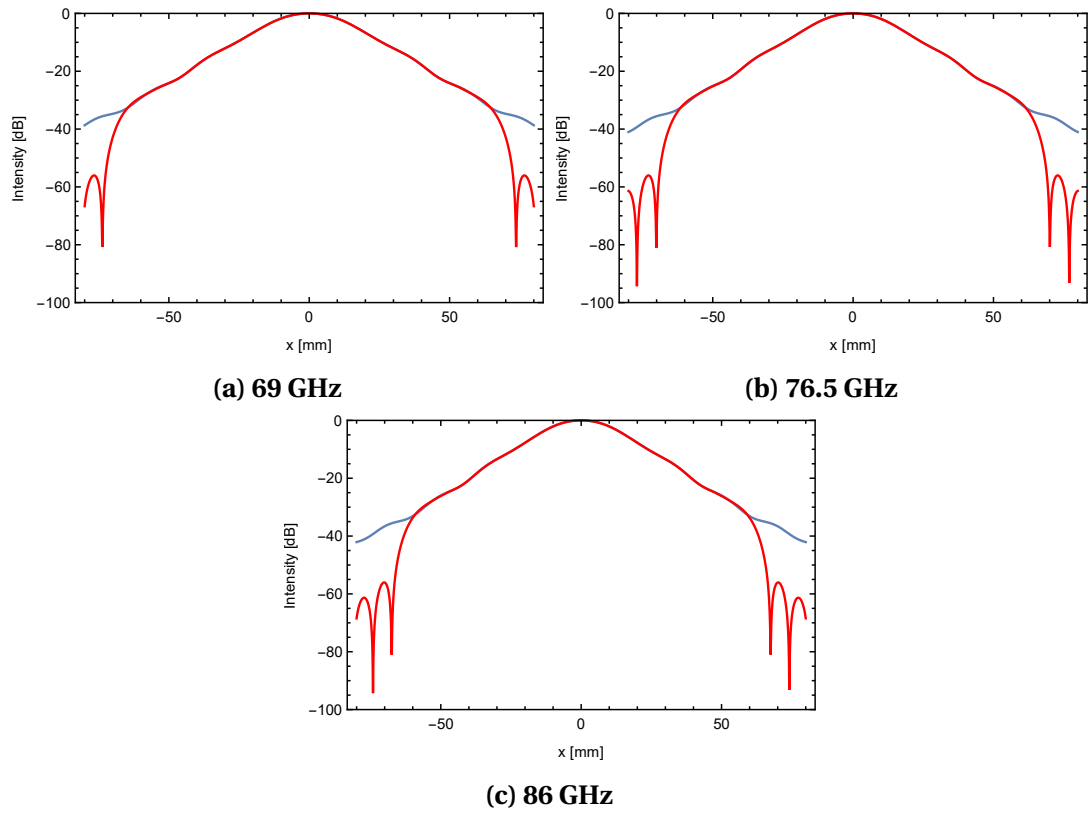


Figure 3.15: Beam at Mirror 1

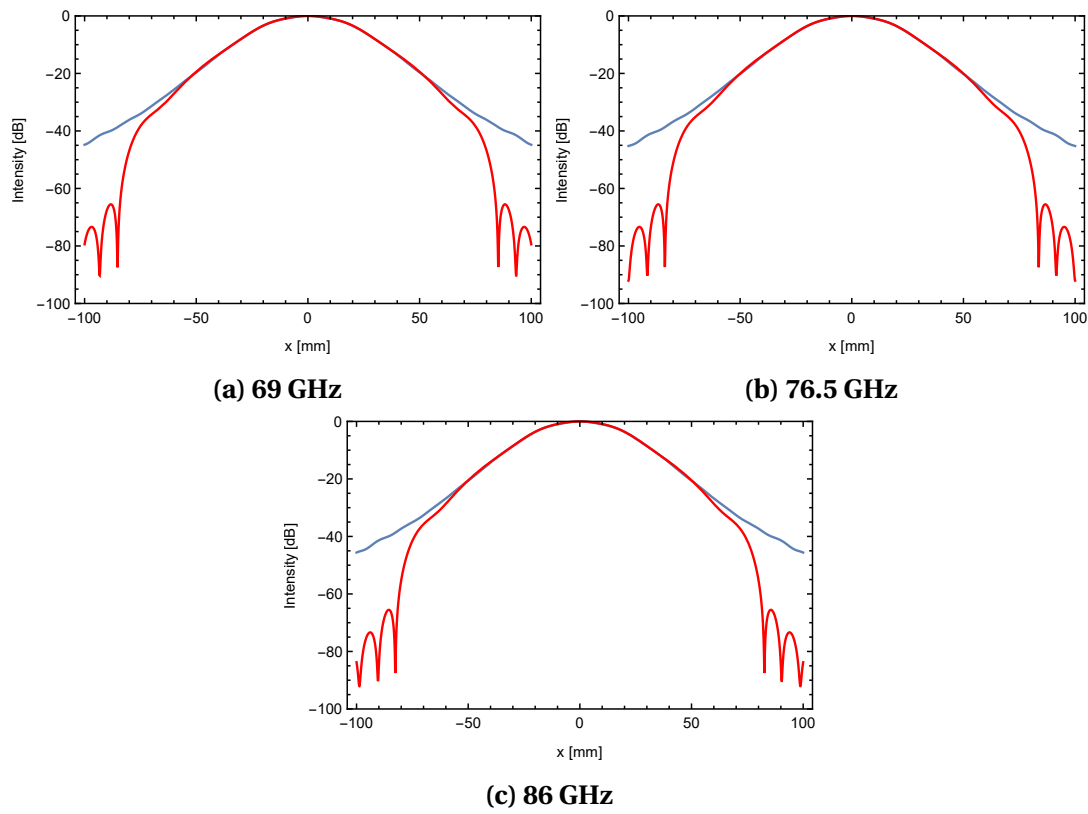


Figure 3.16: Beam at Mirror 2

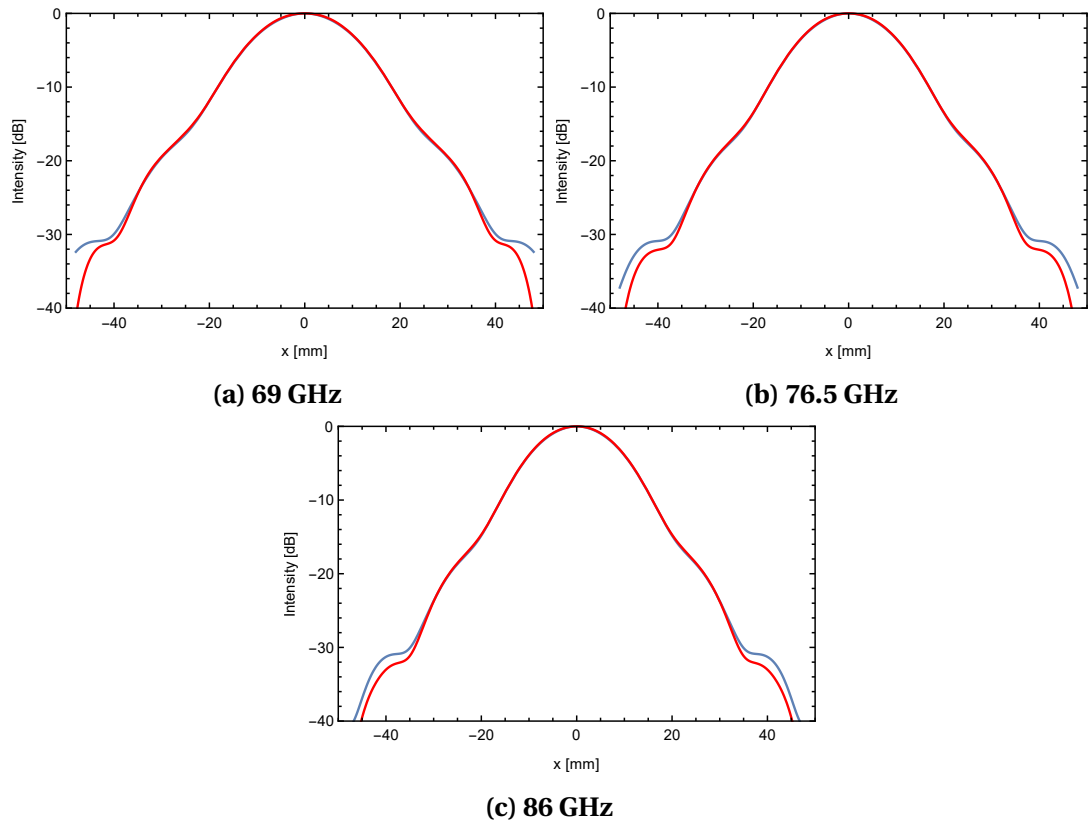


Figure 3.17: Beam at Cryostat Window 3

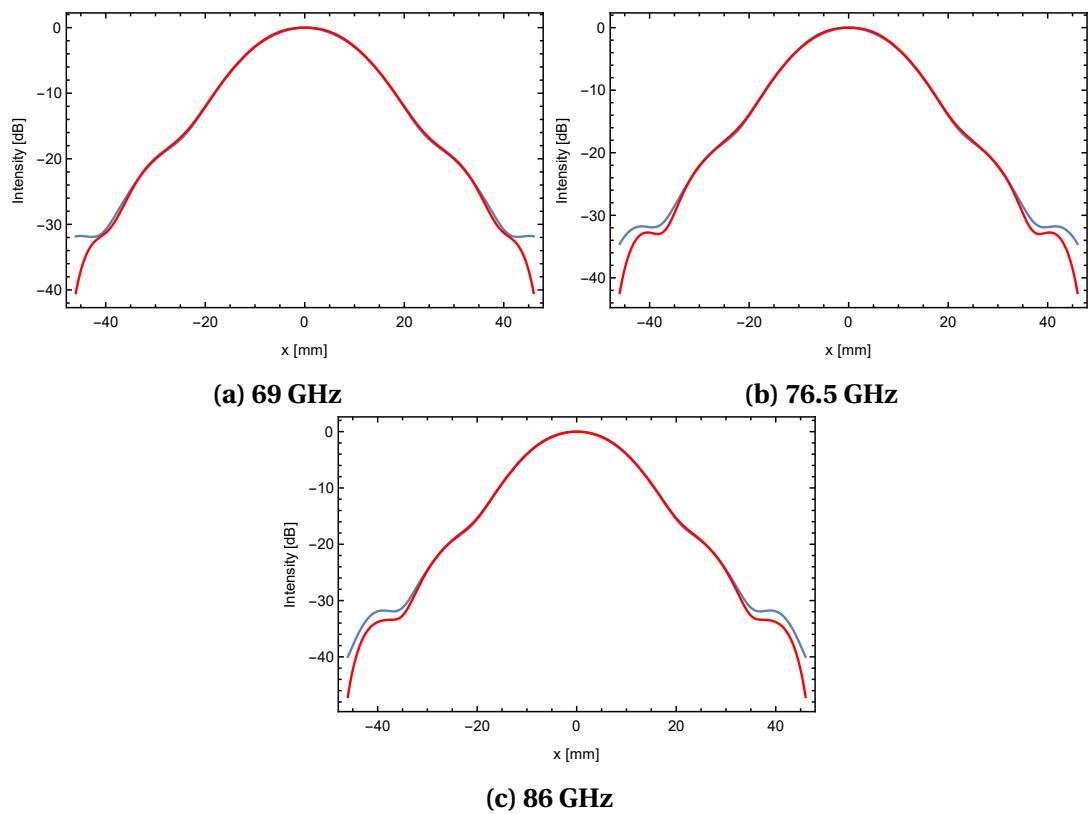


Figure 3.18: Beam at Cryostat Window 2

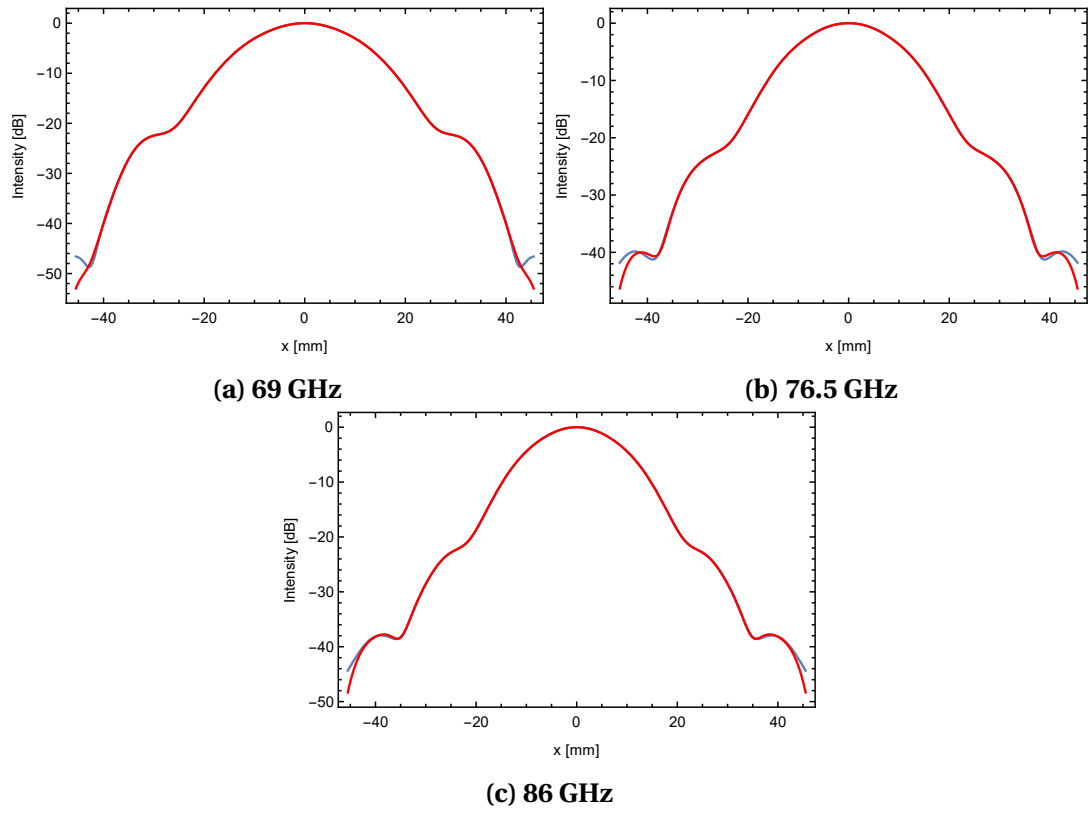


Figure 3.19: Beam at Cryostat Window 1

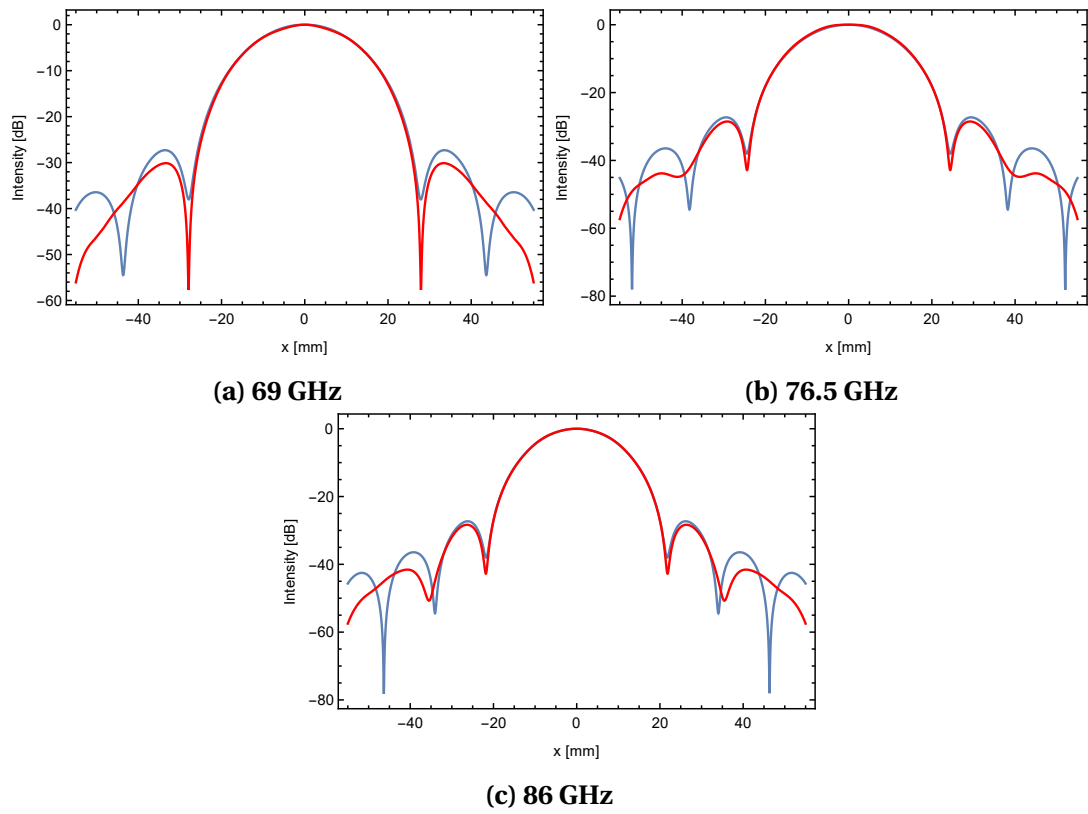


Figure 3.20: Beam at Flat Mirror 2

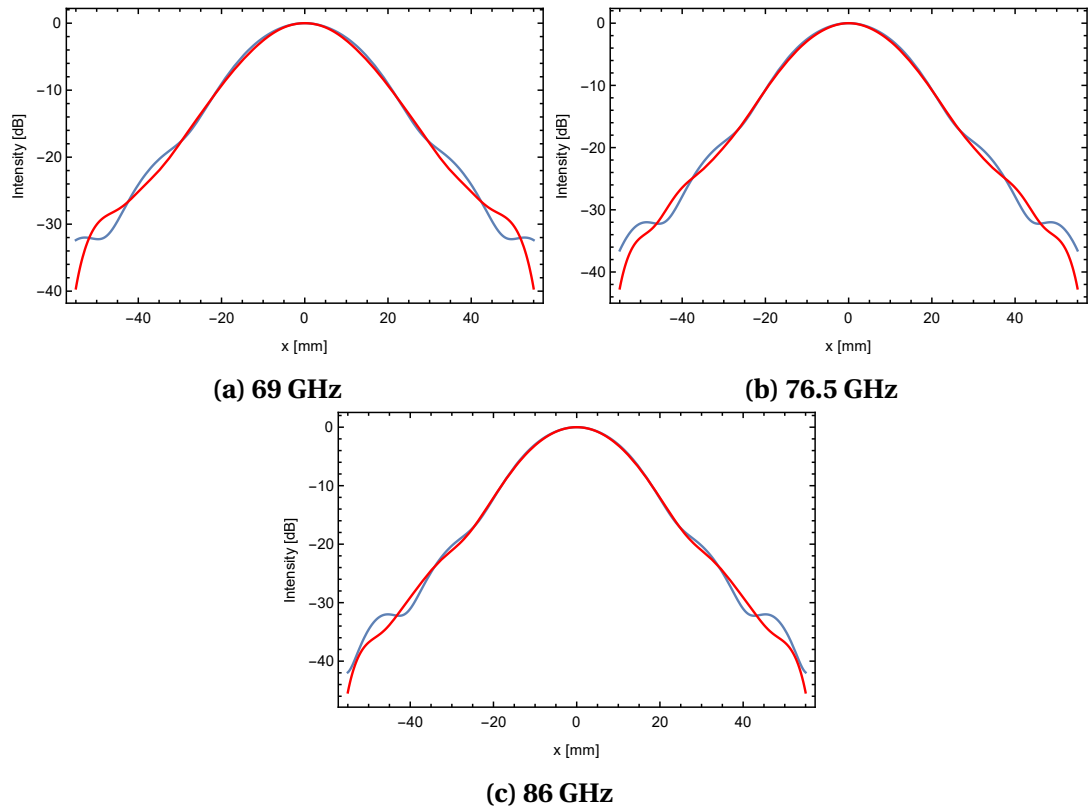


Figure 3.21: Beam at Flat Mirror 1

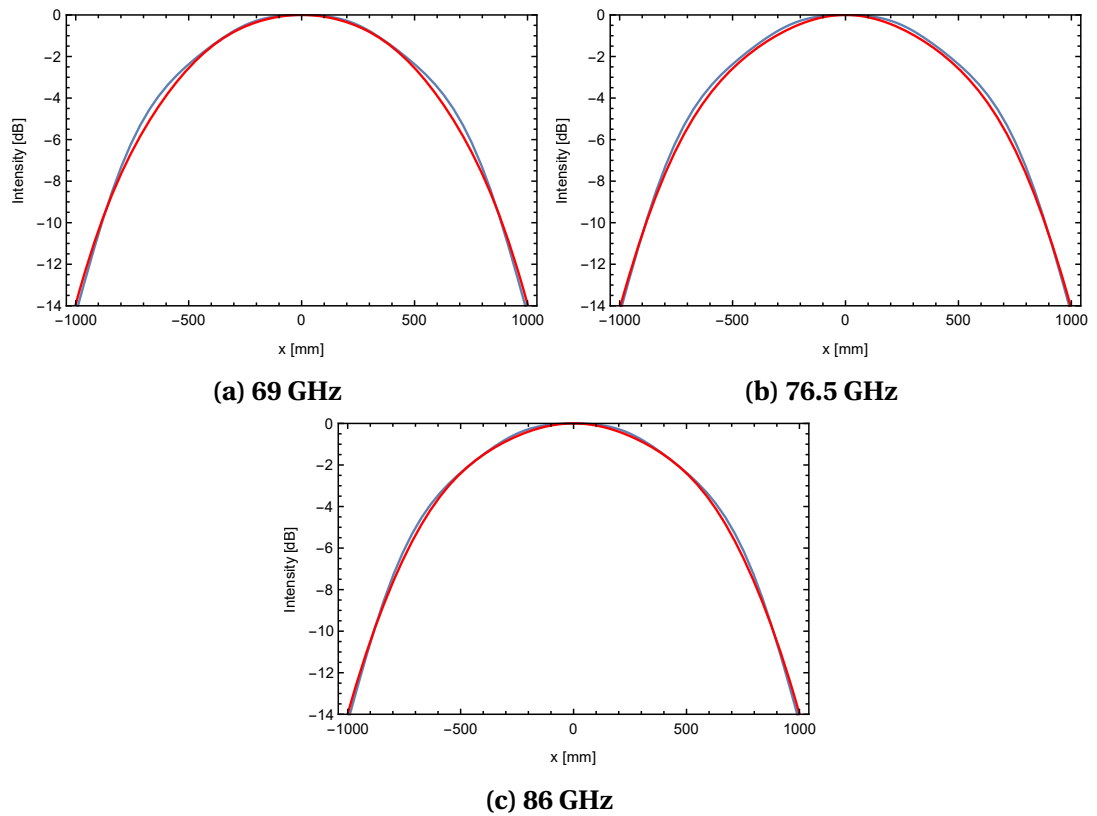


Figure 3.22: Beam at Secondary Mirror

The truncated power levels and power lost are presented in table 3.8. These power levels were calculated at 67 GHz as this frequency has the largest wavelength. The larger wavelength results in a larger beam width, which means that more power will be lost due to truncation effects. The results are cumulative, so that the input power at each element accounts for power lost at previous elements. Note that the initial power at the horn aperture is not exactly equal to unity due to the finite number (20) of modes used in the calculation.

Plane	Truncated Power level	Normalized Power Lost
Horn Aperture	0.999813	0
CM_02	0.997302	0.002511
CM_01	0.997028	0.000274
CW_03	0.996043	0.000985
CW_02	0.995761	0.000282
CW_01	0.995617	0.000144
FM_02	0.995594	0.000023
FM_01	0.993781	0.001813

Table 3.8: Power loss due to truncation at important planes at 67 GHz.

Table 3.8 indicates the optical design ensures insignificant levels of truncation along the optical train in the proposed 4 mm design.

3.5 Optical Efficiency

The optical efficiency is the coupling of the predicted beam from the detector horn propagated to the secondary mirror with the beam from the sky at the secondary mirror. To achieve this, the predicted beam at the secondary mirror is coupled with a truncated planar field, also known as a top-hat field because of its shape. This represents a plane wave arriving at the telescope from a point source at infinity,

assuming the field from the sky is a plane wave. The hole in the centre of the top-hat field is due to the design of the Cassegrain telescope (figure 3.4), which shadows some of the incoming radiation due to the shadow of the secondary mirror on the primary mirror. The amplitude patterns are shown in figure 3.23. The top-hat field has the same radius as the secondary mirror, and the coupling is carried out in the same plane. The optical efficiency calculations are performed using equation 2.84. This model also assumes ideal performance of the telescope. This does not account for aberrations caused by the receiver optics, as the mirrors are modelled as thin lenses. These aberrations are accounted for by propagating the beam using physical optics in chapter 4.

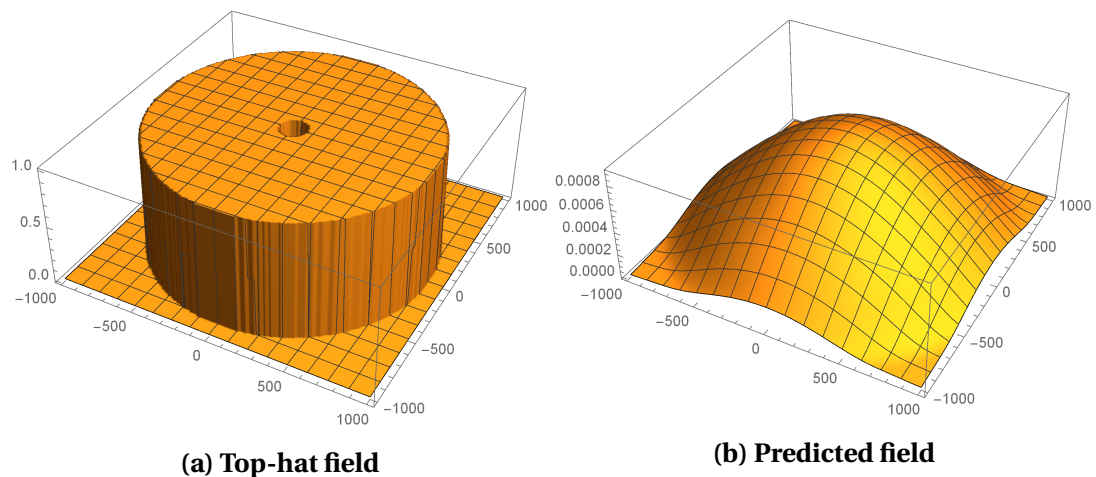


Figure 3.23: Amplitude patterns of the truncated plane wave (top-hat field) and the predicted field at the secondary mirror for the calculation of aperture efficiency. x and y dimensions are in mm.

The initial optical efficiency calculations were based solely on the two elliptical mirrors, with further analysis including the full optics with and without the cryostat windows. The initial beam to represent the horn is based on the Bessel function (section 2.4.2). The results are shown in table 3.9.

Frequency	67 GHz	76.5 GHz	86 GHz	67 GHz	76.5 GHz	86 GHz
Efficiency	Untruncated			Truncated		
Just mirrors	86.0%	86.0%	86.0%	84.6%	84.6%	84.6%
No window	85.2%	85.2%	85.2%	83.9%	84.4%	84.4%
windows	85.2%	85.2%	85.2%	83.9%	84.4%	84.4%

Table 3.9: Comparison of beam efficiency for both the untruncated and truncated beams for different cases. The maximum achievable for an untruncated beam would be 86%.

As expected, the best efficiency of 86% is calculated for the untruncated beam, which is good coupling with the sky. This is only slightly reduced when truncation is introduced. The inclusion of the full optics reduces the efficiency further, although not by a significant amount. The cryostat windows appear to have a negligible effect on the beam efficiency, which would indicate that the vast majority of the beam passes through them unhindered as expected from table 3.8.

3.6 Conclusion

In this chapter, Onsala Space Observatory was introduced, specifically the 20 m telescope optics associated with the 4 mm receiver. The background to the 4 mm receiver was outlined, including design requirements and the horn design. The initial optical analysis of the system was presented, making use of ray transfer matrix analysis. Truncation analysis and optical efficiency calculations were performed, demonstrating that the proposed design meets requirements.

Chapter 4

PO Analysis of the 4 mm Receiver

Contents

4.1 GRASP Analysis	71
4.1.1 Gaussian beam	72
4.1.2 GRASP Hybrid Horn	74
4.1.3 Horn Aperture Grid Files	77
4.2 Propagation of the beam to the Sky	79
4.3 Cross polar levels	81
4.4 Comparison with the 3mm system	82
4.5 Experimental Measurements	83
4.6 Conclusion	89

The previous chapter described the initial design and analysis 4 mm receiver using Gaussian beam mode analysis and the ABCD matrix technique. Here, an outline of the analysis of the design is presented, after it was implemented in GRASP.

4.1 GRASP Analysis

The system was implemented in GRASP, using the methods described in chapter 2. A plot of the final GRASP design is illustrated in figure 4.1. Calculations were performed on the system using the sources outlined in that chapter: i.e., the Gaussian source, which is a simplified model of the horn aperture field; the more accurate hybrid mode conical horn, which is an a source built into GRASP; and the external

grid files, which were generated using *Scatter*, as outlined in the previous chapter. In addition to this, there were two variations of the external grid files used. The first variation was just of the horn, and the second included the transition from a rectangular waveguide to the conical horn, in order to have a more realistic simulation.

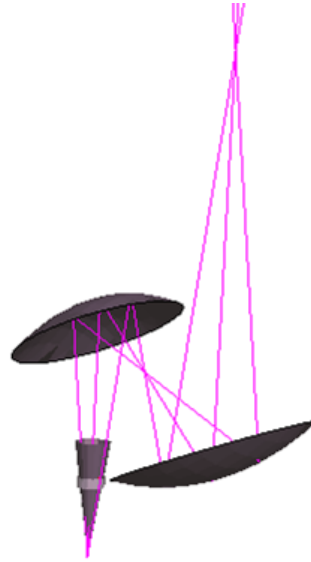
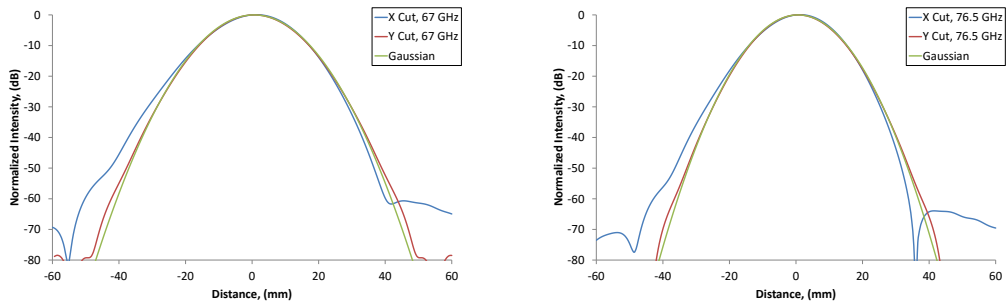


Figure 4.1: Final design of the 4 mm system in GRASP.

4.1.1 Gaussian beam

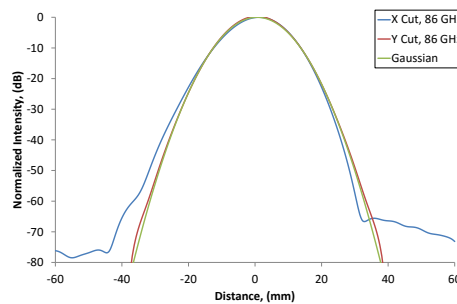
Using a Gaussian beam source (section 2.5.3) as a simplified representative beam for the large horn, figure 4.2 gives the Gaussian beam cuts at the focal planes for various frequencies across the band. The focal planes here refer to the positions at which the beam waists form following the second mirror after the horn (CM_01). The focal plane position varies with frequency. As mentioned in the previous chapter, the focal plane positions, in terms of distance from the CM_01, are 308.67 mm, 312.99 mm, and 315.94 mm for 67 GHz, 76.5 GHz, and 86 GHz respectively. The beam representing the horn has $w = 0.6435a = 9.6525$ mm and $R = 100$ mm at the aperture position, 120 mm from the CM_02. The x and y cuts are graphed against the expected Gaussian beam which is based on the waist radius calculated previously using the ABCD matrices. The beams correspond well with the approximate beam, with a reasonable symmetry. There is greater divergence from the Gaussian

beam in the x cut because this is the plane in which the mirror reflection occurs, causing off-axis aberration.



(a) 67 GHz, $w = 15.6784$ mm

(b) 76.5 GHz, $w = 13.7499$ mm



(c) 86 GHz, $w = 12.2423$ mm

Figure 4.2: Cuts of the Gaussian beam at the focal planes.

The Gaussian beams cuts at the secondary mirror (8751.8 mm from CM_01) are shown in figure 4.4. Again, there is less distortion in the y cut because the beam is only transformed in the xz plane. Here, the beams for the three frequencies are plotted on the same graph to show that the beam size is wavelength independent. There is good agreement with the approximate Gaussian with a beam radius of 765.7 mm.

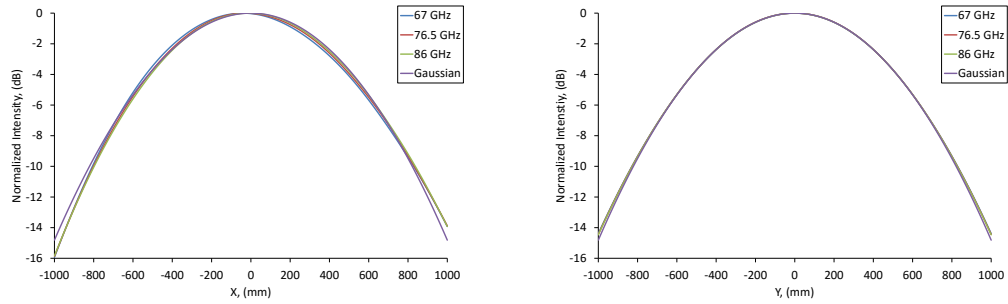


Figure 4.3: Cuts of the Gaussian beam at the Secondary Mirror, $w = 765.7$ mm

From this, it can be concluded that the system images the horn aperture on to the secondary mirror of the telescope in a wavelength independent manner, as designed. This means there is wavelength independent coupling over the band.

4.1.2 GRASP Hybrid Horn

For a more accurate model, the GRASP hybrid horn (section 2.5.3) was then used as a source. This is a scalar approximation to a corrugated horn operating in the balanced hybrid mode condition, which does not include cross-polar components, but gives a better indication of the sidelobes associated with the horn fields. The horn aperture has a diameter of 15 mm, and the slant length is 100 mm. The cuts are graphed against a truncated Bessel field, representing the beams calculated using the ABCD matrices (section 2.4.2), which is a better match to the expected aperture field than the Gaussian field distribution.

The fields in the aperture of the horn using the hybrid mode model of the horn and an equivalent Gaussian field as a first approximation are illustrated in figure 4.4. This shows that the fields have different profiles, which leads to the different fields in the telescope focal plane.

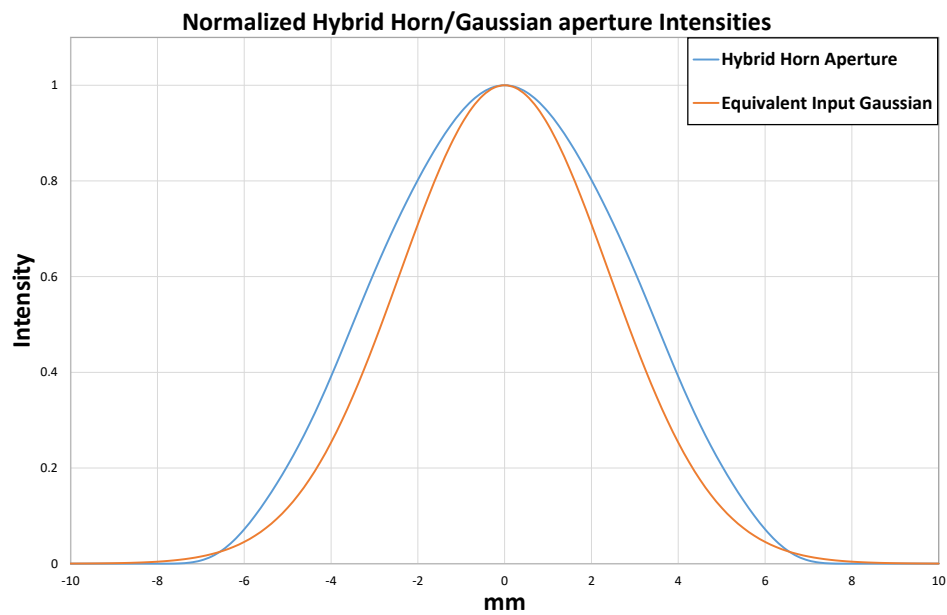


Figure 4.4: Comparison of the aperture fields of the hybrid mode model and equivalent Gaussian.

Figure 4.5 shows the cuts at the beam waist locations when the GRASP hybrid horn is used as a source. As in the previous section, the cuts are taken at the focal planes, where the minimum beam widths occur. The focal plane positions remain the same as previously.

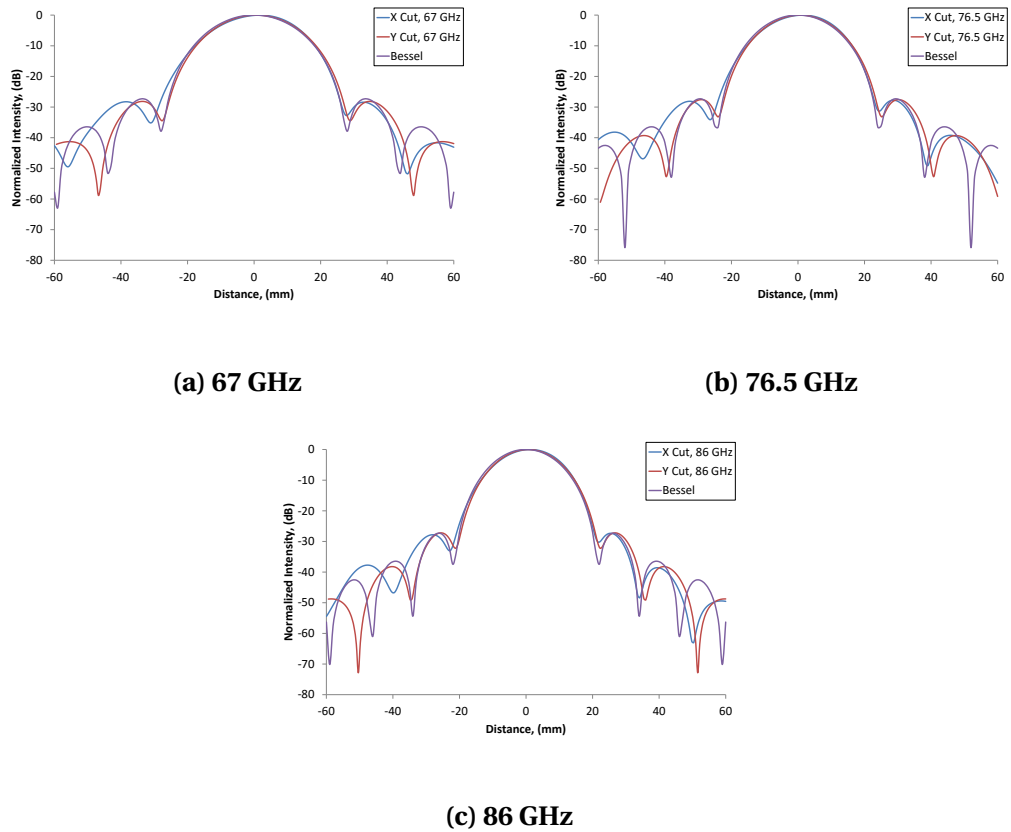


Figure 4.5: Cuts of the GRASP Hybrid Horn beam at the focal planes, plotted with equivalent truncated Bessel field.

Figure 4.6 shows the cuts taken at the position of the secondary mirror for the Hybrid mode horn. There is good agreement with the expected truncated Bessel field from the ABCD technique, especially in the y cut. There is an aberration present in the x cut in the beams propagated through the 4 mm receiver. This is caused by the transformation of the beams by the ellipsoidal mirrors in the xz plane. This will be discussed later in section 4.2, where the effect will be accounted for.

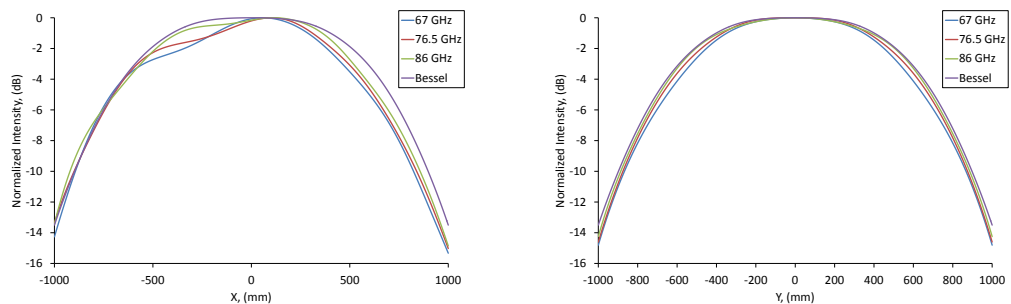


Figure 4.6: Cuts of the Hybrid Mode Horn at the Secondary Mirror

4.1.3 Horn Aperture Grid Files

Figures 4.7 and 4.9 give the cuts taken at the same beam waist location using the aperture grid files calculated with modematching code as a tabulated planar source (section 2.5.3), for both the horn without and with a transition.

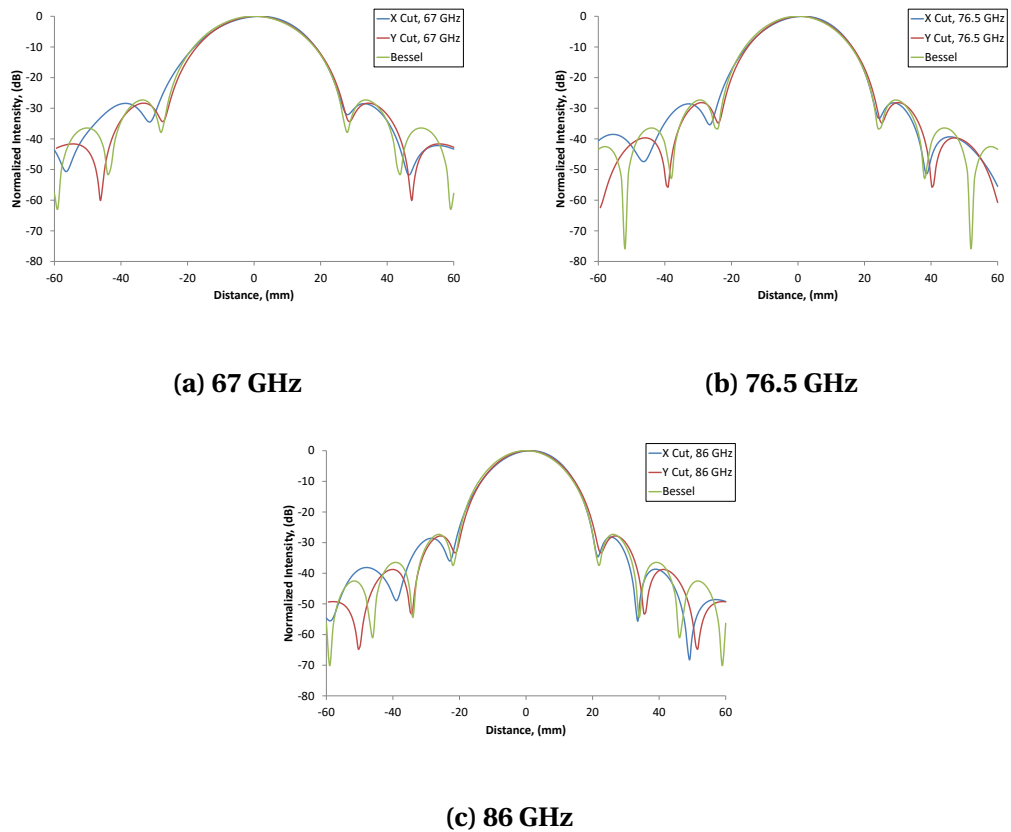


Figure 4.7: Cuts at the focal planes for the real horn grid files (with no transition), plotted with equivalent Bessel field.

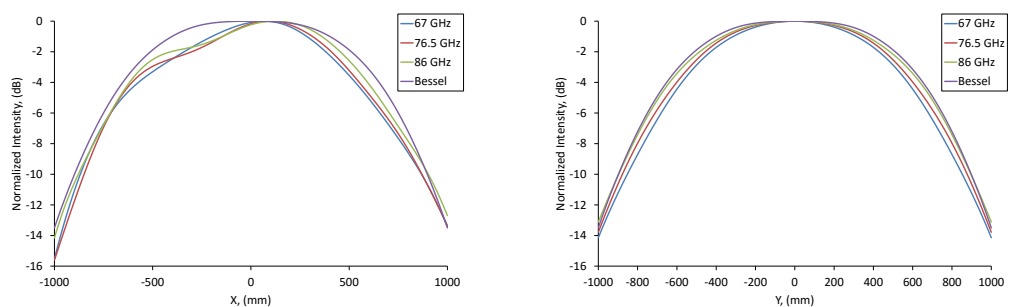


Figure 4.8: Cuts at the Secondary Mirror for the tabulated data (with no transition), plotted with equivalent Bessel field.

It is clear from figure 4.8 that when the tabulated grids from modematching are analysed with the corrugated horn, the field is not fully wavelength independent and has some variation with wavelength over the band. This suggests including an accurate aperture grid to represent the horn is important rather than just using the approximate hybrid mode representation of the horn.

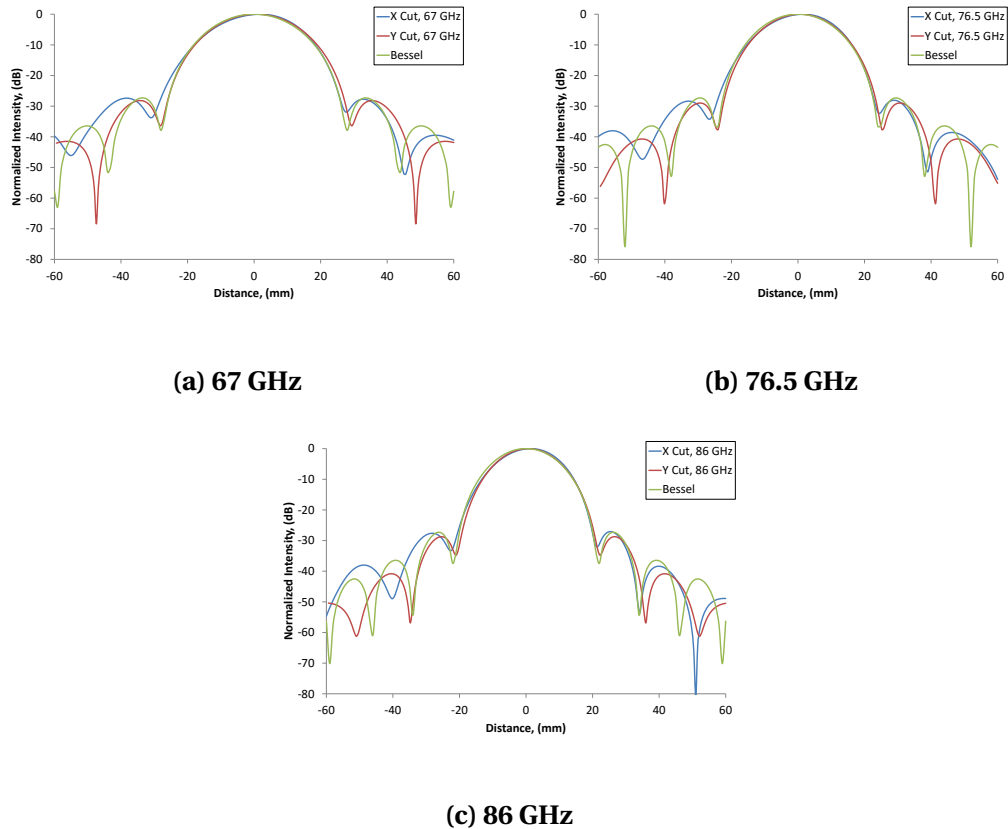


Figure 4.9: Cuts at the focal planes for the real horn grid files (with transition)

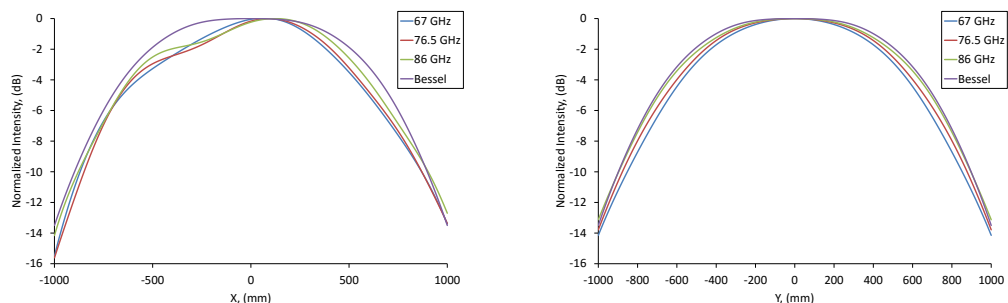


Figure 4.10: Cuts at the Secondary Mirror for the tabulated data (with transition), plotted with equivalent Bessel field.

The following contour plots in figures 4.11 and 4.12 were generated at the secondary mirror for the large horn with and without the horn transition to the waveguide present. The aberrations noticed in figures 4.8 and 4.10 are better represented here, showing that a clear on-axis aberration is present over the band.

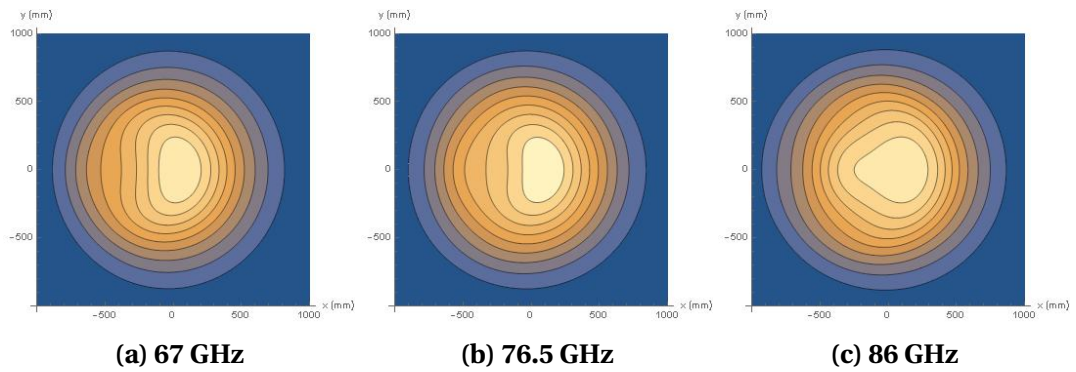


Figure 4.11: Contour plots at secondary (no horn transition)

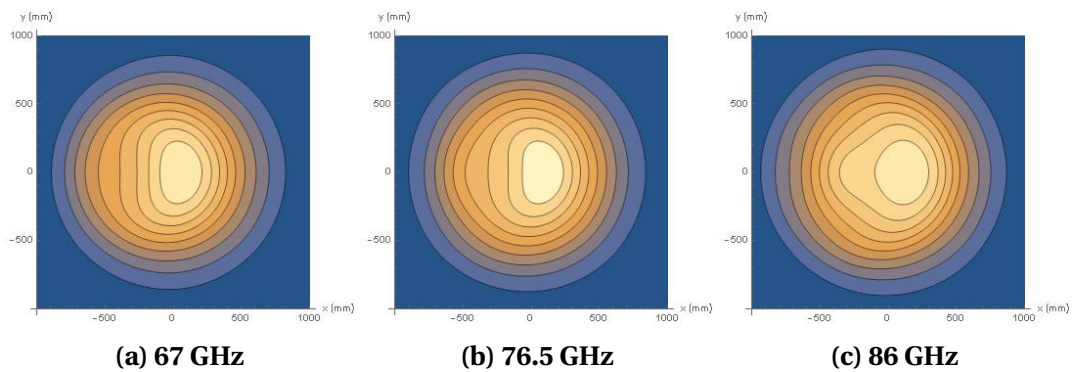


Figure 4.12: Contour plots at secondary (with horn transition)

The same aberrations are present in figures 4.11 and 4.12. This indicates that plotting a 2D grid with or without the horn transition has a negligible effect.

4.2 Propagation of the beam to the Sky

While the beams plotted above in figures 4.11 and 4.12 at the secondary mirror have asymmetries, the primary interest to astronomers is the symmetry of the beam on the sky. In order to ensure that the beam is symmetric on the sky, the 20 m Cassegrain telescope was modelled in GRASP with the 4 mm receiver. This model

includes both the primary and secondary mirrors, the dimensions of which were derived from figure 3.4 in the previous chapter. Because this is a large simulation, the GRASP hybrid horn as a source to reduce simulation time. The beam was propagated through the front end optics and the 20 m telescope, and the farfield pattern was collected from the primary mirror, i.e., the farfield beam on the sky from the Onsala 20 m telescope with the 4 mm receiver. This GRASP setup is illustrated in figure 4.13. The 4 mm system is just visible in the hole at the centre of the primary reflector.

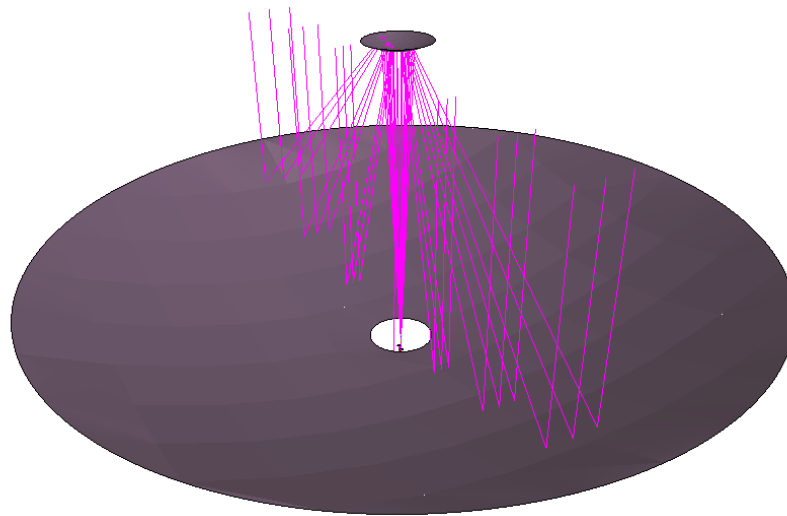


Figure 4.13: GRASP simulation including the secondary and primary mirrors.

The beam patterns are presented in figure 4.14. Note that the x and y coordinates are now in terms of angular degrees from the centre of the main beam. It is clear that the main beam is now symmetric, and the asymmetries are now in the sidelobes, indicating good practical optical performance.

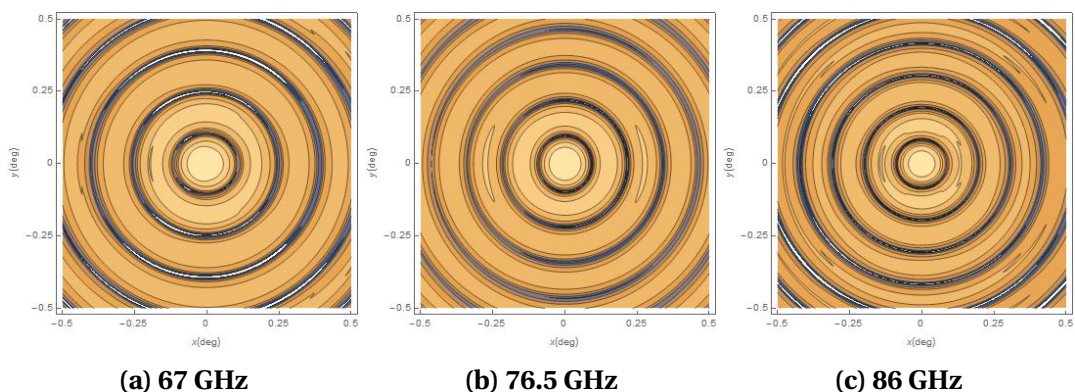


Figure 4.14: Farfield pattern of the beams on the sky.

Although the aberration still appears at the Fourier plane of the sky, it is dissipated to higher farfield angles, so it has little effect on the quality of the performance. This validates the proposed design.

4.3 Cross polar levels

The cross-polar levels associated with the feed horn and optics were calculated by integrating the total power in the cross-polar beam and normalizing it relative to the co-polar beam for all beams propagated from the feed. The cross-polar calculations were carried out at both the horn aperture and the secondary mirror to allow separate analysis of each. The cross polar level in decibels is given by the following equation:

$$XsP = 10 \log_{10} \left[\frac{\epsilon_{xsp}}{\epsilon_{cop}} \right] \quad (4.1)$$

where XsP is the cross-polar level (in dB), and ϵ_{xsp} and ϵ_{cop} are respectively the power levels of the cross and co polar distributions. The cross polar levels are presented below in tables 4.1 and 4.2 for the horns with and without the transition. Cross polar levels at the horn aperture and secondary mirror are given, along with the difference, ΔXsP , which is the level associated with the 4 mm optics in each case. The beam efficiencies are also presented; these were calculated using equation 2.84.

Frequency (GHz)	67	76.5	86
Beam Efficiency (%)	83.12	83.75	84.27
XsP horn (dB)	-38.06	-41.60	-38.94
XsP at secondary (dB)	-30.36	-31.99	-32.66
ΔXsP (dB)	-7.70	-9.61	-6.28

Table 4.1: Beam efficiency and cross-polarization for the grid files

Frequency (GHz)	67	76.5	86
Beam Efficiency (%)	83.11	83.75	84.72
XsP horn (dB)	-33.90	-36.64	-35.03
XsP at secondary (dB)	-29.84	-31.67	-32.59
Δ XsP (dB)	-4.06	-4.97	-2.44

Table 4.2: Beam efficiency and cross-polarization for the grid files with square to circular horn transition

The horn with the transition has higher cross-polar levels, as expected. The beam efficiency increases with frequency, also as expected, as the higher frequencies produce narrower beams. The beam efficiencies are slightly lower than those produced using the ABCD code in chapter 3. Table 4.3 presents the beam efficiency and cross polar levels for the beam produced using the Hybrid Mode conical horn within GRASP. Similar cross-polar levels at the secondary mirror are found with this method, although the beam efficiency is slightly reduced. Cross-polar levels at the horn are not included in this method.

Frequency (GHz)	67	76.5	86
Beam Efficiency (%)	82.71	83.33	83.64
XsP at secondary (dB)	-30.52	-31.59	-32.57

Table 4.3: Beam efficiency and cross-polarization for the grid files produced using hybrid mode conical horn

4.4 Comparison with the 3mm system

As the 4 mm system was based on the design of an existing system operating at wavelengths around 3 mm, it was important to compare the operation of the 4 mm system with that of the existing 3 mm design. The 3mm design was constructed using a 100 mm horn-cryostat separation and with a horn having a 12 mm aperture and a 97.73 mm slant length. It was designed to operate between 85 and 116 GHz.

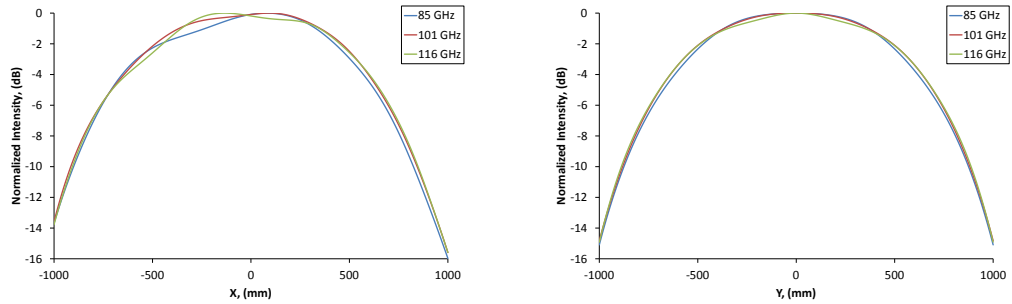


Figure 4.15: Cuts of the Hybrid Mode Horn at the Secondary Mirror for the 3 mm system

Cuts of the field at the secondary mirror, generated using the GRASP Hybrid Mode horn are shown for the 3mm system in Figure 4.15. Similar aberrations to the new 4mm system can be seen in the x cut. This indicates that the aberration examined in the 4 mm system also exists for the 3 mm receiver. As the 3 mm receiver operates well, it is likely that the 4 mm receiver also will do so. The cross polar levels for the 3 mm receiver remain low, below -30 dB, and are not significant as this is a single polarization receiver

4.5 Experimental Measurements

The system was manufactured in autumn 2015, and initial test measurements were made at Onsala [47]. A pyramidal test horn (illustrated in figure 4.16) was used during the test measurements to collect the beam patterns at the various planes under investigation.

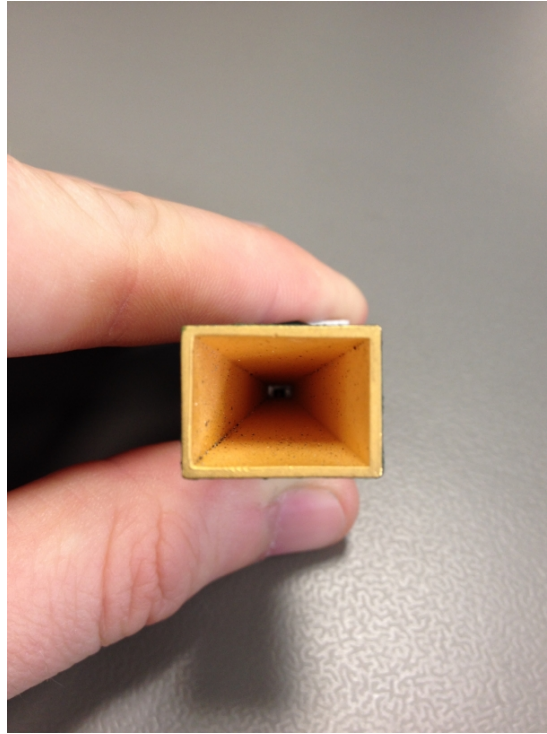


Figure 4.16: The test horn used for the measurements.

The dimensions of the test horn are given in figure 4.17. The horn is attached to a standard WR12 waveguide and as an operating frequency of 60.5–92 GHz, which includes the band across which the 4 mm receiver is to operate.

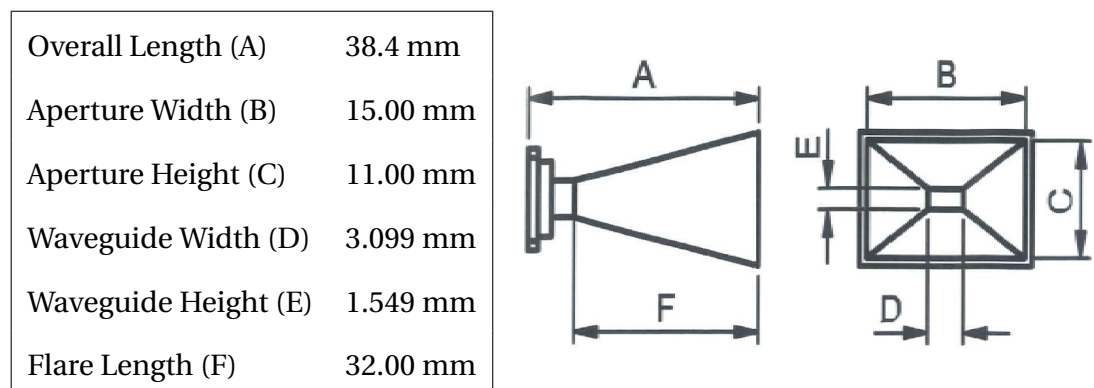


Figure 4.17: Dimensions of the test horn used, from the data sheet.

The beam pattern of the test horn has an effect on the measurements as it is convolved with the incoming test beam. For this reason, using a waveguide as a probe would be more convenient. However, as a pyramidal horn was used in this case, it was necessary to convolve the horn beam pattern with that of the GRASP simu-

lation in order to more accurately compare the experimental data more accurately with the simulations. Using the convolution theorem, the convolved beam is found from the Fourier transforms of the two component beams [48]:

$$[f * g] = \mathcal{F}^{-1} [\mathcal{F}[f] \cdot \mathcal{F}[g]], \quad (4.2)$$

where $*$ represents convolution and \mathcal{F} is the Fourier transform.

The aperture field for the pyramidal horn was represented by [49]

$$E_y = E_0 \cos \frac{\pi x}{A} \exp \left[-i \frac{k}{2} \left(\frac{x^2}{R_1^2} + \frac{y^2}{R_2^2} \right) \right], \quad (4.3)$$

where R_1 and R_2 for the test horn are 40.33 mm and 37.24 mm respectively, which were calculated from the dimensions given in figure 4.17.

There was also some misalignment between the aperture centre of the test horn and that of the 4 mm receiver window. Measurements found the offset of the receiver with respect to the test horn to be $x = -5.5$ mm and $y = 2.25$ mm. There was also an angular misalignment which resulted in the test horn pointing approximately 0.382° in the positive x direction. This is illustrated in figure 4.18.

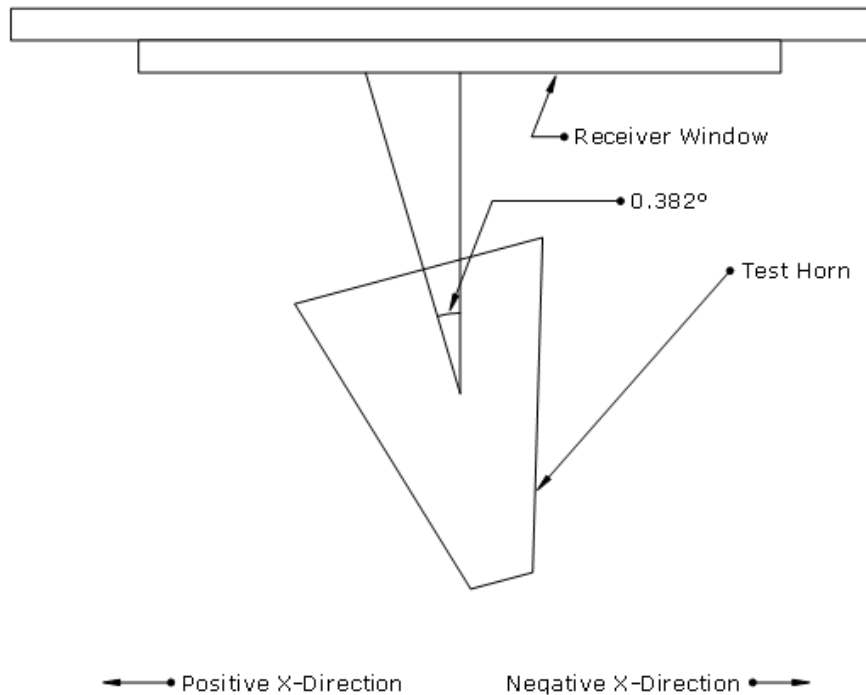


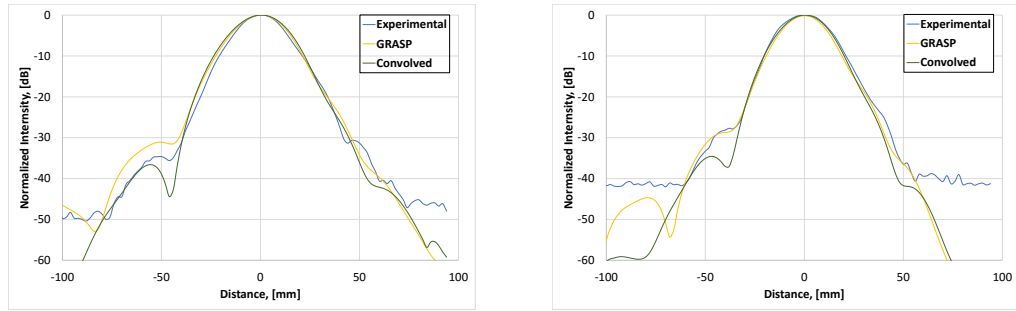
Figure 4.18: Measured misalignment between the test horn plane and the receiver plane. The angle is exaggerated for illustration purposes.

The misalignment was accounted for in GRASP by modifying the coordinates of the output grid. The test setup is illustrated in figure 4.19. The test horn is shown attached to the front of a hexapod, which controls the horizontal and vertical position of the test horn. Part of the cryostat unit is shown at the right of the photograph; the cryostat window is clearly visible, and is surrounded by absorber which reduces the effect of reflections from the front of the cryostat unit.



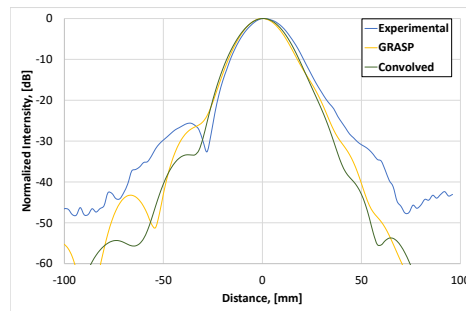
Figure 4.19: Beam test setup

Experimental measurements, taken a distance of 246 mm from the receiver front (which is 480.41 mm in optical distance) are shown in figures 4.20 and 4.21. These are plotted with the GRASP simulated beam (using the modematching tabular grids as source files), and the convolution of the GRASP beam with the aperture field of the test horn. The graphs show how the convolution provides a better fit with the experimental results.



(a) 69 GHz

(b) 79 GHz



(c) 86 GHz

Figure 4.20: Experimental results compared with GRASP; X cuts

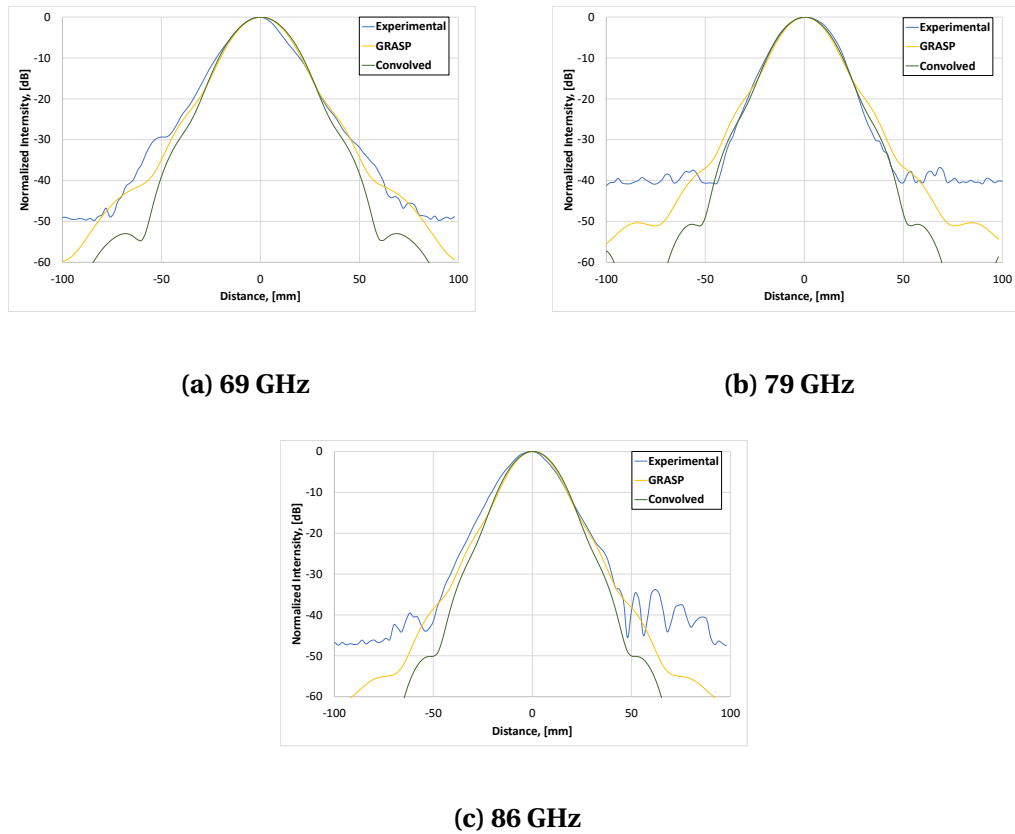


Figure 4.21: Experimental results compared with GRASP; Y cuts

4.6 Conclusion

In this chapter, further design and analysis of the 4 mm receiver system was presented, making extensive use of GRASP. The design of the receiver was verified with low cross-polar levels. In addition, a model beam was propagated through the telescope to the sky in GRASP, demonstrating that the aberrations have little effect on the practical optical performance of the system. The design was also compared with the existing 3 mm system, demonstrating similar performance. Finally, the GRASP simulation was compared with experimental results, and the experimental beam pattern was similar to the expected results from the simulation.

Chapter 5

W Band Lens Antenna Design and Analysis

Contents

5.1 Introduction	91
5.2 Planar Antenna theory	91
5.2.1 Analysis of Patch Antennae	92
Rectangular Patch	94
Circular Patch	95
5.2.2 S-Parameter	95
5.2.3 Directivity	96
5.2.4 CST Microwave Studio	96
5.3 Circular Patch	98
5.3.1 Addition of HDPE lenses	100
5.3.2 Wrap around lens	103
5.4 Alternative patch designs	106
5.4.1 Square patch	106
5.4.2 H-antenna dipole	107
5.4.3 Ellipsoidal lens	108
5.4.4 Rectangular patch antenna	109
5.5 Further Design Considerations	112
5.6 Conclusion	116

5.1 Introduction

In this chapter, the development of lens antennae with good beam characteristics are explored as an alternative to horn antennae for the W band (75–110 GHz). A lens antenna is defined as a planar antenna coupled with a dielectric lens, often referred to as a lenslet, to add directionality to the associated beam. A number of designs are outlined and analysed, and at the time of writing, preliminary measurements of initial patch antenna designs are being made with the vector network analyser at Maynooth.

5.2 Planar Antenna theory

Patch antennae, also known as printed antennae, are commonly used in a variety of classical microwave applications. Examples include radars, telecommunications, satellites, GPS, and mobile communications. Patch antennae can be quite cheaply produced using printed circuit technology, and have become smaller over time with the general trend of the miniaturization of electronic devices. In addition to ease of manufacturing, they have several other advantages, including light weight and small dimensions, easy integration with electronic components, and the possibility of being easily made into arrays. At Maynooth, the patch antennae were etched on Rogers dielectric using the traditional circuit board manufacturing techniques.

For these reasons, they are being investigated as an alternative to the traditional horn antenna at submillimetre wavelengths. However, there are some drawbacks to the use of a patch antenna, including a relatively narrow bandwidth, except for complicated geometries, and several effects such as dielectric losses and surface waves, which may lead to a low efficiency. In addition, for a patch antenna to oper-

ate at the higher frequencies associated with submillimetre wavelengths, its physical dimensions must be much smaller than one operating at traditional microwave frequencies. This represents an additional manufacturing complication.

The simplest type of patch antenna is a metallic patch printed on one side of a dielectric, with the other side of the dielectric being a completely metallized ground plane. The patch may be manufactured in a variety of different shapes; for example, circular, rectangular, triangular, etc. The patch is excited, or fed, by a transmission line between the ground plane and the patch. There is a variety of methods of achieving this, including coaxial, microstrip, or coplanar feeds. A coaxial feed consists of a central conductor going through the dielectric and being electrically connected to the patch, and an outer conductor connected to the ground plane. The central wire is isolated from the ground by dielectric material. This is the feed method that is used throughout the analysis presented in this chapter.

5.2.1 Analysis of Patch Antennae

The method of analysis presented here is known as the *cavity method*, and is a simple approximation, which helps with the understanding of the physical operation of the antenna [49]. The cavity in this model refers to the volume between the patch and the ground plane. The approximation consists of assuming that the patch is a perfectly conducting metallic surface S with a closed boundary C . The patch is on a dielectric substrate, which has a relative permittivity ϵ_r , and thickness h . This is illustrated in figure 5.1. This method also assumes that the electric field is localized in the volume between the patch and the ground plane, and that the radiation is the result of leakage from the cavity through the side walls.

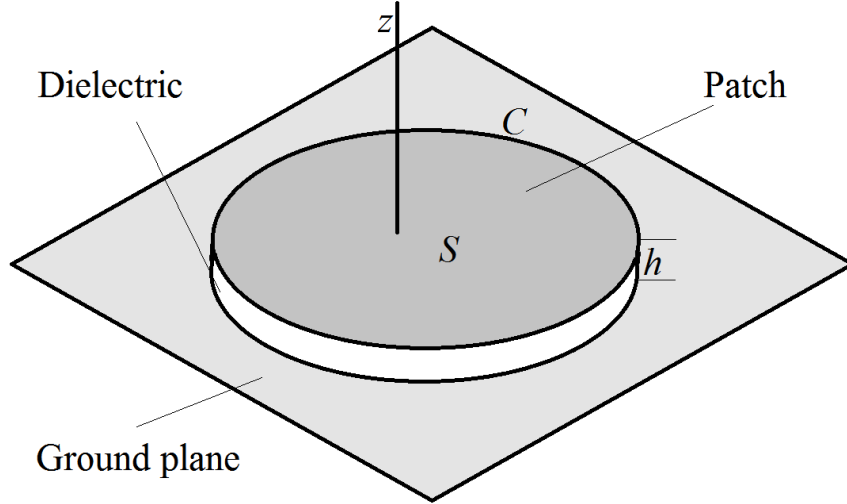


Figure 5.1: The patch antenna is considered as an electromagnetic cavity.

Assuming h is small when compared with the wavelength λ_d , it can also be assumed that the electric and magnetic fields \mathbf{E} and \mathbf{H} are independent of z , where z is the position along the axis perpendicular to the plane of the patch antenna. It can also be assumed that the electric field \mathbf{E} in the cavity is parallel to \mathbf{u}_z , where \mathbf{u}_z is in the direction of propagation [49]. Under these approximations, Maxwell's equations reduce the electric field to a single component $E_z(x, y)$ within the cavity, so that

$$\mathbf{E} = E_z \mathbf{u}_z, \quad (5.1)$$

which gives

$$\mathbf{H} = -\frac{i}{\omega\mu} \mathbf{u}_z \times \nabla E_z, \quad (5.2)$$

where ω is the angular frequency $2\pi f$ and μ is the magnetic permeability. The surface current density \mathbf{J}_s on the dielectric side of the patch is given by

$$\mathbf{J}_s \times \mathbf{u}_z = -\frac{i}{\omega\mu} \nabla E_z. \quad (5.3)$$

In order to calculate E_z , the boundary conditions at the walls of the cavity are im-

posed, along with the Helmholtz equation

$$\nabla^2 E_z + \omega^2 \epsilon \mu E_z = 0. \quad (5.4)$$

The surface density \mathbf{J}_s must be tangent to the boundary, and the magnetic field, from $\mathbf{H} = \mathbf{u}_z \times \mathbf{J}_s$, must then be normal to the lateral walls of the cavity. Therefore, the component E_z must also satisfy

$$\mathbf{n} \cdot \nabla E_z = 0 \quad (5.5)$$

on the contour C , which surrounds the patch, where \mathbf{n} is a vector perpendicular to C and the lateral walls. From these conditions, the farfield approximation $\mathbf{E}(\mathbf{r})$ of the radiated electric field, at a point M defined by \mathbf{r} in the direction \mathbf{u} may be expressed as

$$\mathbf{E}(\mathbf{r}) = -\frac{ih}{\lambda} \frac{\exp(-ikr)}{r} \int_C E_z(\mathbf{r}') \exp(ikr') \cos \psi \, dc, \quad (5.6)$$

where \mathbf{r} defines the position of the point of observation, \mathbf{r}' defines a point M' on C , $E_z(\mathbf{r}')$ is the field at the point M' on the lateral wall of the cavity, and dc is the element of the contour C at this point.

Rectangular Patch

For a rectangular patch with dimensions a and b on a substrate characterized by its dielectric properties ϵ and μ with thickness h , the component E_z satisfies the Helmholtz equation 5.4 with the following boundary conditions:

$$\begin{aligned} \frac{\partial E_z}{\partial y} &= 0 & \text{for } x = 0, x = a; \\ \frac{\partial E_z}{\partial x} &= 0 & \text{for } y = 0, y = b. \end{aligned} \quad (5.7)$$

E_z may then be calculated by separation of variables, such that

$$E_z = E_0 \cos \frac{m\pi x}{a} \cos \frac{n\pi y}{b}, \quad (5.8)$$

where E_0 is an integration constant, and the integers m and n are related to the angular frequency ω by

$$\left(\frac{m\pi}{a}\right)^2 + \left(\frac{n\pi}{b}\right)^2 = \omega^2 \epsilon \mu. \quad (5.9)$$

Circular Patch

For a circular patch with radius a on a substrate characterized by its dielectric properties ϵ and μ with thickness h , the Helmholtz equation satisfied by the electric field E_z may be written in polar coordinates (ρ, ϕ) as

$$\frac{\partial^2 E_z}{\partial \rho^2} + \frac{1}{\rho} \frac{\partial E_z}{\partial \rho} + \frac{1}{\rho^2} \frac{\partial^2 E_z}{\partial \phi^2} + \omega^2 \epsilon \mu E_z = 0. \quad (5.10)$$

The boundary condition is

$$\frac{\partial E_z}{\partial \rho} = 0 \quad \text{at } \rho = a. \quad (5.11)$$

The solution for the electric field may be written as

$$E_z = E_0 \frac{J_m(\omega \sqrt{\epsilon \mu} \rho)}{J_m(\omega \sqrt{\epsilon \mu} a)} \cos m\phi, \quad (5.12)$$

where E_0 is an integration constant, as before, and $J_m(x)$ is the Bessel function of order m .

5.2.2 S-Parameter

The scattering parameter represents power transferred from one port to another in a system.

The S_{11} parameter represents the power reflected back compared with the incident power. If absorption is low, this is equivalent to $1 - S_{21}$, the power radiated by the antenna, as all the incident power is either radiated or reflected back, as they are two port systems. A low S_{11} parameter (and corresponding high S_{21} parameter) indi-

cates that the antenna is resonant at this frequency, and that most of the delivered power is radiated. In the remainder of this thesis, "S parameter" refers to the S_{11} parameter. These are given in dB — an S parameter close to zero indicates most of the beam is reflected back, demonstrating transmission in the case of the patch antenna

For the lens antennae, the S parameter shows if the antenna is resonant, and its bandwidth of operation. As the antennae are to be resonant in the W band, a low S parameter in the range 75–110 GHz is of utmost importance. In the designs outlined, the resonant transmission is desired to be closer to 75 GHz, as the wavelength is longer, so the antenna is easier to manufacture when compared with the higher 110 GHz end of the W band range.

5.2.3 Directivity

Directivity is a measure of the maximum power density radiated by an antenna in the direction of its strongest emission, with reference to that of an isotropic radiator. It is usually given in decibels. In this chapter, directivity is an important parameter used to characterize the antenna designs, as directional antennae are desirable for optical receivers. The aim is to increase directivity by modifying the design of the antenna, and with the addition of a lens in front of the antenna, as patch antennae alone have a low directivity.

5.2.4 CST Microwave Studio

CST (Computer Simulation Technology) Microwave Studio is a commercially available software package for electromagnetic design and analysis in the high frequency range. The program uses finite integration techniques to carry out electromagnetic simulations. These techniques solve the integral form of Maxwell's equations [32][50].

A model is initially constructed within CST using the inbuilt computer aided design tools. In order to solve the problem numerically, a finite calculation is defined before a simulation engine is started. This is achieved by a mesh system which divides the model into many grid cells. While the primary mesh can be visualized in CST, a second mesh is set up internally that is orthogonal to the first one. This is illustrated in figure 5.2.

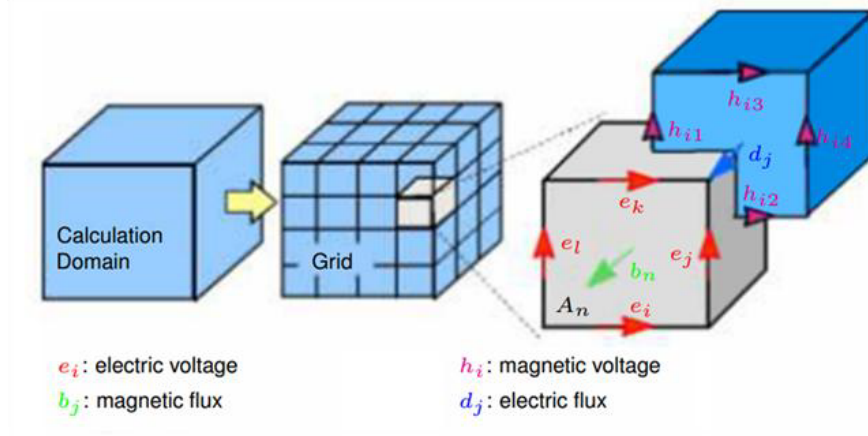


Figure 5.2: The CST Mesh system

This can be illustrated by considering the integral form of Faraday's law [50]:

$$\int E \cdot dS = -\frac{\partial}{\partial t} \iint B \cdot dA. \quad (5.13)$$

The closed integral $\int E \cdot dS$ for a mesh cell can be rewritten as the sum of four grid voltages ($e_i + e_j - e_k - e_l$), as shown in figure 5.2. The magnetic flux on the enclosed face b_n equals $\iint B \cdot dA$. From these,

$$e_i + e_j - e_k - e_l = -\frac{\partial}{\partial t} b_n. \quad (5.14)$$

Repeating this for all cells results in a matrix formulation as follows:

$$\begin{pmatrix} \vdots & \vdots & \vdots & \vdots \\ 1 & 1 & -1 & -1 \\ \vdots & \vdots & \vdots & \vdots \end{pmatrix} \begin{pmatrix} e_i \\ e_j \\ e_k \\ e_l \end{pmatrix} = -\frac{\partial}{\partial t} \begin{pmatrix} \vdots \\ b_n \\ \vdots \end{pmatrix} \quad (5.15)$$

The software has a variety of simulation techniques; the time domain and frequency domain solvers are considered here. The choice of solver is important in producing accurate and efficient simulations, and is also determined by the type of system being considered.

The time domain solver allows the entire broadband frequency behaviour of a device to be simulated in a single calculation. This method is efficient for most high frequency applications such as connectors, transmission lines, and antennae. It is also suitable for non-linear and time-varying problems. It uses a hexagonal mesh, and is based on the discretized set of Maxwell's grid equation, with the central differences being substituted for time derivatives. This is the solver that is most suitable for the problems considered in this chapter.

The time domain solver is not as efficient for resonant problems, or for structures that have dimensions less than that of the wavelengths of interest, such as the detector cavities considered in chapter 6. In such cases, the frequency domain solver is more suitable.

5.3 Circular Patch

A circular patch antenna was initially considered. This design is a scaled S band (2–4 GHz) model [51], with the dimensions reduced so that it would be approximately resonant at 100 GHz in the W band. The design of this antenna is shown in figure

5.3. The metal patch itself has a radius of 0.464 mm, the substrate is modelled as a square, with dimensions of 1.2 mm, and a thickness of 0.014 mm, which is attached to the ground plane of thickness 0.042 mm. The patch is fed with a wire of radius 0.02 mm and an offset of 0.184 in the y direction from the centre of the patch. The wire is separated from the ground plane by a cylinder of substrate of radius 0.08 mm. The substrate (green in the figures) is defined to have a relative permittivity of 2.33.

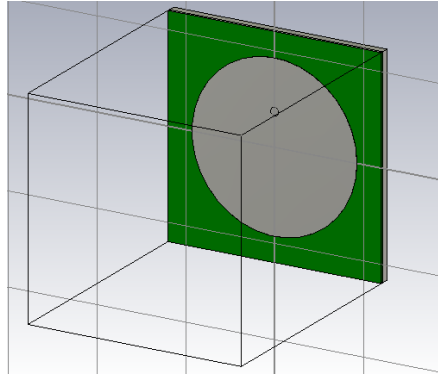


Figure 5.3: Initial circular patch considered in CST

The S-parameter of this design is shown in figure 5.4, showing that it is resonant at approximately 101 GHz. There is a very narrow bandwidth over which the design is resonant.

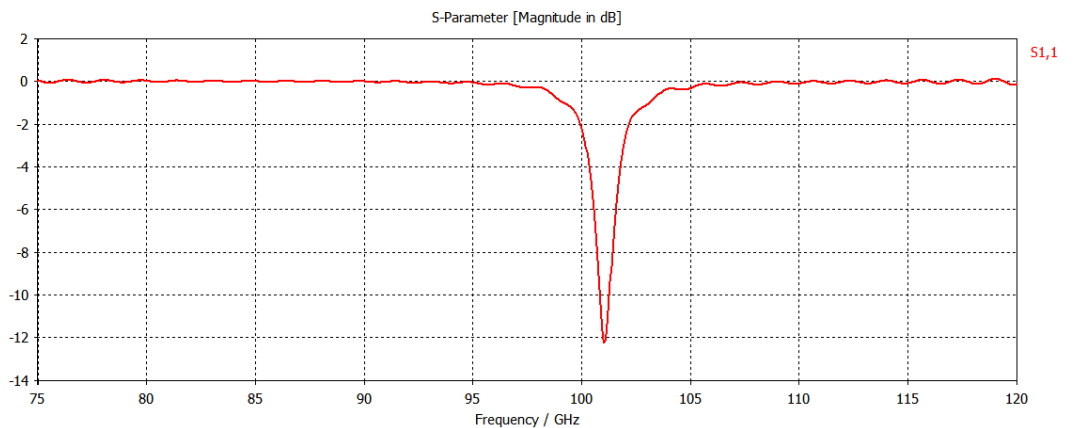


Figure 5.4: S-parameter of the initial circular patch

In order to realize a directional beam reduce the cross talk or mutual coupling between such pixels, the antenna must produce a more directional beam pattern. For this reason, the farfield directivity was the primary parameter of interest in this

project. Also of note is the angular width, which is the angle at which the directivity falls by 3 dB, or is reduced to half the peak directivity. The farfield directivity for the circular patch is shown in figure 5.5. This graph shows that the peak directivity is only 5.84 dB, and the angular width is 85.4 degrees, which means that the antenna is picking up radiation from all directions frontal, and is radiating from all effective angles in front of the antenna.

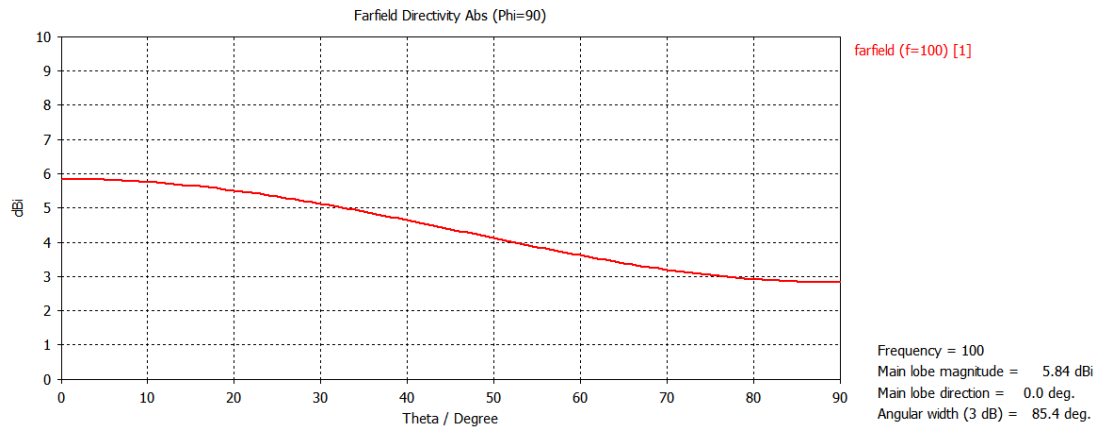
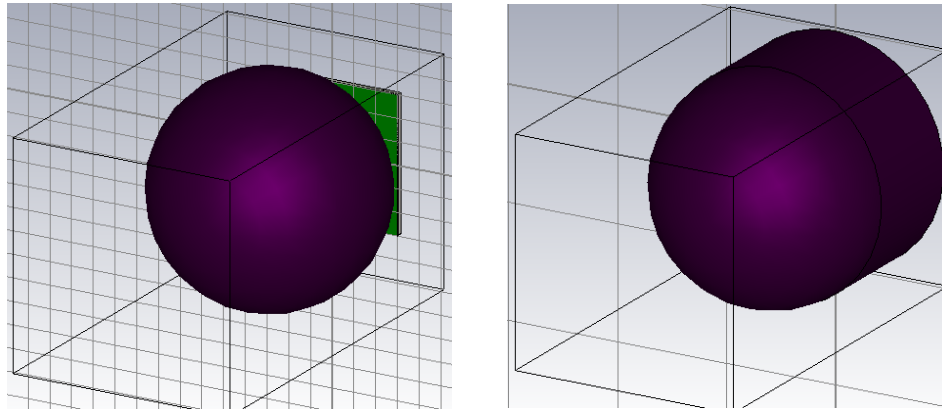


Figure 5.5: Farfield directivity of the initial circular patch

5.3.1 Addition of HDPE lenses

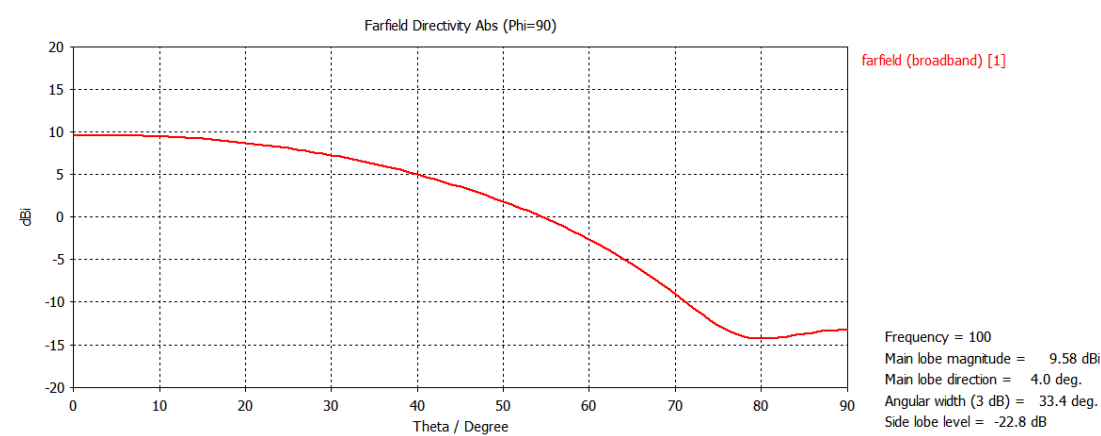
Both spherical and hemispherical lenses were then considered in order to produce a more directional beam when coupled with the patch antenna described above. These are shown in figure 5.6 for lenses with a radius of 1 mm. The lenses are made of high density polyethylene, which is defined in CST as having a relative permittivity of 2.4. With a radius of 1 mm, this lens is larger than the described patch antenna, but will need to be much larger than the wavelength to be of practical use.



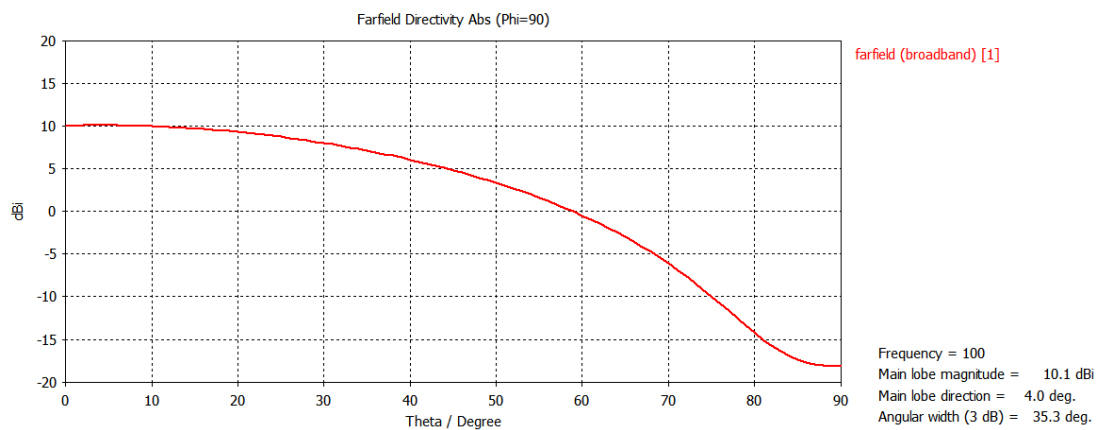
(a) Patch with spherical HDPE lens (b) Patch with hemispherical HDPE lens

Figure 5.6: Patch antenna and lens

Figure 5.7 shows the results for farfield directivity in these cases, where the lenses have radii of 1 mm. Immediately, the beam has become more directional, with slightly better results in the case of the hemispherical lens. The hemispherical lens type was chosen for further analysis as it is a better design to implement when compared with a spherical lens; the hemisphere and cylinder can be simply attached to the front of the antenna, whereas for the spherical lens a more complicated mounting system would have to be used.



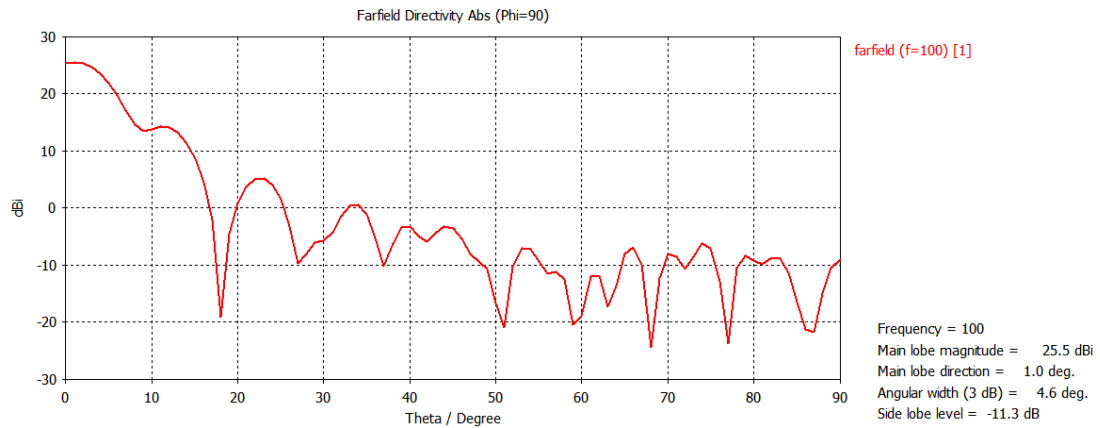
(a) Farfield directivity of circular antenna with 1 mm spherical lens



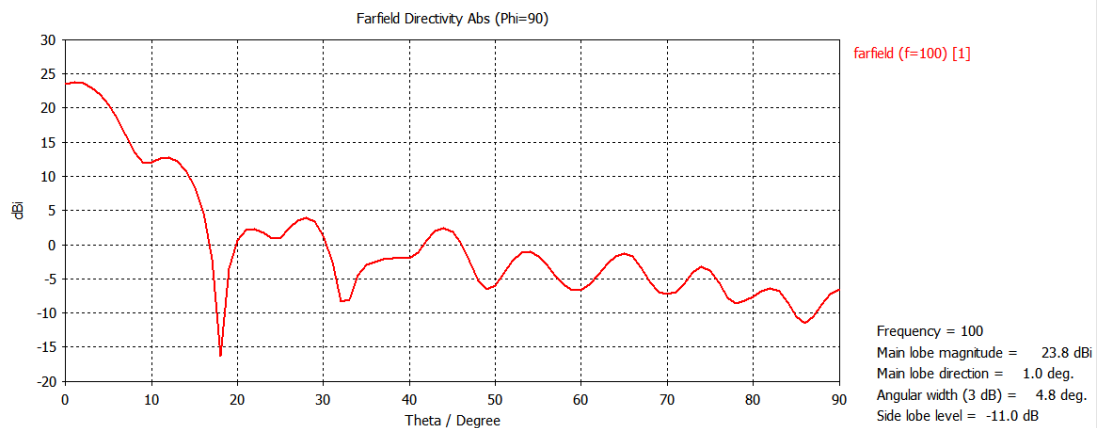
(b) Farfield directivity of circular antenna with 1 mm hemispherical lens

Figure 5.7: Patch antenna and 1 mm lens

Figure 5.8 shows the results for farfield directivity when the lenses have a radius of 10 mm, which is a much more realistic dimension. In this case, the directivity is much higher, with a slightly better result for the spherical lens than for the hemispherical lens. However, for ease of implementation, manufacture, and experimental alignment, it was decided to continue analysis with the hemispherical lens. With the 1 mm radius hemispherical lens, all the radiation from the patch is probably not coupled into the lens as its volume is too small to catch the off-axis radiation from the patch. In order to investigate this effect, the size of the lens is increased to a 10 mm radius.



(a) Farfield directivity of circular antenna with 10 mm spherical lens



(b) Farfield directivity of circular antenna with 10 mm hemispherical lens

Figure 5.8: Patch antenna and 10 mm lens

The farfield with combination of the circular patch and the hemispherical lens demonstrates that good directionality has been achieved, and the -3 dB level is only at about 5 degrees, which indicates good directional beam qualities.

5.3.2 Wrap around lens

Optical fibres work by wrapping a central medium (core) with one of a slightly lower refractive index (cladding) in order to produce total internal reflection. A similar principle is attempted here by wrapping the lens in front of the antenna with material of a slightly lower refractive index. Total internal reflection occurs when a propagating wave strikes the medium boundary at an angle of incidence larger than the

critical angle. This critical angle can be found from Snell's law [52]:

$$n_1 \sin \theta_i = n_2 \sin \theta_t, \quad (5.16)$$

where n_1 and n_2 are the refractive indices of the core and the cladding respectively, and θ_i and θ_t are the incident and transmitted angles, as illustrated in figure 5.9.

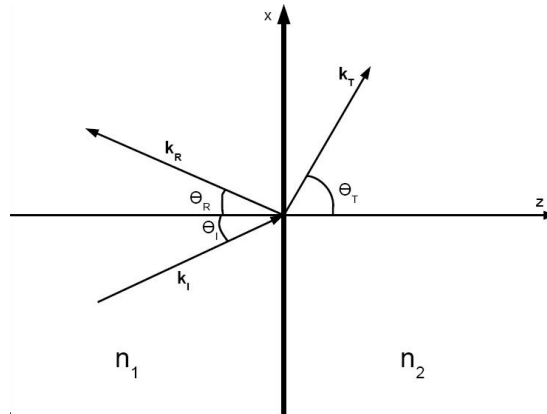


Figure 5.9: Illustration of Snell's Law [53].

The critical angle θ_c is defined as the value of θ_i when θ_t reaches 90° , given by

$$\sin \theta_c = \frac{n_2}{n_1} \sin \theta_t. \quad (5.17)$$

The lens surrounded by a wrap is shown in figure 5.10. The wrap material has a relative permittivity of 1.5, which is less than that of the lens material. As the relative permittivity of the central lens is 2.4, from equation 5.17, the critical angle is 38.7° , so lower sidelobes are expected beyond this angle.

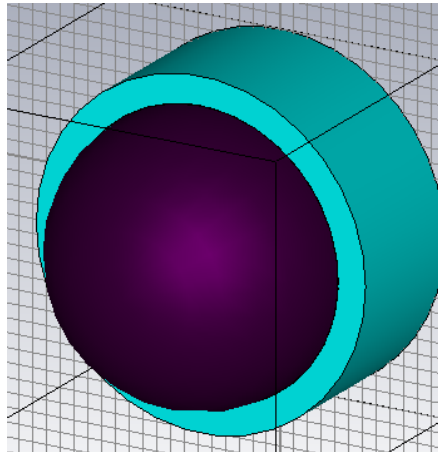


Figure 5.10: Lens antenna with surrounding wrap

Figure 5.11 shows the results for farfield directivity in this case. The lens radius has been kept at 10 mm, and the wrap extends 2 mm beyond this. From the graph, the directivity is only slightly improved in this case, with a directivity of 24 dB, compared to 23.8 dB is the case without the wrap (figure 5.8b). However, the sidelobe level has dropped from -11 dB to -20.8 dB, which indicates that the addition of the wrapping material has an effect, as expected. Further investigation using the wrap could include the variation of its thickness, and the refractive index, as these parameters probably have an effect on the operation of the device.

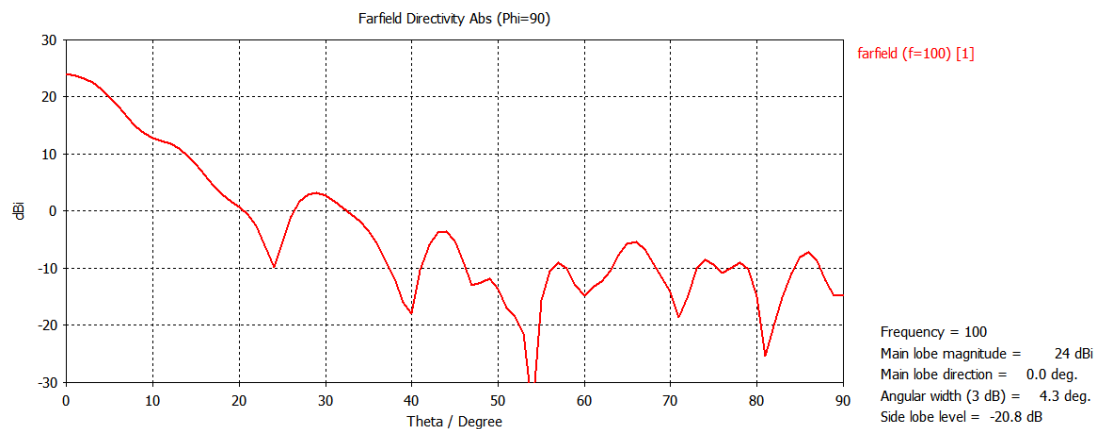


Figure 5.11: Directivity of circular patch antenna with wrapped hemispherical lens

5.4 Alternative patch designs

5.4.1 Square patch

Following from this, some different antenna structures were considered in an attempt to provide a greater directivity before the inclusion of a lens structure. A square antenna, based on the previous circular antenna, is shown in figure 5.12. The patch has dimensions of $1 \text{ mm} \times 1 \text{ mm}$. The other parameters (dielectric thickness, etc.) were kept the same as for the previous case.

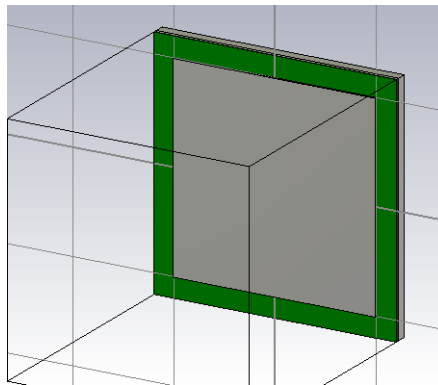


Figure 5.12: Square patch considered in CST

The S parameter of this patch design is shown in figure 5.13. This design clearly is much more resonant over the band than the circular design considered previously.

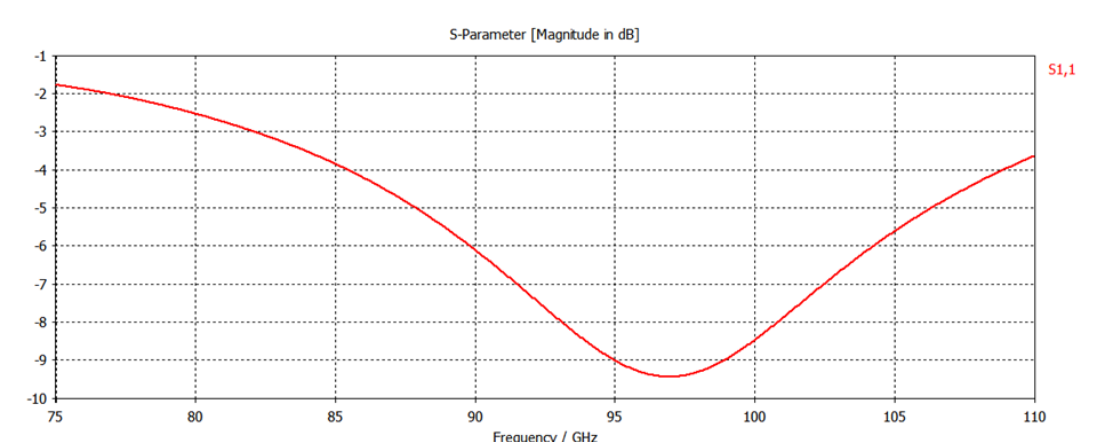


Figure 5.13: S parameter of the square patch.

Figure 5.14 shows the farfield directivity of the square patch, which is much better

than that of the initial circular patch that was considered, with a peak directivity of 7.58 dB, and an angular width of 44.3 degrees.

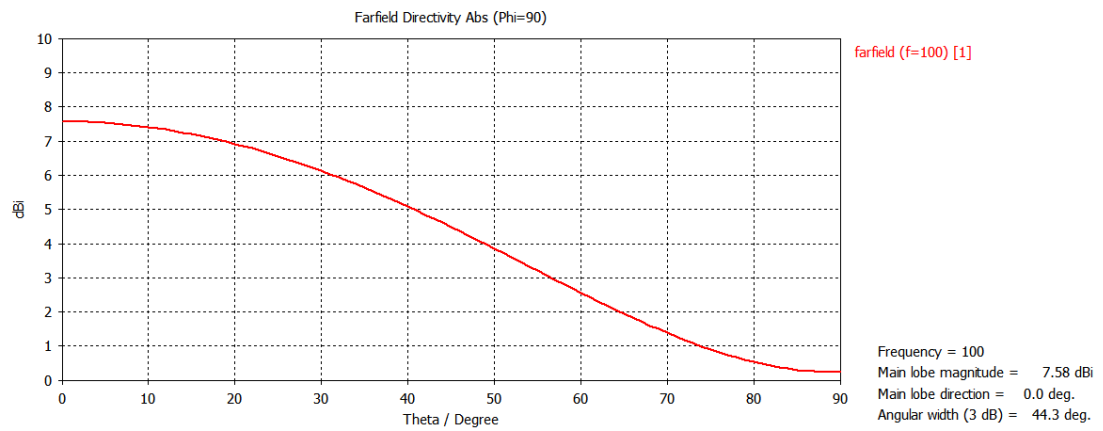


Figure 5.14: Farfield directivity of the square patch.

5.4.2 H-antenna dipole

In an attempt to improve the directionality of the antenna, the following dipole H-shaped antenna was developed, as shown in figure 5.15. This is another planar antenna design that is potentially easy to manufacture and has high gain farfield patterns equivalent to a patch antenna. The bars have a width of 0.025 mm, and the central bar is at a position 0.184 mm from the centre, which is the position of the input feed. The other parameters were kept the same.

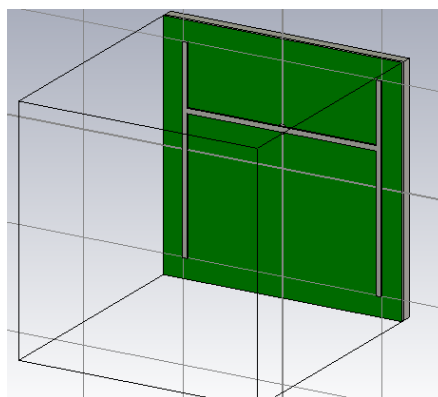


Figure 5.15: H-shaped patch antenna considered in CST.

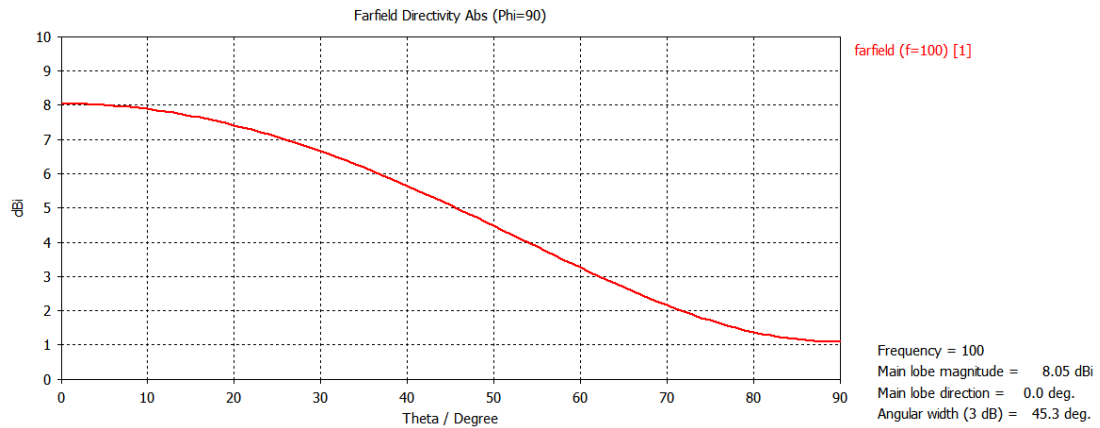


Figure 5.16: Farfield directivity of the H-shaped patch.

This design has a slightly improved directivity when compared with the square patch antenna, although would be much more difficult to manufacture, and this difficulty would outweigh the potential benefits of the design.

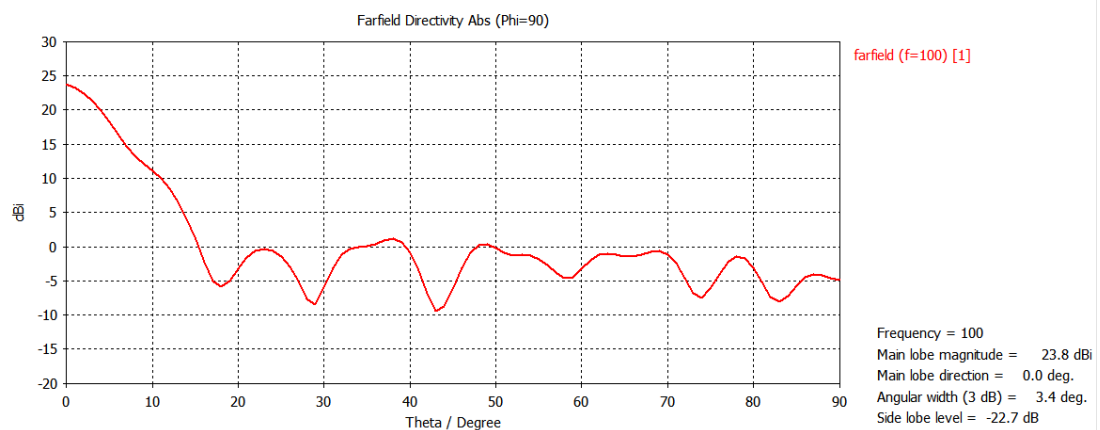


Figure 5.17: Farfield directivity of the H-shaped patch with an hemispherical lens

5.4.3 Ellipsoidal lens

Following this, the effect of using an ellipsoidal lens, with the antenna at one of the focal lengths were considered [54]. An example of this modelled in CST is shown in figure 5.18. The lens has a major axis of 12 mm and a minor axis of 10 mm, which provides the best result for directivity without the lens getting too large.

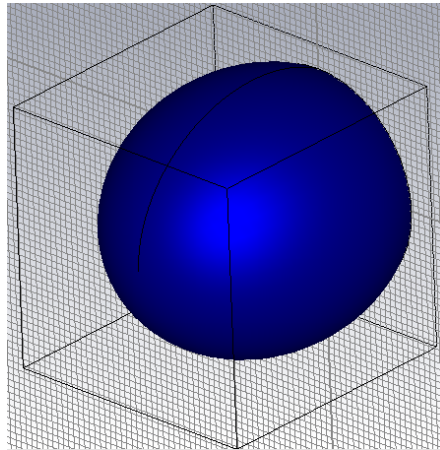


Figure 5.18: Ellipsoidal lens in CST.

In this case, the directivity is slightly reduced when compared with the hemispherical lens, as shown in figure 5.19. The hemispherical lens would also be easier to manufacture.

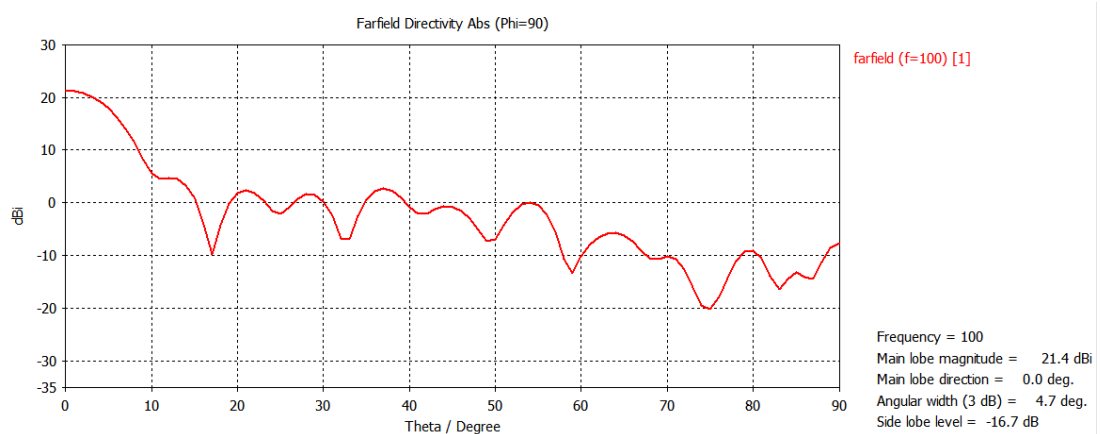


Figure 5.19: Farfield directivity of the H-shaped patch with an ellipsoidal lens.

5.4.4 Rectangular patch antenna

The following rectangular patch design was developed with reference to the previous designs, but additionally allowing an increase in the thickness of the dielectric substrate. This design is shown in figure 5.21. The substrate material has a permittivity of 3.3, as before. The substrate thickness has been increased to 0.25 mm to produce a design resonant around 100 GHz, as shown in figure 5.20. The size of the patch has also been altered slightly for this purpose to be 0.7 mm × 1.0 mm. The

position of the input feed has been increased to 0.48 mm, with the result that the feed is just at the top of the patch, as this made the beam more directional.

Figure 5.20 shows the S-parameter for this

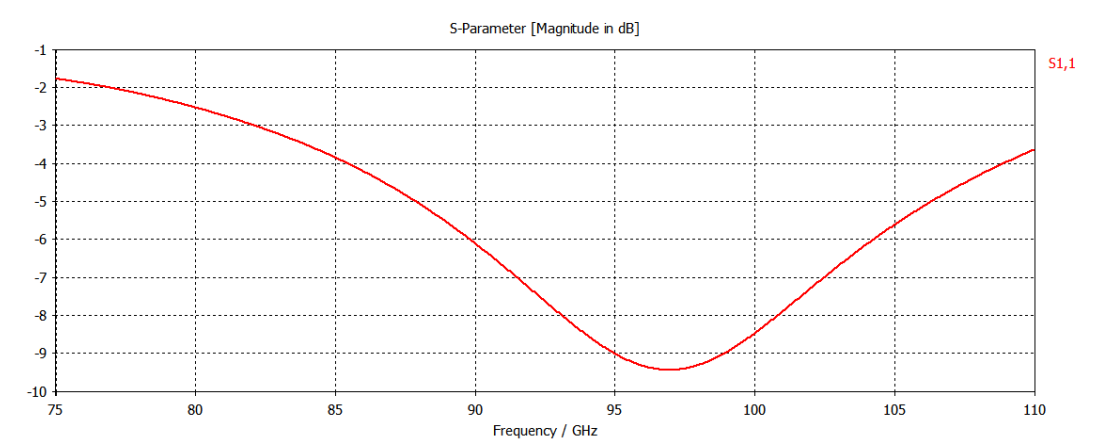


Figure 5.20: S-parameter rectangular patch

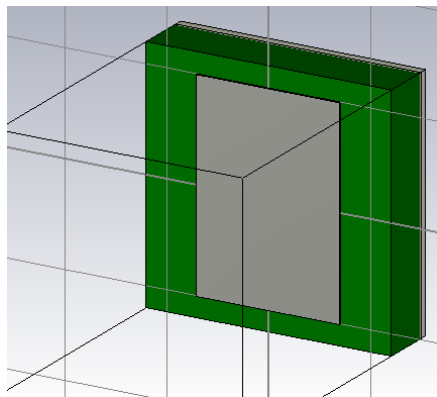


Figure 5.21: Rectangular patch design

The farfield directivity for this patch design is shown in figure 5.22. While this result of 6.83 dB is less than that of the earlier square patch design (figure 5.14), the directivity drops off significantly more quickly, to around -6 dB, and the angular width is only 35.3 degrees, which is better than all the other patch designs considered so far.

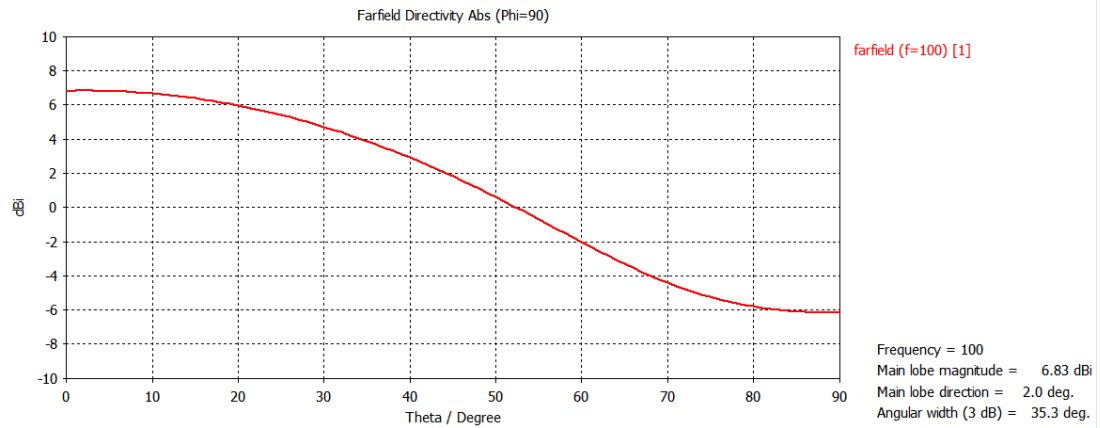
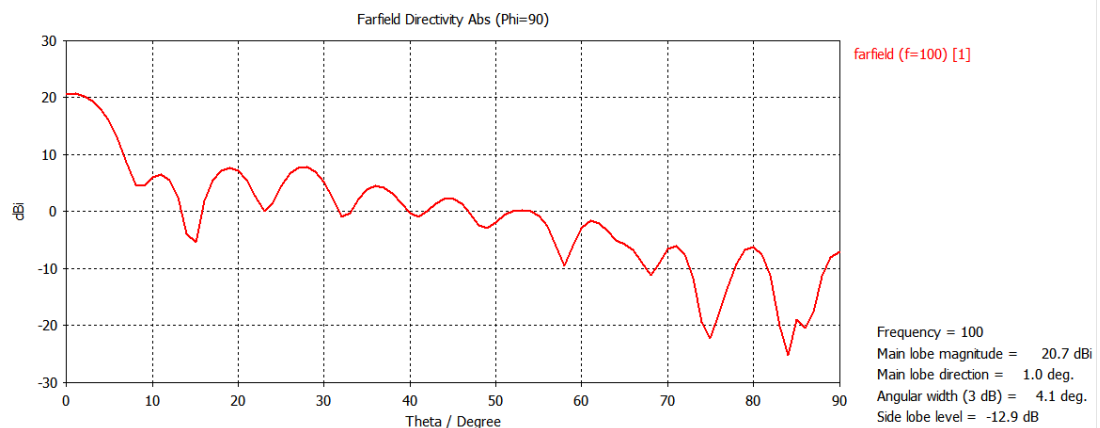
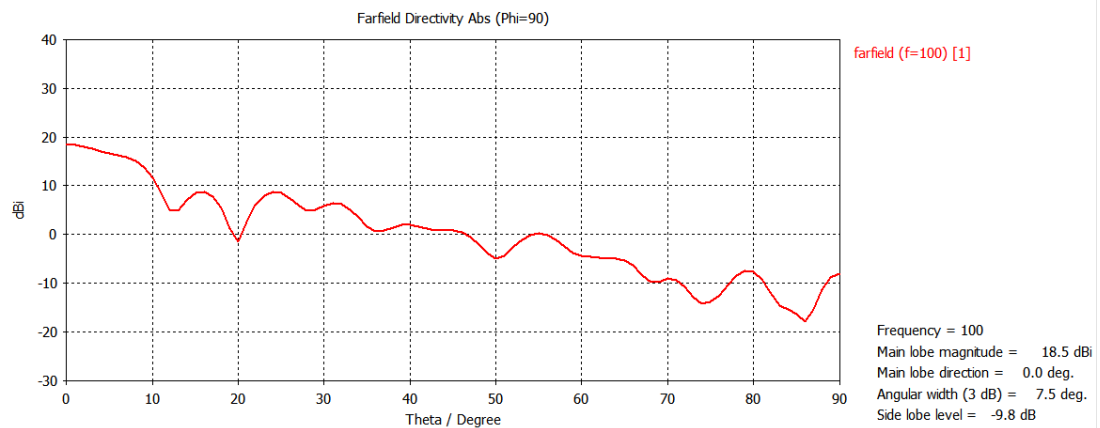


Figure 5.22: Farfield directivity rectangular patch

Figure 5.23a shows the farfield directivity of the rectangular patch with an ellipsoidal lens. The major and minor axes were 12 mm and 10 mm respectively, which gave the best results without having the lens too large.



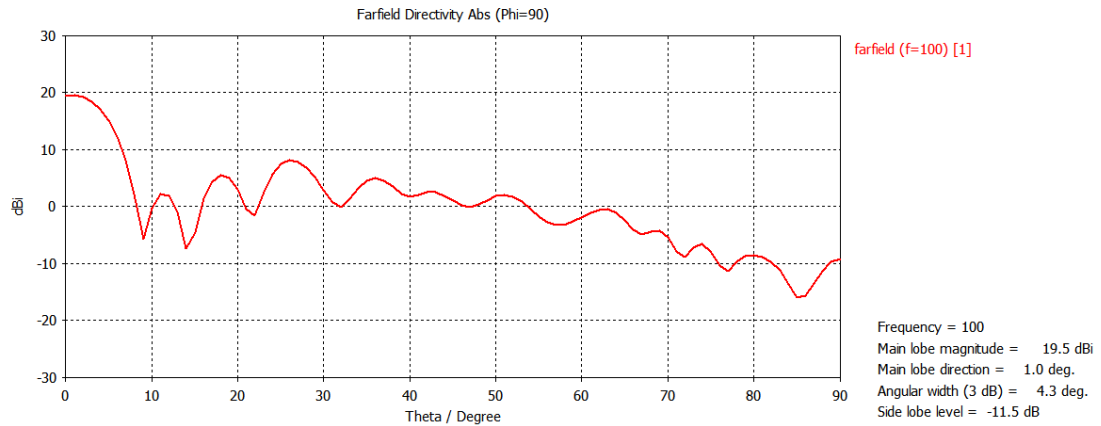
(a) Farfield directivity of rectangular patch with ellipsoidal lens



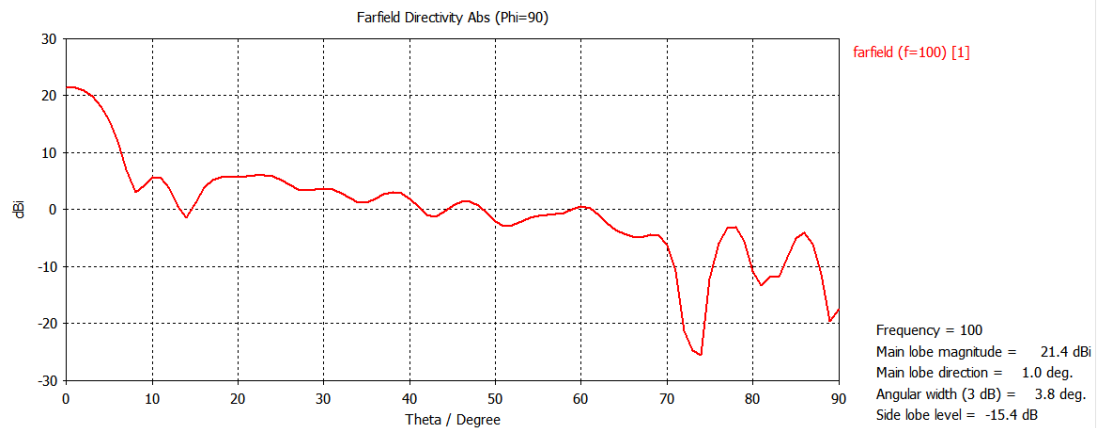
(b) Farfield directivity of rectangular patch with ellipsoidal lens with wrap

Figure 5.24a shows the farfield directivity of the rectangular patch with a hemispher-

ical lens that approximates the previous ellipsoidal lens. This approximation was achieved by setting the radius to be equal to the minor axis, and the total length of the cylinder and the hemisphere to be equal to twice the major axis minus the focal length.



(a) Farfield directivity of rectangular patch with hemispherical lens



(b) Farfield directivity of rectangular patch with hemispherical lens with wrap

The ellipsoidal lens provides a better result than the hemispherical approximation, but the hemispherical version could be used if it was less difficult to manufacture.

5.5 Further Design Considerations

Many different patch or planar antennae can be used in the W band, but for manufacture on the particular circuit board available, only certain designs will be resonant in the W band. This commercially available board is 0.8 mm thick with a

measured dielectric constant of 3.3 and an estimated loss tangent of 0.01.

The following design is based on these actual measurements of the thickness of a dielectric available to manufacture the antenna. The patch was optimized for 75 GHz, as this frequency provides the highest wavelength in the band, which is more convenient for manufacturing. The patch has a length of 1.0 mm, and a width of 0.9 mm, and is shifted in the x direction by 0.3 mm, relative to the coaxial feed. The substrate thickness is 0.1 mm, and the ground is 0.8 mm thick. The inner conductor has a radius of 0.14 mm. The inner conductor also protrudes from the back by 0.2 mm to assist with coupling. This patch design is shown in figure 5.25.

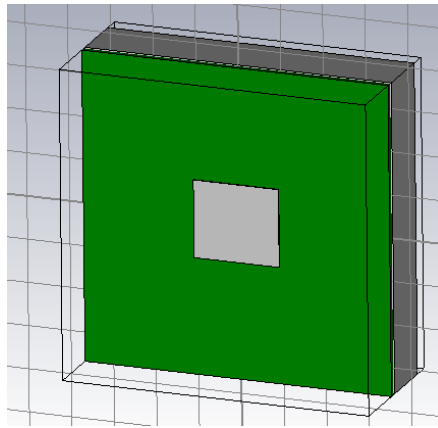


Figure 5.25: Design of patch to be manufactured.

The S parameter is shown in figure 5.26, demonstrating that this patch design is highly resonant in the W band.

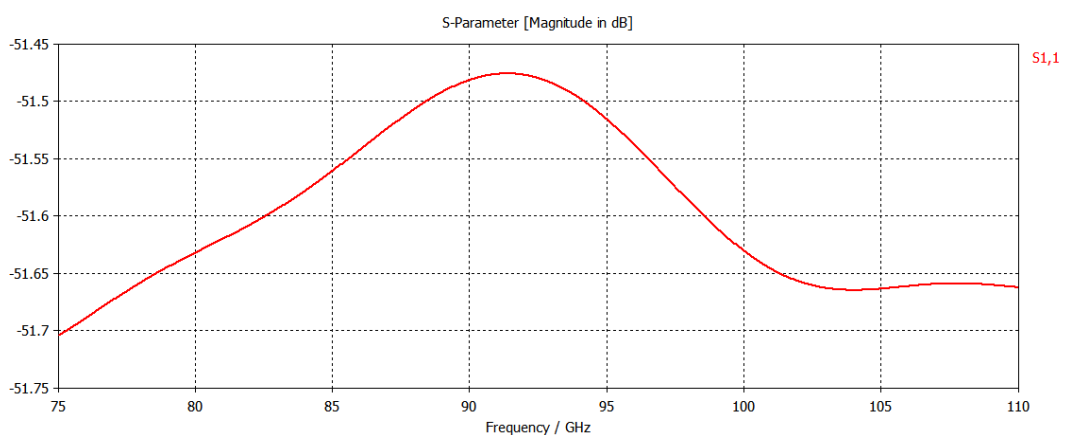


Figure 5.26: S-parameter for the patch to be manufactured.

The farfield directivity is shown in figure 5.27. The peak directivity is 3.2 dB, and the angular width is quite large at 92.3°, indicating the beam is radiating in all forward directions.

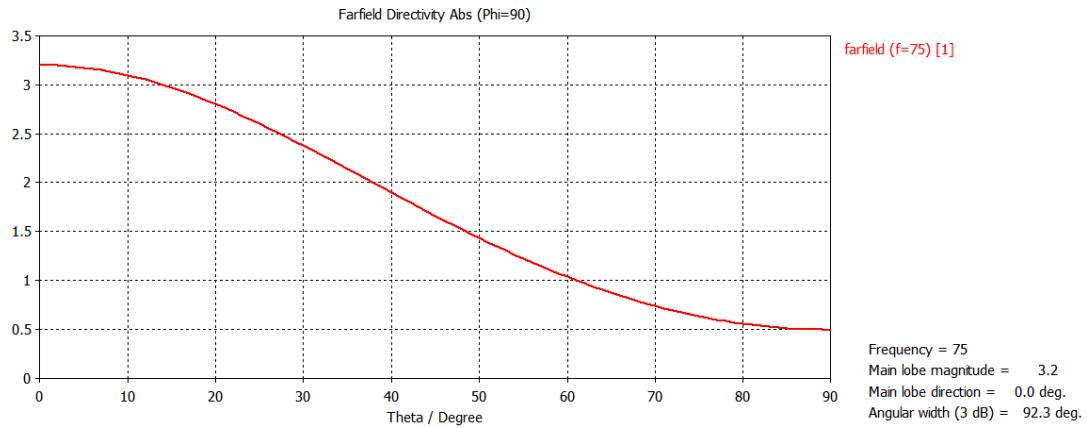


Figure 5.27: Cut of the farfield for the patch to be manufactured.

The addition of a hemispherical lens, using the same dimensions as before, has a large improvement in the directivity than for the bare antenna. Figure 5.28 shows that the directivity has increased to over 34 dB, with an angular width reduced to 15.9°.

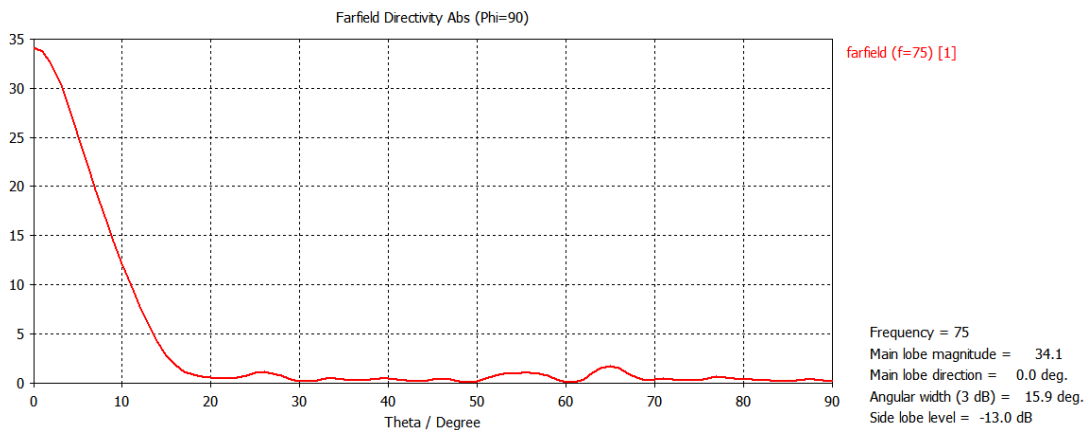


Figure 5.28: Cut of the farfield for the patch to be manufactured with hemispherical lens

The farfield directivity was found for an ellipsoidal lens at 75 GHz with a major axis of 14 mm and a minor axis of 10 mm; this is shown in figure 5.29. This result is better than the hemispherical lens, with a directivity of over 46 dB, and angular width at the 3 dB level is 9.3°.

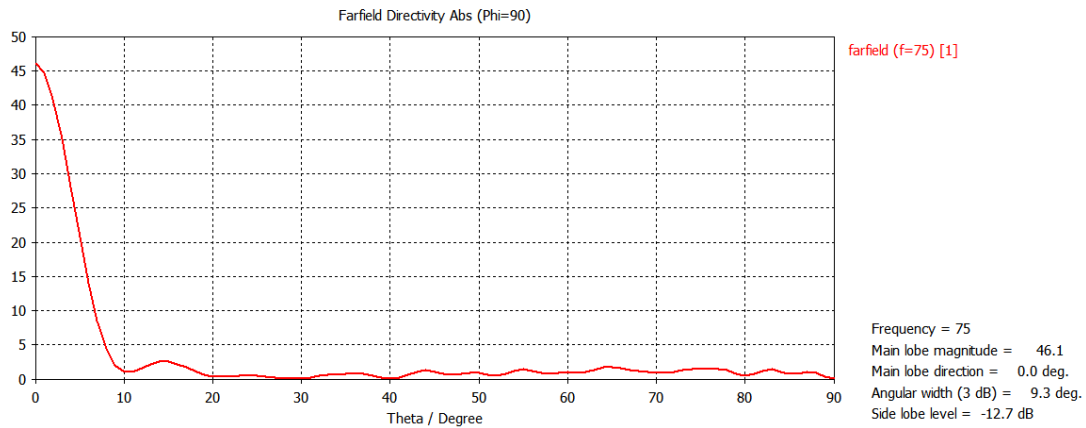


Figure 5.29: Farfield directivity for the patch to be manufactured with ellipsoidal lens

It must be noted that as a patch antenna has a narrow band of optimized performance, outside this band the performance is significantly decreased. This can be seen when the farfield directivity is measured at other frequencies, as shown in figure 5.30. The peak directivity at 85 GHz is reduced to 29.8 dB, and at 95 GHz, it is 17.5 dB. This clearly illustrates a drawback of the patch antenna, when compared with alternatives such as the horn antenna.

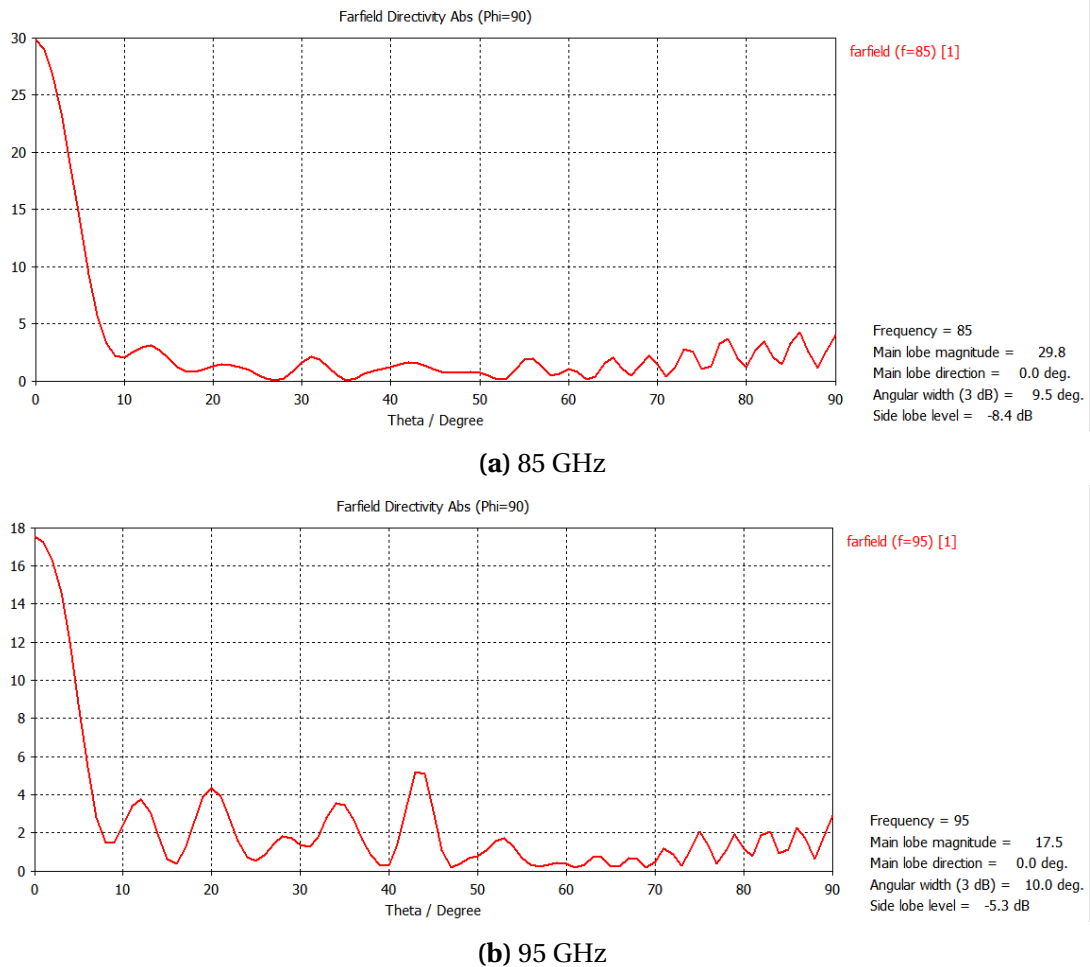


Figure 5.30: Farfield directivity for the patch to be manufactured with ellipsoidal lens at higher frequencies.

5.6 Conclusion

Various designs of planar antennae were considered. From these, the best results in terms of the angular width of the resulting beam were found for a rectangular patch antenna with dimensions of 1.0 mm \times 0.9 mm. The addition of various shaped lenses was found to greatly enhance the directionality of the beam, with the ellipsoidal lens providing a better result than a hemispherical lens for this particular patch design. However, there is a drawback in using a planar antenna, as there is only a narrow band across which performance can be optimized. Future plans include the manufacture and testing of this design at Maynooth.

Chapter 6

Detector Cavities

Contents

6.1 Background	117
6.2 Modelling of Detector Cavities within CST	118
6.3 Cavity 1	119
6.3.1 Optimization of Simulation Efficiency	120
6.3.2 Using Two Ohmic Sheets	122
6.3.3 Modelling the Ohmic sheet on a Dielectric	123
6.3.4 Offset Position of Waveguide	125
6.3.5 Absorber position	127
6.4 Cavity 2	128
6.4.1 Two Ohmic Sheets	128
6.4.2 Effect of Dielectric Thickness	129
6.4.3 Offset Position of Waveguide	131
6.5 Cavity 3	133
6.5.1 Two Ohmic Sheets	133
6.5.2 Effect of Dielectric Thickness	134
6.5.3 Offset Position of Waveguide	135
6.6 Conclusion	137

6.1 Background

This chapter examines the behaviour of rectangular waveguide detector cavities. These are sealed hollow waveguide structures, in which an absorbing layer associated with a detector (bolometer) can be placed to detect incident radiation. The

motivation behind this model type of waveguide-bounded detector is the trapping of all incident radiation in the cavity, so that energy not initially absorbed will be reflected back and forth, and may be absorbed subsequently. This method maximizes absorption [32], and will achieve higher optical coupling with this enclosing cavity than if the detector was just housed in free space. As a result, this method can increase the sensitivity for weak terahertz astronomical signals

Three different cavity sizes are presented in this chapter, along with the effect of varying the thickness of the dielectric layer, which is used to support the thin tantalum layer which acts as the resistive absorptive layer in the cavity and the position of the input waveguide relative to the on-axis position. Some parameters are left unchanged, so the results presented here may not be optimal for a particular geometry. However, this analysis may form the basis of future work on the optimization of such detector cavities, highlighting the interdependence of all the parameters defining the cavity structure. The analysis is presented in terms of the three cavities, and various modifications made to each cavity to investigate the subsequent effects of varying cavity dimensions.

This work is motivated by the detector cavities planned for the SAFARI instrument of the SPICA mission. SAFARI is an imaging grating spectrometer covering 30–210 μm , to allow for broadband photometry imaging and variable resolution imaging spectrometry.

6.2 Modelling of Detector Cavities within CST

CST (the background of which is described in chapter 5) was used to optimize models of detector cavities, using the frequency domain solver. The tantalum absorbing layers associated with TES bolometers within the cavities are modelled using ohmic sheets. The ohmic sheet is an infinitely thin surface with a surface impedance of $377 \Omega/\text{sq}$ to match free space impedance.

In order to investigate methods of increasing the absorbed power, the effect of having two ohmic sheets with and without a silicon dielectric between them was also considered. Offset input waveguide positions were also investigated. Offsetting the entrance waveguide could have the effect of breaking the symmetry and potentially increasing the optical efficiency.

Three cavities were considered. Cavity 1 has a square structure, with dimensions of 5 mm × 5 mm × 2.75 mm. The dimensions of cavity 2 are 5.08 mm × 2.54 mm × 6 mm. The waveguide is a standard WR-10, with dimensions of 2.54 mm × 1.27 mm, which is half the length and width dimensions of cavity 2. Cavity three has dimensions of 10.16 mm × 5.08 mm × 6 mm, which is twice the length and width dimensions of cavity 2.

The default absorber position is 0.75 mm from the back in all simulations, which is $\frac{\lambda}{4}$ at 100 GHz. However, this could additionally be modified for cavities 2 and 3, which would affect the simulation results, so the designs presented here may not be the optimal design. The absorbers fully fill the cavities as the height and width dimensions are kept the same for all cavities.

The cavities were modelled with walls of thickness 0.05 mm. All simulations were taken in the W band, that is 75–110 GHz.

6.3 Cavity 1

The initial model of cavity 1 is shown in figure 6.1a. This “build up” model is made by merging smaller shapes using Boolean addition in the CST CAD environment. This model is physically more realistic, but due to the complicated shape requires a significant amount of computing time in order to implement the mesh, especially at the corners. The second model, shown in figure 6.1b, has the cavity cut away from a block. This means the cavity is realized by cutting the shape from a larger block of metal in the CST CAD environment. The additional material has no effect

on the simulation results as all the radiation is directed into the cavity. However, it was found that building the mechanical structure differently resulted in different computational times.

The use of symmetry planes would be an additional way to reduce simulation time as only a quarter of the cavity would need to be analysed. This was not necessary in the case of these two small cavities, but would be useful when the cavity under investigation is larger. However, this method cannot be used when offset waveguide positions are being investigated. The simulation is single-moded, as a single-moded WR-10 waveguide is being used to excite the multi-moded cavity. As the entrance waveguide is single-moded, the fundamental mode (TE₁₁) is the only mode that can couple radiation into and out of the cavity, which makes the analysis straight forward.

6.3.1 Optimization of Simulation Efficiency

The initial simulation was made using Cavity 1, which has height 5 mm, width 5 mm, and depth 2.75 mm. The absorbing layer consists of an infinitely thin ohmic sheet, and is located 0.75 mm from the back of the cavity. Two models were used initially, the first where the full structure is built up in CST, and the second which consisted of starting with a block, and cutting out the cavity. Because the "build up" model is a more complicated shape, more mesh cells are required to model it, with a resulting increase in simulation time when compared with the "cut away" model. The two models, which are designed with equivalent internal cavity volume and materials, are shown in figure 6.1b.

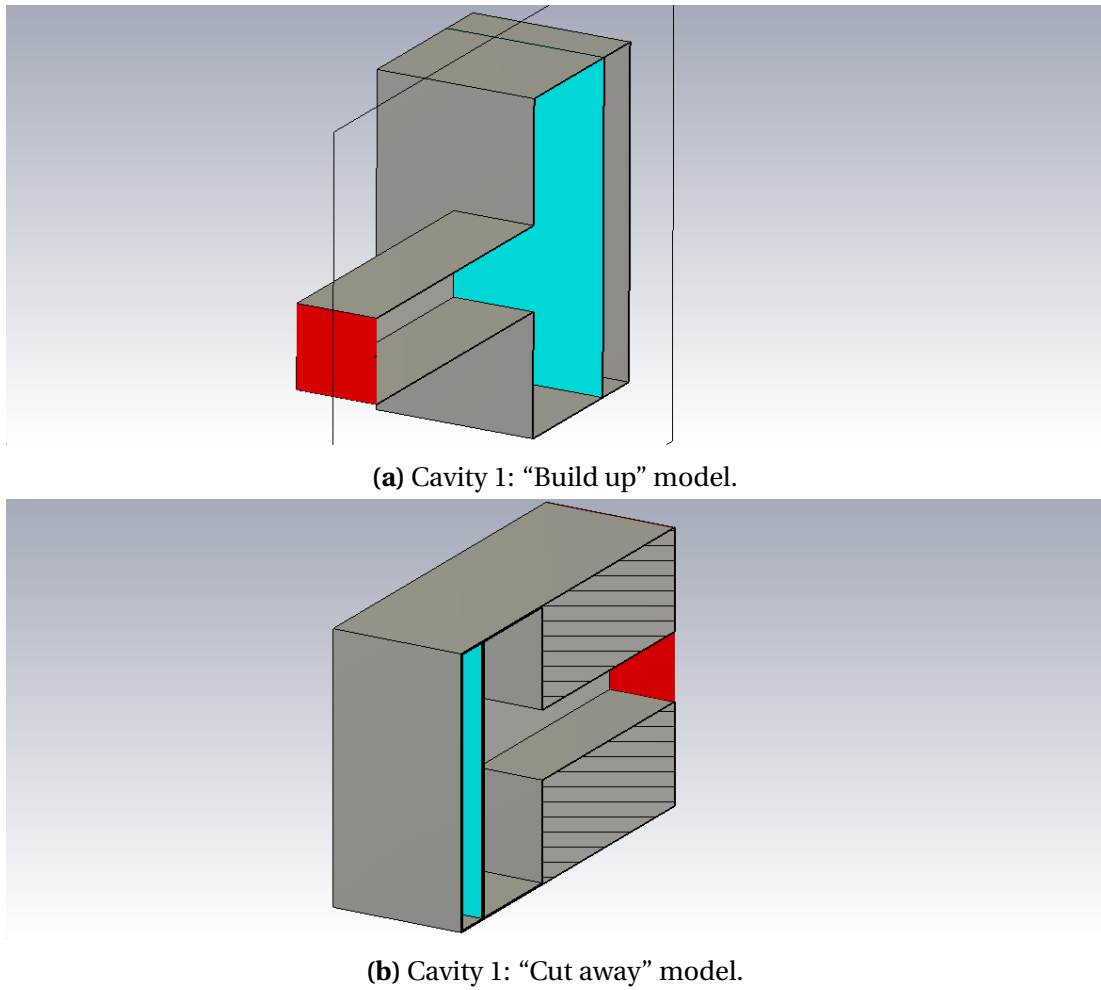


Figure 6.1: Two methods of modelling Cavity 1 within CST. Both give equivalent results.

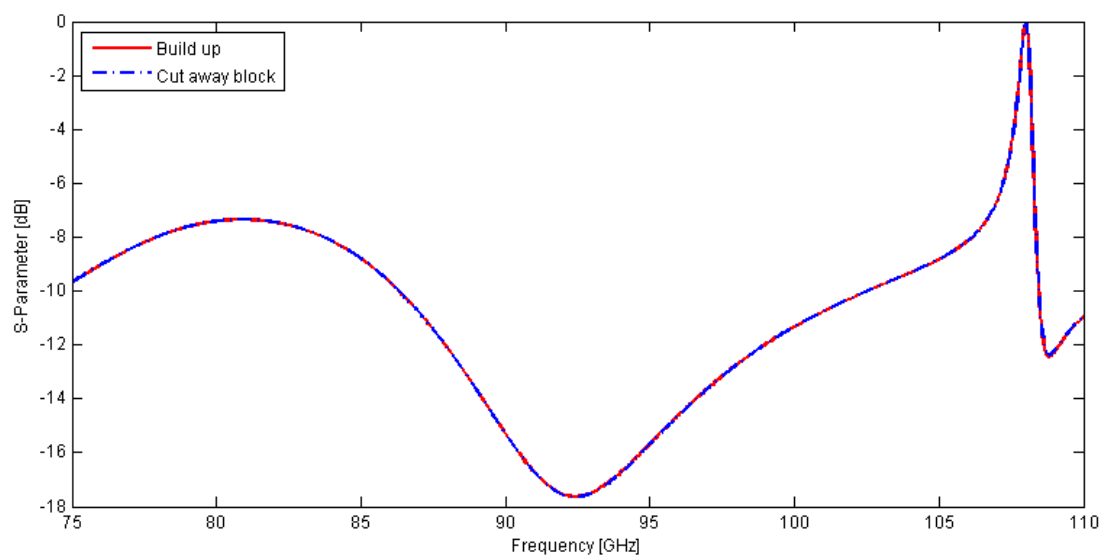


Figure 6.2: Comparison of S-Parameter results for the "build up" and "cut away" models of Cavity 1 in CST.

When the “build up” model and the “cut away” model are used in CST, the results are found to be equivalent as shown in figure 6.2. This is expected, as the additional material in the "cut away" model has no effect on the incoming beam. As a result, the more efficient "cut away" model was used for the remainder of the simulations.

The S parameter shown represents the power reflected out of the cavity. When the S parameter is 0 dB, this indicates that all the power is reflected back. Conversely, a low S parameter indicates good absorption. Figure 6.2, indicates very good absorption between 90 and 95 GHz, as an S parameter of -17 dB translates into over 98% of the incoming power absorbed, so the cavity is resonant at these frequencies. There is a peak around 107 GHz where none of the power is absorbed, probably due to modal cutoff frequencies, i.e. the TE_{23} mode.

6.3.2 Using Two Ohmic Sheets

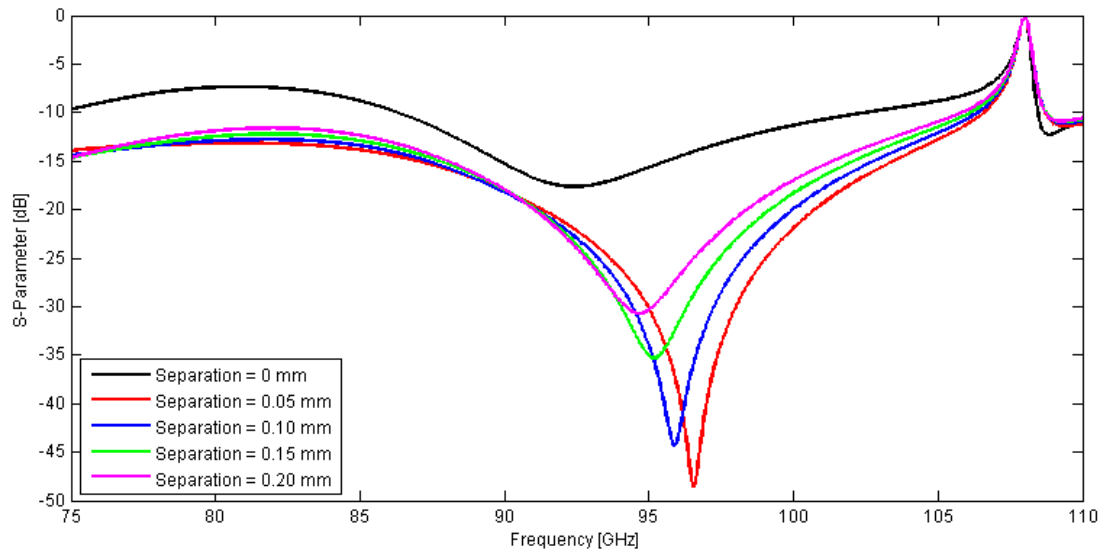


Figure 6.3: Cavity 1 with two ohmic sheets and an air gap.

Figure 6.3 shows the result when two ohmic sheets are introduced instead of a single one, with an air gap between them. Increased absorption is found for all results here, when compared to the case with one ohmic sheet, as can be seen in table 6.1. However, this increase is reduced slightly with an increasing separation between

the two sheets. The optimum absorption is to be found when their separation is 0.05 mm.

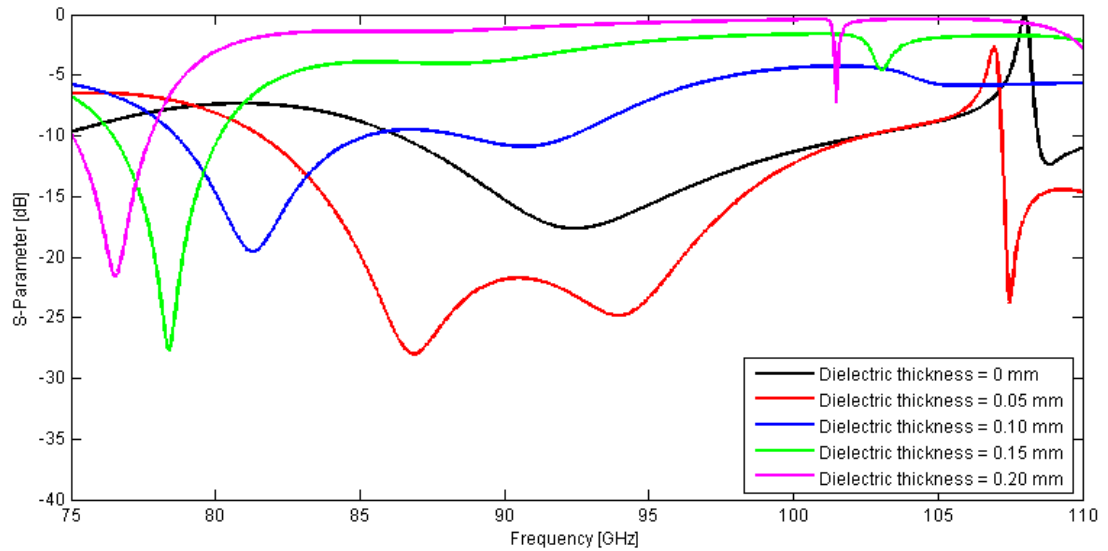
Separation (mm)	0	0.05	0.10	0.15	0.20
Average Absorbed Power (%)	88.9	95.2	95.0	94.6	94.1

Table 6.1: Average absorbed power for Cavity 1 with two ohmic sheets and an air gap by separation.

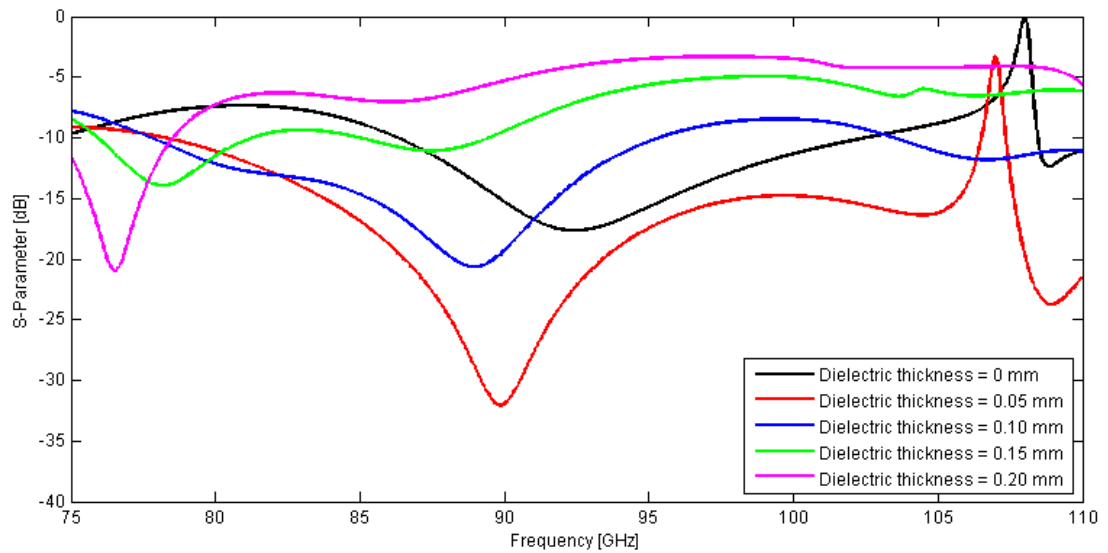
The addition of a second ohmic sheet provides greatly increased absorption – an S parameter of 5 dB less when an additional ohmic sheet is used indicates that about three times as much power is absorbed. For example, at 75 GHz, the S parameter is approximately -15 dB, meaning that almost 97% of the power is absorbed, which is an excellent result.

6.3.3 Modelling the Ohmic sheet on a Dielectric

The infinitely thin ohmic sheet model for the absorber used in the previous sections is unrealistic, as a real absorber is made using a thin absorbing layer on a dielectric substrate. In this section, a more realistic model is considered by including a dielectric (silicon, dielectric constant 11.67). This is modelled with one ohmic sheet in front of the dielectric, or with two ohmic sheets; one on either side of the dielectric layer.



(a) 1 Ohmic Sheet.



(b) 2 Ohmic Sheets.

Figure 6.4: Cavity 1 with Dielectric.

Figure 6.4 shows the results for a varying thickness of dielectric behind an ohmic sheet. Results are given for both the case with one ohmic sheet and with two. The black line (dielectric thickness = 0 mm) is equivalent to the result with one ohmic sheet and no dielectric.

Separation (mm)	0	0.05	0.10	0.15	0.20
Average Absorbed Power, 1 Ohmic Sheet (%)	88.9	92.5	81.1	54.6	29.4
Average Absorbed Power, 2 Ohmic Sheets (%)	88.9	95.9	92.4	82.0	69.7

Table 6.2: Average absorbed power for Cavity 1 by dielectric thickness.

The optimum absorption in both cases is for the 0.05 thickness of dielectric. Including an additional ohmic sheet also improves the absorption somewhat, as shown in table 6.2. The dielectric becomes significantly more reflective when it has a larger thickness; this is especially evident with one ohmic sheet. The thicker ohmic sheet results in a very poor cavity, as demonstrated by the low levels of absorption.

6.3.4 Offset Position of Waveguide

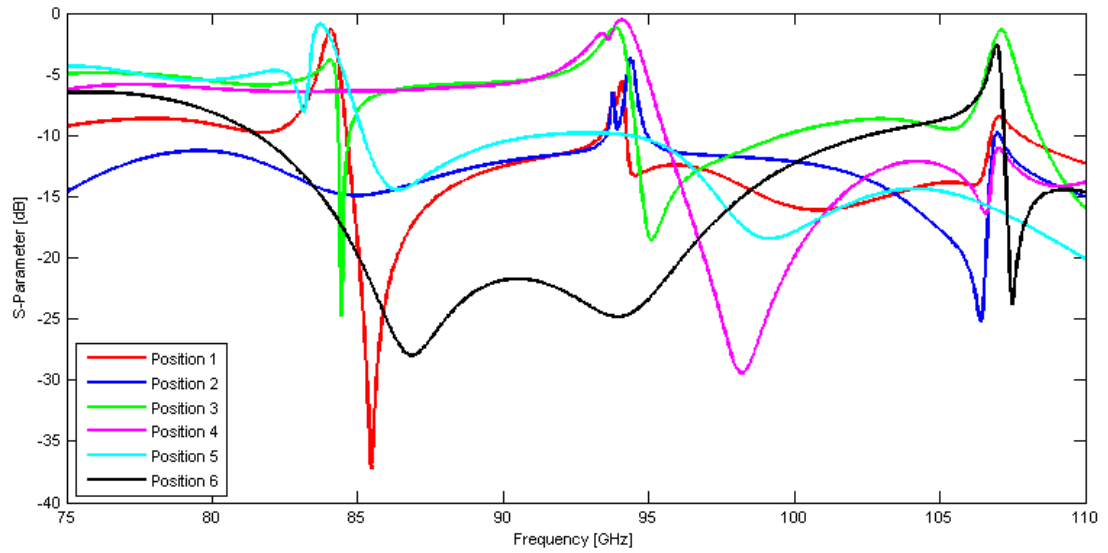
In this section, the optical performance of the cavity is investigated in relation to the input position of the waveguide.

Six offset positions were considered for the waveguide position for cavity 1. Due to symmetry, it was only necessary to consider offsets in one corner of the detector. Table 6.3 gives the x and y offsets with the position number used in the graphs. Note that position 6 is the symmetric case, and the same waveguide position as in the previous section. Following the results in the previous section, a silicon dielectric with a thickness of 0.05 mm was included for cases with one ohmic sheet and with two, for comparison.

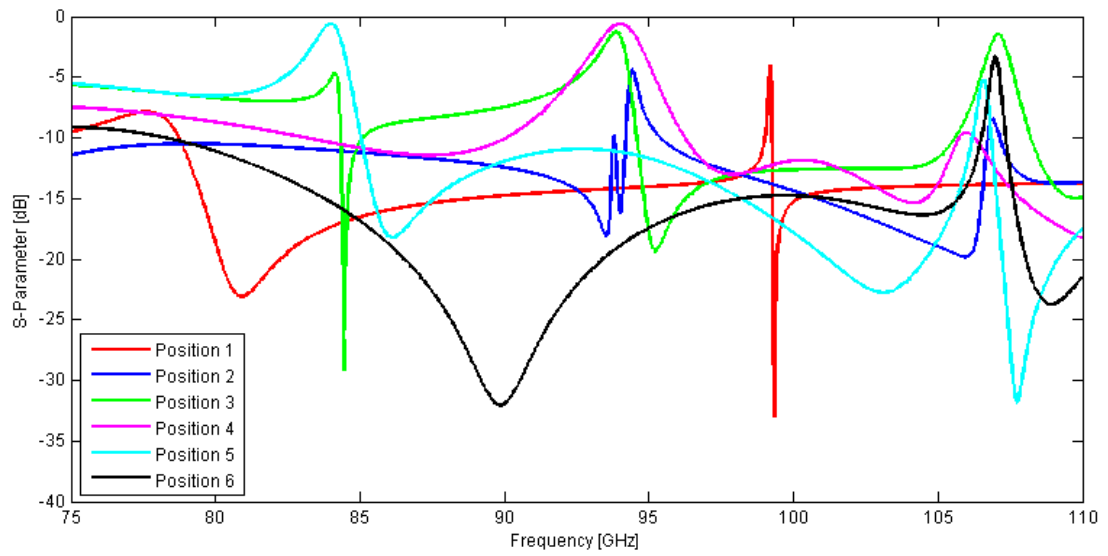
Position	X offset (mm)	Y offset (mm)
Position 1	-1.23	-1.865
Position 2	0	-1.865
Position 3	-1.23	-0.9325
Position 4	0	-0.9325
Position 5	-1.23	0
Position 6	0	0

Table 6.3: Offset positions considered for Cavity 1.

Figure 6.5 gives the results for the offset positions for the cases with one ohmic sheet and with two.



(a) 1 Ohmic Sheet.



(b) 2 Ohmic Sheets.

Figure 6.5: Cavity 1 with waveguide position offsets.

The average absorbed powers are given in table 6.4. In the first case, optimum absorption is found in position 2, although the symmetric case has an advantage if it is desired to have the cavity resonant between 85 and 95 GHz. In the second case, the symmetric case is found to have the most absorption, closely followed by position 1.

Position	1	2	3	4	5	6
Average Absorbed Power, 1 Ohmic Sheet (%)	91.7	94.1	77.6	81.3	86.1	92.4
Average Absorbed Power, 2 Ohmic Sheets (%)	95.4	93.8	83.0	86.6	88.0	95.9

Table 6.4: Average absorbed power for Cavity 1 by waveguide position.

In conclusion, shifting the input waveguide position by less than half a wavelength does not significantly increase the levels of absorbed power for the particular geometry of this cavity, which already has good absorption. It is not possible to generalize these results to different cavity dimensions, as the geometry of a cavity has a significant influence on its absorption, as shown in the analysis on other cavity designs.

6.3.5 Absorber position

A brief investigation was performed on the effect of absorber position on absorption. This was carried out on cavity 1 with 2 ohmic sheets, and the waveguide in the symmetric position, as this was the optimum case. The position of the absorber, including both ohmic sheets and the dielectric, was varied between 0.25 mm and 1.00 mm from the rear of the cavity; the results are graphed in figure 6.6.

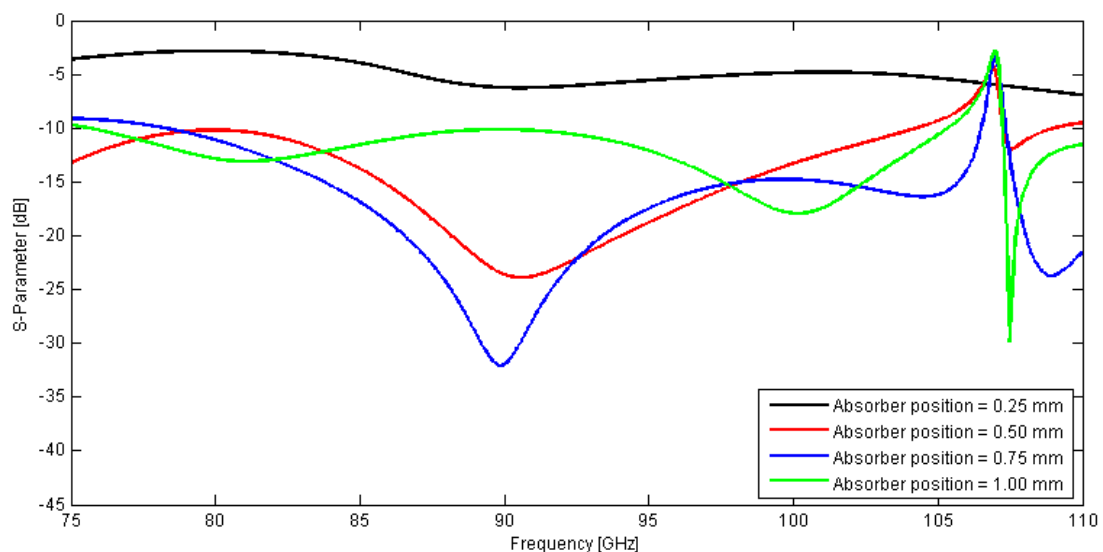


Figure 6.6: Cavity 2

Absorber position (mm)	0.25	0.50	0.75	1.00
Average Absorbed Power (%)	65.9	94.0	95.9	93.0

Table 6.5: Average absorbed power for Cavity 1 by waveguide position.

As shown in table 6.5, the absorber position is not critical, as long as it is not too close to the rear of the cavity, when compared with the wavelength. The absorption decreases significantly in the 0.25 mm case, and it is relatively consistent for the other three cases.

6.4 Cavity 2

Cavity 2 has dimensions of 5.08 mm \times 2.54 mm \times 6 mm, as shown in figure 6.7. While cavity 1 has a square-shaped cross-section, this cavity is rectangular, and the width and height dimensions are twice those of the WR-10 waveguide. The depth is somewhat longer, at 6 mm, and the absorber position is kept at 0.75 mm from the back of the waveguide.

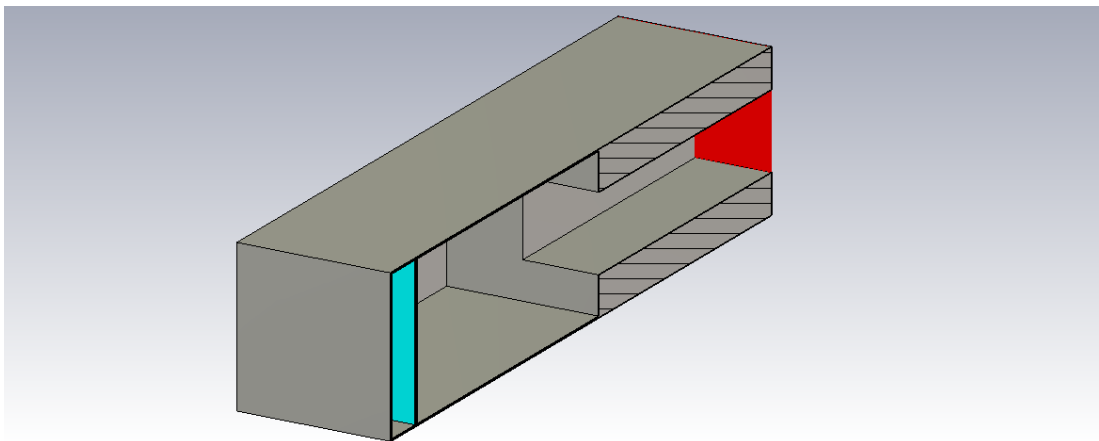


Figure 6.7: Cavity 2.

6.4.1 Two Ohmic Sheets

Figure 6.8 shows the result with two ohmic sheets and an air gap between them.

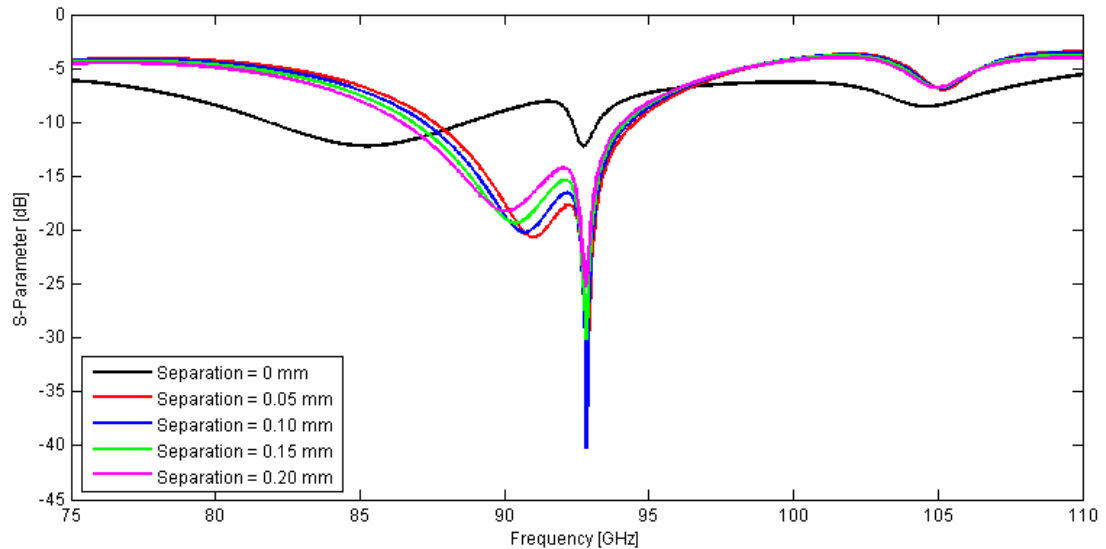


Figure 6.8: Cavity 2 with two ohmic sheets and an air gap.

As shown in table 6.6, there is no improvement over the case with one ohmic sheet, except for the small bandwidth between 87 and 95 GHz.

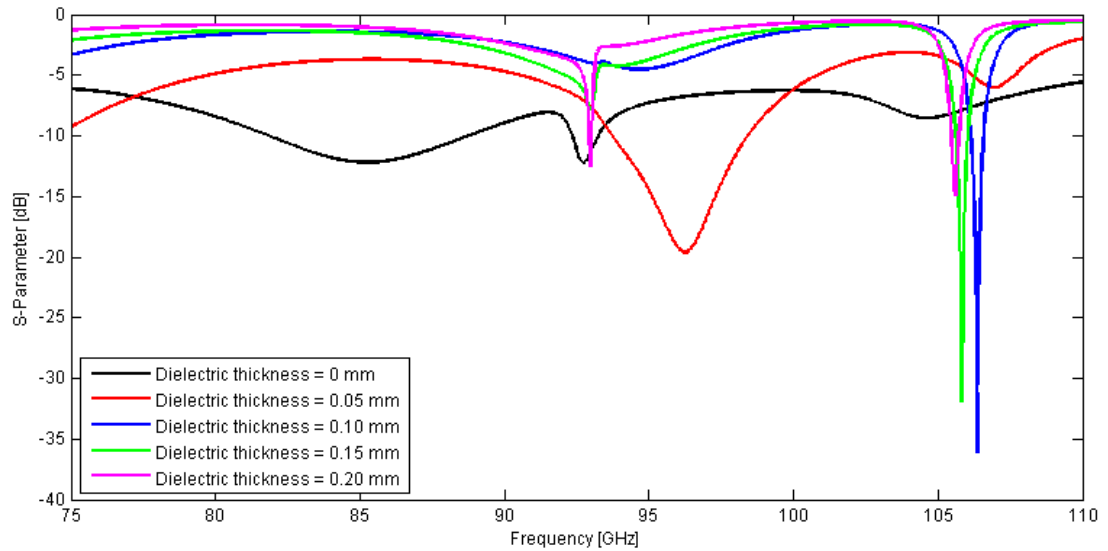
Separation (mm)	0	0.05	0.10	0.15	0.20
Average Absorbed Power (%)	83.8	73.8	74.3	75.2	76.1

Table 6.6: Average absorbed power for cavity 2 with two ohmic sheets and an air gap by separation.

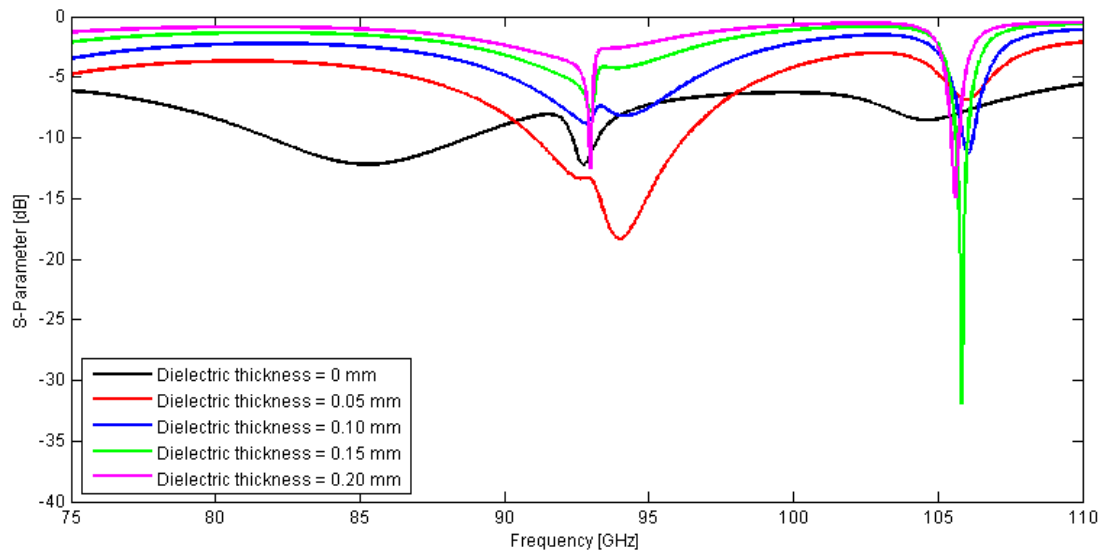
Of the cases with two ohmic sheets, the overall absorbed power increases with increasing wavelength. This particular cavity clearly performs worse than the previous example, as is evident from the lower levels of average absorbed power.

6.4.2 Effect of Dielectric Thickness

As with cavity 1, the effect of the inclusion of a dielectric in addition to the ohmic sheets was considered for cavity 2 in order to have a more realistic simulation.



(a) 1 Ohmic Sheet.



(b) 2 Ohmic Sheets.

Figure 6.9: Cavity 2 with Dielectric.

Figure 6.9 shows the results for a varying thickness of dielectric with both one and two ohmic sheets. As with cavity 1, the case with a 0.05 mm dielectric gave the best absorption, although this absorption is significantly less than the case with no dielectric, as shown in table 6.7. The addition of a second ohmic sheet has no advantage in this case.

Separation (mm)	0	0.05	0.10	0.15	0.20
Average Absorbed Power, 1 Ohmic Sheet (%)	83.8	70.0	37.5	36.8	27.4
Average Absorbed Power, 2 Ohmic Sheets (%)	83.8	68.4	52.1	36.8	27.4

Table 6.7: Average absorbed power for cavity 2 by dielectric thickness.

The geometry of cavity 2 is clearly not optimal, as the performance does not match that of cavity 1. This indicates that geometry is a significant factor which must be considered in the design of a detector cavity.

6.4.3 Offset Position of Waveguide

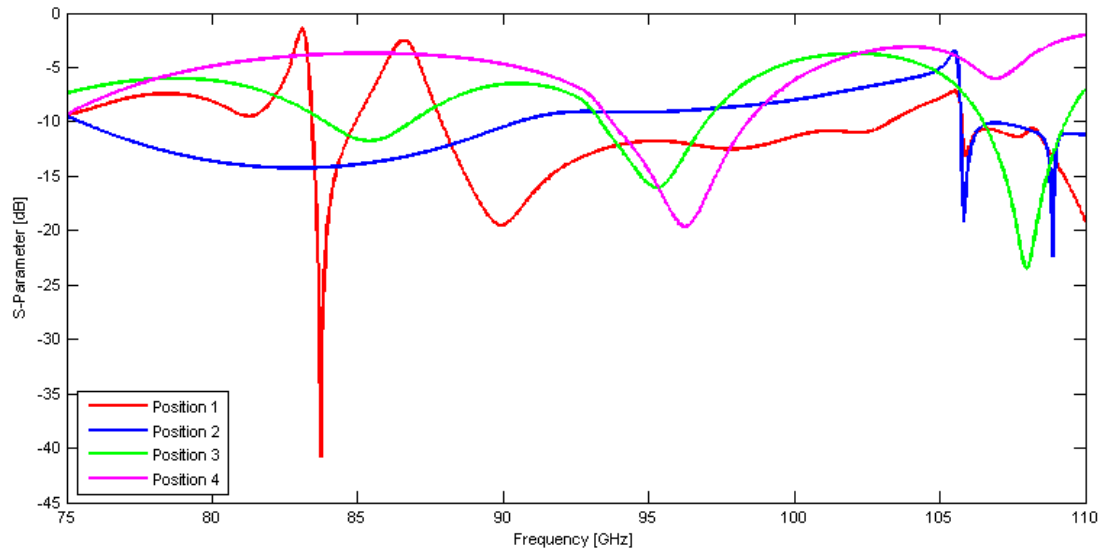
The effect of the offset location of the input waveguide is investigated below, to determine if it is possible to improve the performance of cavity 2.

Due to the smaller size of cavity 2 when compared with cavity 1, four offset positions were considered, taking advantage of symmetry so that only positions in one corner need to be considered. The positions were chosen so that there would be one in the corner, and two at the edges of the cavity. The x and y offsets are given in table 6.8 with the position numbers used in the graphs. The silicon once again had a thickness of 0.05 mm.

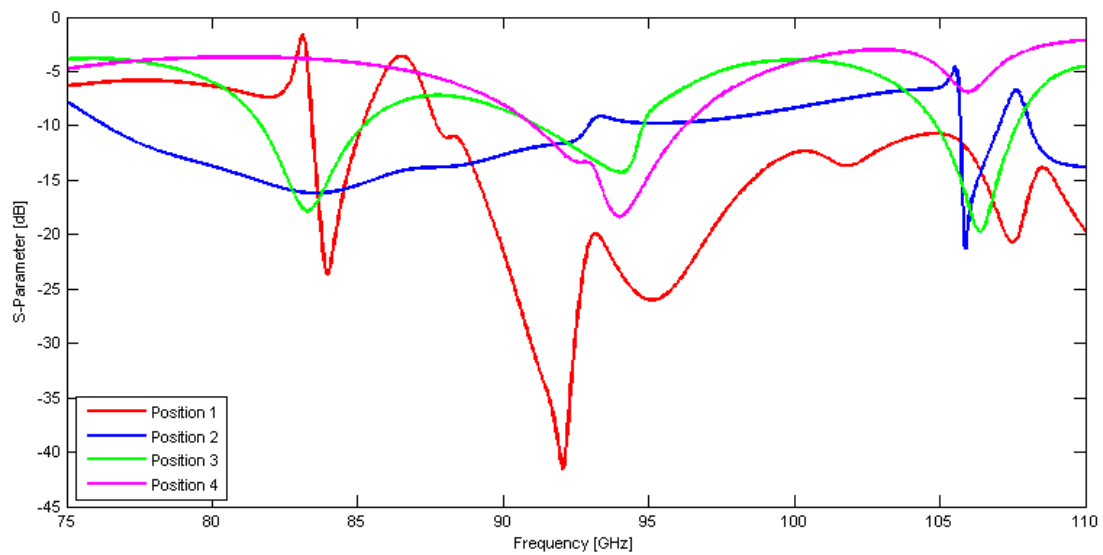
Position	X offset (mm)	Y offset (mm)
Position 1	-1.27	-0.635
Position 2	0	-0.635
Position 3	-1.27	0
Position 4	0	0

Table 6.8: Offset positions considered for cavity 2.

Figure 6.10 gives the S parameter graphs for these offsets in both cases.



(a) 1 Ohmic Sheet.



(b) 2 Ohmic Sheets.

Figure 6.10: Cavity 2 with waveguide position offsets.

Unlike the situation with cavity 1, the average absorbed power increases when the waveguide is offset, as shown in table 6.9. The absorption increases significantly especially for position 1 (corner) and position 2 (top or bottom).

This result is in stark contrast to that of cavity 1, where the offset had effectively no effect.

Position	1	2	3	4
Average Absorbed Power, 1 Ohmic Sheet (%)	88.6	89.3	81.2	70.0
Average Absorbed Power, 2 Ohmic Sheets (%)	89.8	90.8	79.6	68.4

Table 6.9: Average absorbed power for cavity 2 by waveguide position.

6.5 Cavity 3

Cavity 3 has the same ratio of height to width as cavity 2, but these dimensions are doubled. The depth remains the same, so the overall dimensions are 10.16 mm × 5.08 mm × 6 mm. The absorber still fills the cavity. This increase in cavity size provides conditions for many more modes to propagate. The fact that more modes are supported means that absorption can be different.

6.5.1 Two Ohmic Sheets

As with the previous cavities, the effect of the inclusion of a second ohmic sheet was considered for cavity 3. This is shown in figure 6.11.

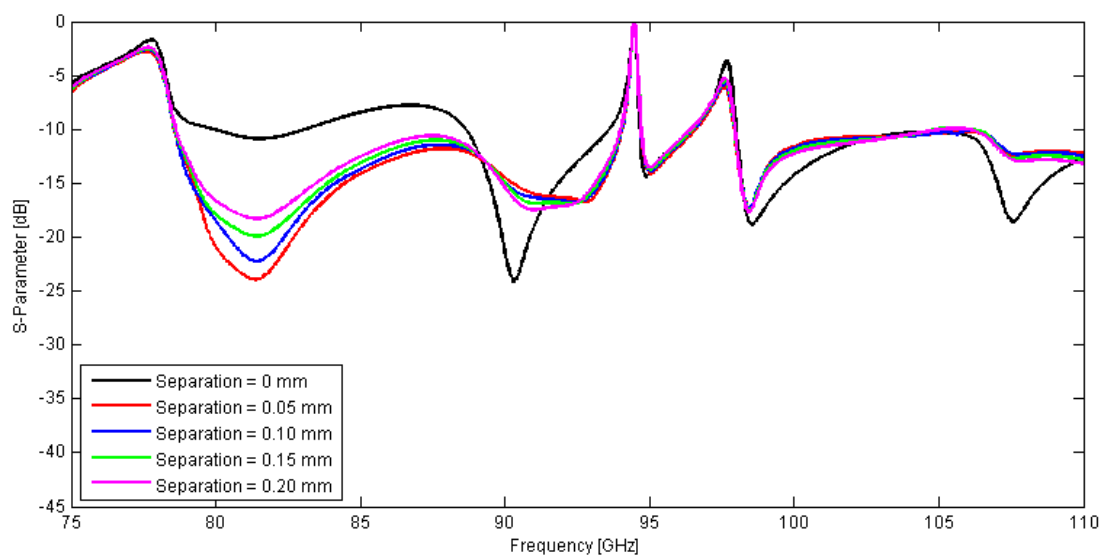


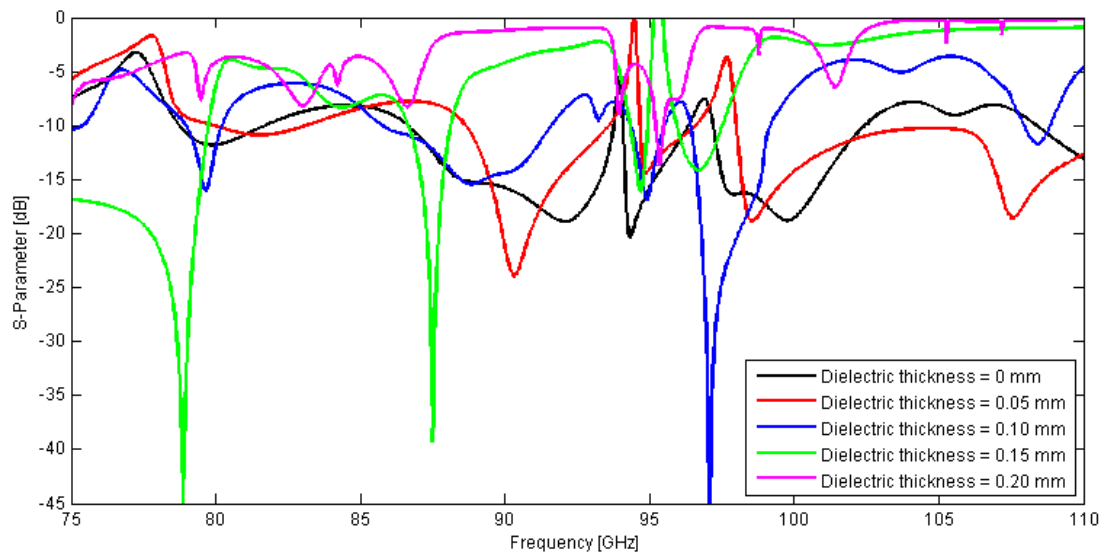
Figure 6.11: Cavity 3 with two ohmic sheets and an air gap.

The average absorbed power is outlined in table 6.10. Unlike in cavity 2, the absorption increases when there are two ohmic sheets separated by an air gap, which was the case for cavity 1.

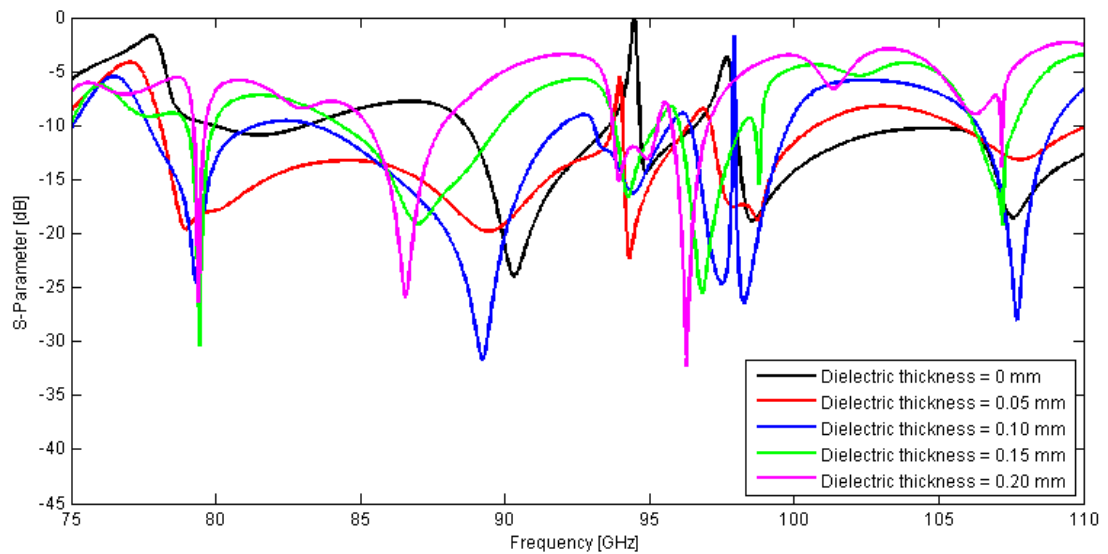
Separation (mm)	0	0.05	0.10	0.15	0.20
Average Absorbed Power (%)	87.5	90.6	90.4	90.1	89.9

Table 6.10: Average absorbed power for cavity 3 with two ohmic sheets and an air gap by separation.

6.5.2 Effect of Dielectric Thickness



(a) 1 Ohmic Sheet.



(b) 2 Ohmic Sheets.

Figure 6.12: Cavity 3 with Dielectric.

Figure 6.12 shows the S parameter results for a varying thickness of dielectric with both one and two ohmic sheets.

Table 6.11 makes it clear that increasing the dielectric thickness reduces the absorption in both cases. This is similar to the result found for cavity 2, although for cavity 3 this is much less pronounced. A similar effect was observed for cavity 1. Cavity 3 is twice as large as cavity 2, and so supports many more modes due to its larger axial extent. This leads to great modal scattering and many more modes propagating. Higher order modes excited in cavity 3 do not exist in cavity 1 and 2 so direct comparisons is difficult. It should also be noted that higher order modes have different impedances and the absorber position of 0.75mm from the backshort will not be optimal for these modes.

Separation (mm)	0	0.05	0.10	0.15	0.20
Average Absorbed Power, 1 Ohmic Sheet (%)	89.9	87.5	82.7	61.9	42.3
Average Absorbed Power, 2 Ohmic Sheets (%)	87.5	92.4	90.3	83.3	74.6

Table 6.11: Average absorbed power for cavity 3 by dielectric thickness.

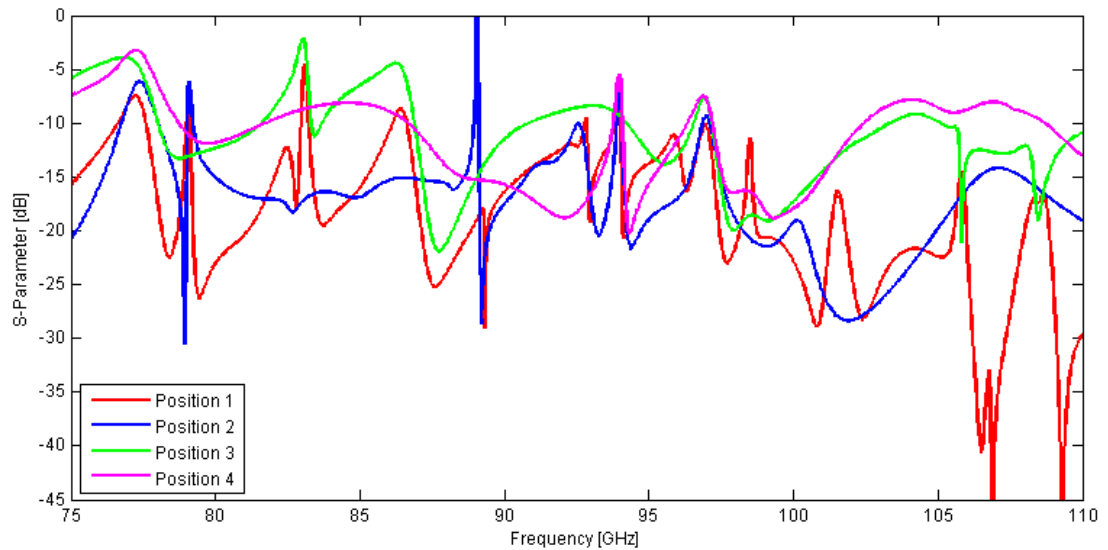
6.5.3 Offset Position of Waveguide

Four offset positions were considered for cavity 3. The x and y offsets are given in table 6.12 with the position numbers used in the graphs and table. The silicon crystalline dielectric once again had a thickness of 0.05 mm. The offset positions were chosen with similar conditions to cavity 2: one position at the corner, and two at the sides in addition to the central position.

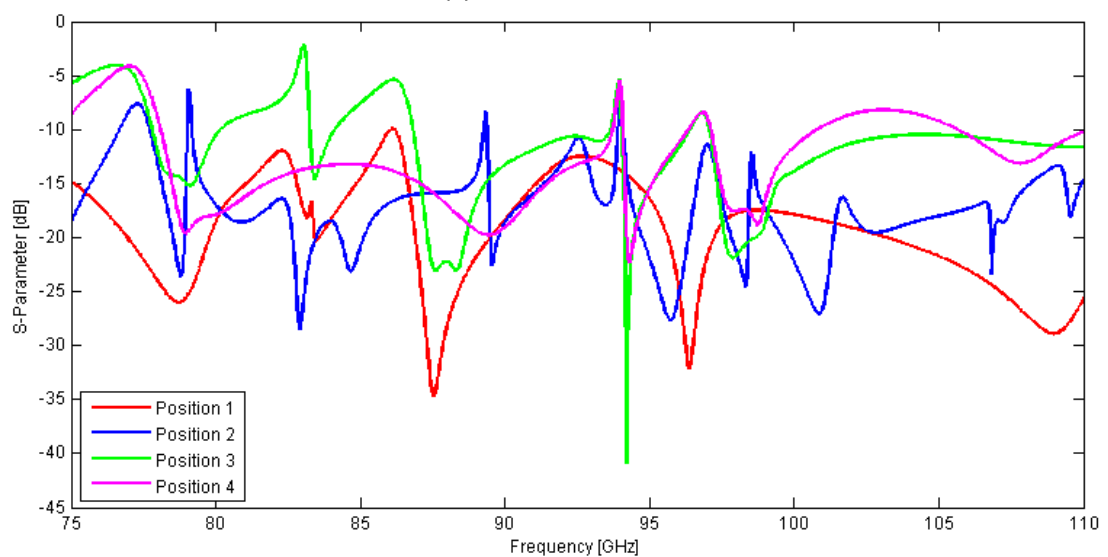
Position	X offset (mm)	Y offset (mm)
Position 1	-3.81	-1.905
Position 2	0	-1.905
Position 3	-3.81	0
Position 4	0	0

Table 6.12: Offset positions considered for cavity 3.

Figure 6.13 shows the S parameter results for these cases.



(a) 1 Ohmic Sheet.



(b) 2 Ohmic Sheets.

Figure 6.13: Cavity 3 with waveguide position offsets.

As shown in table 6.13, the average absorbed power is significantly increased for the offset cases, especially at the corner, with the best result for the case with two ohmic sheets. This result follows the same pattern as cavity 2, although the larger cavity has a higher absorption (98%) than that of the smaller one with the same dimensional ratio (87.5%).

Position	1	2	3	4
Average Absorbed Power, 1 Ohmic Sheet (%)	97.0	96.6	88.8	89.8
Average Absorbed Power, 2 Ohmic Sheets (%)	98.1	97.2	89.7	92.3

Table 6.13: Average absorbed power for cavity 3 by waveguide position.

6.6 Conclusion

The conclusion from this analysis of three different cavity geometries is that the absorption of a detector cavity is highly dependent on the dimensions of the cavity itself. In all cases, the addition of a thin dielectric of thickness 0.05 mm improved the absorption somewhat. The symmetric case for the waveguide position gave the best result for cavity 1, but the best result for cavity 2 was found to be when the waveguide was positioned in the corner. This suggests that close attention should be made to the design of cavities for missions such as the SAFARI instrument for SPICA. Depending on the space available for each detector, a specific cavity geometry should be designed to best match a particular bandwidth of operation. The position of the absorbing layer and the relative dimensions of the cavity itself could lead to drastically different optical performance. As this brief analysis suggests, each cavity dimension is dependent on other dimensions to achieve a certain level of performance. As such, a specific optical arrangement is required for a particular detector.

Chapter 7

Conclusions

This thesis has been primarily concerned with the quasi-optical analysis of millimetre and submillimetre devices and receivers, including the design, analysis and verification of the 4 mm receiver channel for the 20 m telescope at Onsala Space Observatory.

Chapter 1 gives a general overview to the historical background of far-infrared astronomy, and the development of millimetre and submillimetre astronomy in particular. The astronomical applications of this part of the electromagnetic spectrum are outlined, as are the unique challenges associated with astronomy at these wavelengths. These applications form the primary motivation behind the work in this thesis. In addition, commercial applications of Terahertz radiation are outlined.

Chapter 2 is a review of the background theory and analysis techniques which form the basis of the work in this thesis. A comprehensive review of the theoretical foundations of Gaussian beam mode analysis is presented, including the application to quasi-optical systems using ray transfer matrix analysis. The type of antenna system used in this thesis is introduced, along with some background on conical corrugated horn antennae, and beam coupling methods. GRASP, which is the software package used for the analysis presented in chapter 4, is introduced, with a general description of the principles of physical optics, on which its operation is based. The operation of GRASP is outlined, and a comparison of its computational simulations

with experimental measurements made of a pyramidal horn antenna with the vector network analyser is reported on.

Chapter 3 introduces the Onsala Space Observatory, the 25 m and 20 m telescopes, and outlines the 20 m telescope optics, as this is relevant for the design of the 4 mm receiver. The 4 mm receiver is introduced, outlining the design requirements, and the design of the horn. The design of the 4 mm receiver was realized using Gaussian beam mode analysis and ABCD matrix analysis. Also reported in this chapter is the initial optical analysis, which presents the evolution of the beam throughout the system, with parameters given at planes of interest. These were calculated using the ABCD code, and by representing the horn input using a truncated Bessel function. Following this, a truncation analysis is presented, which demonstrates that the power lost in the beam due to truncation at the mirrors and windows is at an acceptable level. Finally, optical efficiency calculations are presented, which show that the design results in good coupling with a point source on the sky. These calculations were all carried out using the ABCD matrix technique.

This analysis is supplemented in chapter 4 by using the commercial software package GRASP, which allows for more accurate physical optics analysis. The analysis is presented using three input feed models. The first two of these are built-in feed options in GRASP; the Gaussian beam feed allows for a basic approximation of the input horn field, and the GRASP hybrid-mode conical horn gives a more accurate approximation, although it does not account for cross-polar levels. The third input method allows for external user-defined grid files. These files were generated using the in-house mode matching software *Scatter*, which allows for full vector free space analysis, including co and cross polar fields. Results are given and compared for these three methods, both at the focal planes, and at the secondary mirror, where the beam is required to be wavelength-independent. The farfield patterns projected onto the sky are then presented, which were calculated by modelling the full telescope in GRASP, in addition to the 4 mm system. These patterns show that the main beam on the sky is symmetric, which validates the proposed design. Beam effi-

ciencies and cross-polar levels are then reported, which show good performance, as necessitated by the design requirements. The design is compared with the existing 3 mm system, demonstrating similar aberrations at the secondary mirror, which already operates well. When presenting the 4mm receiver optical performance an on-axis aberration was noticed for the beam at the secondary mirror. By projecting this beam onto the sky and showing that this aberration is spread to far out sidelobes it is shown that this effect would not affect the performance of the receiver. The same effect also exists in the operating 3mm system and was not previously noticed. This helps validate the 4mm design implemented. Finally, the simulation is compared with experimental results, which were carried out at Onsala Space Observatory.

Chapter 5 concerns the design of a lens antenna with good beam characteristic in the W band as an potential alternative to horn antennae, but operating over a narrower bandwidth. The background theory of planar antennae is outlined, and the cavity method of analysis is presented for rectangular and circular patch antennae. The S parameter and directivity are defined, as these are important parameters for determining the resonance and beam characteristics of the antennae. An introduction to the operation of CST Microwave Studio, a commercial software package is given, as this software forms the basis of the simulations presented in chapters 5 and 6. Several patch designs are considered, varying parameters such as the dimensions of the patch, the thickness of the dielectric, and feed wire dimensions. The addition of a dielectric lens or "lenslet" is considered, and this is required to considerably increase the performance of the antenna with the desired higher directionality. Further work includes the experimental manufacture and testing of the lens antenna design.

Chapter 6 examines the behaviour of detector waveguide cavities. Three cavity designs are examined within CST, and the effect of varying the dielectric thickness under the thin tantulum absorbing layer (modelled as an infinitely thin ohmic sheet) and the input waveguide position is outlined. Cavity 1 was found to have no significant increase in absorption when the waveguide position was offset, however the

opposite was found in the cases of cavities 2 and 3. This shows that the absorption efficiency (how much power could be ideally absorbed in this configuration) of a detector cavity is highly dependent on its dimensions, and many parameters must be accounted for when seeking an optimal design. Further work could include using this information in the design of a cavity with optimized absorption properties.

Bibliography

- [1] A. Unsold and B. Baschek, *The New Cosmos: An Introduction to Astronomy and Astrophysics*. New York: Springer-Verlag, 2005.
- [2] P. Ronan, “Em spectrumrevised.png.” Wikimedia Commons, 2013. Licensed under the Creative Commons Attribution-Share Alike 3.0 Unported license.
- [3] J. C. Maxwell, “A dynamical theory of the electromagnetic field,” *Philosophical Transactions of the Royal Society*, vol. 155, pp. 459–512, January 1865.
- [4] B. F. Burke and F. G. Smith, *An Introduction to Radio Astronomy*. Cambridge: Cambridge University Press, 1996.
- [5] Very Large Array. <http://www.vla.nrao.edu/>.
- [6] ALMA. <http://www.almaobservatory.org/>.
- [7] ESA Science and Technology, “*Herschel*.” <http://sci.esa.int/herschel/>.
- [8] NASA, “*Hubble Space Telescope*.” https://www.nasa.gov/mission_pages/hubble/main/index.html.
- [9] ESA Science and Technology, “*XMM-Newton*.” <http://sci.esa.int/xmm-newton/>.
- [10] C. O’Sullivan and J. A. Murphy, *Field Guide to Terahertz Sources, Detectors and Optics*. Bellingham: SPIE, 2012.

- [11] J. M. Byrd et al, "The electromagnetic spectrum." http://www.als.lbl.gov/als/science/sci_archive/135terahertz.html, 2006. Public Domain under the terms of Title 17, Chapter 1, Section 105 of the US Code.
- [12] P. F. Goldsmith, *Quasioptical Systems: Gaussian Beam Quasioptical Propagation and Applications*. New York: IEEE Press, 1998.
- [13] NASA, "Atmospheric electromagnetic opacity." NASA copyright policy states that NASA material is not protected by copyright unless noted.
- [14] Teraview, "*Terahertz Light Applications*." <http://www.teraview.com/applications/index.html>.
- [15] J. E. Federici et al, "Thz imaging and sensing for security applications—explosives, weapons and drugs," *Semiconductor Science and Technology*, vol. 20, no. 7, p. S266, 2005.
- [16] J. Y. Suen and W. J. Padilla, "Superiority of terahertz over infrared transmission through bandages and burn wound ointments," *Appl. Phys. Lett.*, vol. 108, no. 233701, 2016.
- [17] Y.-C. Shen, "Terahertz pulsed spectroscopy and imaging for pharmaceutical applications: A review," *International Journal of Pharmaceutics*, vol. 417, pp. 48–60, 2011.
- [18] Wolfram, "*Wolfram Mathematica: Modern Technical Computing*." <https://www.wolfram.com/mathematica/>.
- [19] A. E. Siegman, *Lasers*. Mill Valley, CA: University Science Books, 1986.
- [20] M. Candotti, *Design, Analysis and Optimisation of Quasi-Optical Systems for Sub-mm Astronomy Instrumentation*. PhD thesis, National University of Ireland, Maynooth, 2007.

- [21] K. F. Riley, M. P. Hobson, and S. J. Bence, *Mathematical Methods for Physics and Engineering*. Cambridge: Cambridge University Press, 2006.
- [22] H. Kogelnik, “Imaging of optical modes—resonators with internal lenses,” *Bell Syst. Tech. J.*, vol. 44, pp. 455–494, 1965.
- [23] M. Whale, *Optical Characterisation of Astronomical Submillimetre Receivers including ALMA Bands 5 and 9*. PhD thesis, National University of Ireland, Maynooth, 2010.
- [24] R. J. Potton, “Reciprocity in optics,” *European Journal of Physics*, vol. 67, pp. 717–754, 2004.
- [25] M. Born and E. Wolf, *Principles of Optics: Electromagnetic Theory of Propagation Interference and Diffraction of Light*. Chapman & Hall, 1997.
- [26] R. J. Wylde, “Millimetre-wave gaussian beam-mode optics and corrugated feed horns,” *Microwaves, Optics and Antennas, IEEE Proceedings H*, vol. 131, pp. 258–262, August 1984.
- [27] F. Cahill, *Design and Analysis of Corrugated Conical Horn Antennas with Terahertz Applications*. MSc thesis, National University of Ireland, Maynooth, 2015.
- [28] A. W. Rudge, K. Milne, A. D. Olver, and P. Knight, *The Handbook of antenna design*. London: P. Peregrinus on behalf of the Institution of Electrical Engineers, 1986.
- [29] L. Diaz and T. A. Milligan, *Antenna engineering using physical optics*. Boston: Artech House, 1996.
- [30] A. Ludwig, “The definition of cross polarization,” *IEEE Transactions on Antennas and Propagation*, vol. 21, pp. 116–119, Jan 1973.
- [31] TICRA, *GRASP9 Reference Manual*, 2010.

- [32] S. Doherty, *Optical and Quasi-Optical Design and Analysis of Astronomical Instrumentation including a Prototype Safari Pixel*. PhD thesis, National University of Ireland, Maynooth, 2012.
- [33] M. L. Gradziel et al, “Improving the efficiency of quasi-optical analysis and design of terahertz systems,” in *15th International Symposium on Space Terahertz Technology*, pp. 255–262, 2004.
- [34] M. Whale, “*OSO 4mm Receiver - Notes on Optical Design & Prescribed Work Packages.*” Internal report, 2014.
- [35] V. B. et al., “A new 3 mm band receiver for the Onsala 20m antenna,” *Astronomy and Astrophysics*, vol. 580, no. A29, 2015.
- [36] Onsala Space Observatory, “*About us.*” <http://www.chalmers.se/en/centres/oso/about-us/Pages/default.aspx>.
- [37] Swedish Research Council, “*International Collaboration.*” <http://www.vr.se/inenglish/international.html>.
- [38] LOFAR, “*European Stations.*” <http://www.lofar.org/about-lofar/general-information/european-stations/european-stations>.
- [39] Nordic ARC node, “*Home.*” <http://www.nordic-alma.se/>.
- [40] Onsala Space Observatory, “*Technical description (25 m telescope).*” <http://www.chalmers.se/en/centres/oso/radio-astronomy/25m/Pages/Technical-description.aspx>.
- [41] Peterkz, “Onsala-20m-antenn.jpg.” Wikimedia Commons, 2015. Licensed under the Creative Commons Attribution 4.0 International licence.
- [42] Onsala Space Observatory, “*Technical description (20 m telescope).*” <http://www.chalmers.se/en/centres/oso/radio-astronomy/20m/Pages/Description.aspx>.

- [43] O. Nyström, *Design, Characterization, and Calibration of Low-Noise Terahertz Receivers*. PhD thesis, Chalmers University of Technology, 2011.
- [44] Committee on Radio Astronomy Frequencies, “*Radio frequencies of the astrophysically most important spectral lines.*” <http://www.craf.eu/iaulist.htm>, 2003.
- [45] J. A. Murphy, A. Egan, and S. Withington, “Truncation in millimeter and submillimeter-wave optical systems,” *IEEE Trans. on Antennas & Propagation*, vol. 41, pp. 1408–1413, 1993.
- [46] N. Trappe, *Quasi-optical Analysis of the HIFI Instrument for the Herschel Space Telescope*. PhD thesis, National University of Ireland, Maynooth, 2002.
- [47] J. Flygare, “*OSO 4mm Test Setup and Notes.*” Internal report, 2015.
- [48] E. W. Weisstein, “*Convolution Theorem.*” <http://mathworld.wolfram.com/ConvolutionTheorem.html>. From MathWorld—A Wolfram Web Resource.
- [49] S. Drabowitch, A. Papiernik, H. Griffiths, and J. Encinas, *Modern Antennas*. London: Chapman & Hall, 1998.
- [50] Computer Simulation Technology, *CST Microwave Studio, Workflow & Solver Overview*, 2013.
- [51] CST, “*Antenna Design and Simulation.*” <https://www.cst.com/antenna>.
- [52] H. D. Young and R. A. Freedman, *University Physics*. Bertrams, 2008.
- [53] Chhe, “*Tirdiagram2.jpg.*” Wikimedia Commons, 2009. Public domain.
- [54] A. Neto, D. Pasqualini, and A. Toccafondi, “Mutual coupling between slots printed at the back of elliptical dielectric lenses,” *IEEE Transactions on Antennas and Propagation*, vol. 47, no. 10, pp. 1504–1507, 1999.